ISSN 1913-1844 (Print)
ISSN 1913-1852 (Online)

MODERN APPLIED SCIENCE

Vol. 3, No. 7
July 2009

Canadian Center of Science and Education

Editorial Board

Modern Applied Science

www.ccsenet.org/journal.html

Vol. 3, No. 7

July 2009

Contents

Modern Applied Science

www.ccsenet.org/journal.html

Vol. 3, No. 7

July 2009

Contents

Modern Applied Science

www.ccsenet.org/journal.html

Vol. 3, No. 7

July 2009

Effects of Temperature and Binder Type on the Dynamic Creep of Asphaltic Concrete Incorporating Geometrically Cubical Aggregates Subjected to Ageing

Meor Othman Hamzah

School of Civil Engineering, Universiti Sains Malaysia

Engineering Campus, 14300 Nibong Tebal, Pulau Pinang, MALAYSIA

Tel: 60-04-599-6210 Fax: 60-04-594-1009

Ramadhansyah Putra Jaya

School of Civil Engineering, Universiti Sains Malaysia

Engineering Campus, 14300 Nibong Tebal, Pulau Pinang, MALAYSIA

Joewono Prasetijo

School of Civil Engineering, Universiti Sains Malaysia

Engineering Campus, 14300 Nibong Tebal, P. Pinang, MALAYSIA

Tel: 60-04-599-6290 Fax: 60-04-594-1009

E-mail: Joewono.Prasetijo@ruhr-uni-bochum.de, cejoewono@eng.usm.my

Khairun Azizi M.A.

School of Materials & Mineral Resources, Universiti Sains Malaysia

Engineering Campus, 14300 Nibong Tebal, Pulau Pinang, MALAYSIA

Abstract

This paper presents an evaluation of the effects of temperature and binder type on the dynamic creep properties of asphaltic concrete mixtures incorporating granite aggregates produced via compression and impact modes of crushing. The creep test was carried out using the Asphalt Universal Testing Machine in accordance with procedures outlined in ASTM D4123. A conventional 80/100 bitumen and Styrene-Butadiene-Styrene (SBS) modified bitumen were used in sample preparation to evaluate the effects of binder types while the dynamic creep test was carried out at 40^{o}C and 60^{o}C. The results show that mixes prepared using geometrically cubical aggregate shape and SBS modified mixes exhibit higher creep stiffness than the unmodified mixtures. Temperature has a significant effect on creep stiffness, a mere 20^{o}C increase from 40^{o}C can cause the stiffness of unaged mixes to increase by as much as 51.8%. Linear regression analysis showed that mixes incorporating geometrically cubical aggregates and modified mixes are the least susceptible to creep stiffness.

Keywords: Creep stiffness, Short-Term ageing, Long-Term ageing, Modified binder, Geometrically cubical

1. Introduction

Permanent deformation in paving materials develops gradually with increasing number of load applications, and it appears as longitudinal depression in the wheel paths accompanied by small upheavals at the sides. The creep test provides sufficient information to determine the instantaneous elastic (recoverable) and plastic (irrecoverable)

components and the time independent and time dependent of the materials response. Zhao (2002) defined the cumulative permanent strain curve into three zones: primary, secondary, and tertiary as shown in Figure 1. In the primary zone, the permanent deformation or strain accumulates rapidly. The incremental permanent deformation tends to decrease, reaching a constant value in the secondary zone. Finally, the incremental permanent deformation again increases and accumulates rapidly in the tertiary zone. In the field, Parker and Brown (1992) suggested that the top 7 to 10 cm of the pavement system is the portion which is most vulnerable to rutting. The rut rate depended on factors such as axle load, number of axle repetitions, tyre inflation pressure and pavement temperature. Kamal et. al. (2005) carried out creep tests on the cores extracted from the field. Mixes prepared using polymer modified bitumen were found to exhibit less accumulated strain at higher temperatures when compared to the conventional mixes.

The effects of coarse aggregate morphologies such as shape, angularity, and texture on the rutting resistance of hot mix asphalt (HMA) have been analyzed from field observations and laboratory standard tests. Significant increases in stability have been reported by Wedding and Gaynor (1961) when crushed gravel was used in place of uncrushed natural gravel in an HMA mixture. About 45 percent increase in stability has been reported with the substitution of all crushed aggregate (crushed gravel coarse and fine aggregate) for natural sand and gravel. Campen and Smith (1948) reported an increase in HMA stability of 30% to 190% by using crushed aggregate as compared to HMA incorporating natural rounded aggregate.

In service, HMA mixes undergo an ageing process resulting in bitumen embitterment. Typically, the effects of ageing on the mixture performance were investigated by ageing the bitumen and subsequently measuring the change in physical properties. In many instances, the process was extended into ageing of the mixes. Bell et al. (1994) found that the ageing rates for all bitumen tested have diminished significantly with temperature reduction suggesting that below 55^{o}C to 60^{o}C oxidative ageing may be relatively insignificant. Daniel at el. (2002) used two methods of simulating the hot-mix process. The first step involved a short term Rolled Thin Film Oven Test (RTFOT) with air-blowing procedure. For long term ageing comparisons, Pressure Ageing Vessel (PAV) ageing was compared with ageing in an environmental room maintained at 60^{o}C. Before that, all samples were RTFOT short term aged to simulate the hot-mix production process. It was found that 38 days of ageing in 1-mm thick films at 60^{o}C and 1 atm of air was approximately equivalent to 20 hours in the PAV in 3.2mm thick films at 100^{o}C, after RTFOT aged.

2. Material Characteristics

2.1 Aggregate

Crushed granite aggregates used for preparing asphalt concrete mixture were supplied by Yen Bumi Sdn. Bhd. The aggregates were re-crushed using a vertical shaft impact crusher shown in Figure 2, available in the laboratory of the School of Materials and Mineral Resources Engineering of the Universiti Sains Malaysia. The basic engineering properties of the geometrically cubical re-crushed aggregates is shown in Table 1.

2.2 Materials for Asphalt Mixes

The gradation of the HMA mixes met the requirements for the Malaysian Public Works Department ACW14 for wearing courses (JKR 1988) as depicted in Figure 3. The median gradation was regarded as the target gradation. Binder types used were a conventional binder (penetration grade 80/100) and an SBS polymer modified binder. The method of optimum binder content (OBC) determination based on the Marshall method of mix design is available in another literature (Hamzah et al., 2006). A total of 24 samples were prepared to determine the OBC and the result for mixes incorporating irregularly and geometrically shaped aggregates are shown in Table 2. Table 3 provides a guide on mix designation.

2.3 Dynamic Creep Test

The dynamic creep test was developed to estimate the rutting potential of asphalt mixes. This test was conducted using the Asphalt Universal Testing Machine, MATTA in accordance with the procedures outlined in ASTM D4123 (ASTM, 2005). The test parameters adopted are summarized in Table 4. Actual dynamic creep test was conducted at 40^{0}C, 1 hour loading time and 0.1 MPa applied stress.

2.4 Aging of Bituminous Mixtures

Short-term ageing was carried out on loose mix according to AASHTO R30-02 (AASHTO, 2002) procedures. The method consisted of curing mix samples in a forced-draft oven at 135°C for 4 hours. After curing, the samples were brought to the compaction temperature and compacted via impact mode. The long term ageing was carried out on compacted specimens after subjected to short term ageing. Specimens were placed in a forced-draft oven at 85°C for five days. To accelerate ageing, ultra-violet light was incorporated. After the aging period, the oven was turned off and allowed to cool to room temperature. The specimens were then extruded and tested for dynamic creep.

3. Result and Discussion

3.1 Dynamic Creep Behaviour of Unaged Mixes

The effect of temperature on dynamic creep of all unaged asphaltic concrete mixtures tested is shown in Table 5. In general, the dynamic creep at 40^0C is much higher compared to the corresponding value at 60^0C. The increase ranges from as low as 11.9% to as high as 107.7%. The positive effects of using geometrically cubical shaped aggregates can be seen from the overall results summarized in Table 5. Generally, mixes incorporating geometrically cubical shaped aggregates perform better than mixes with aggregates crushed using the conventional compression crusher. The percentage increase in creep stiffness is more pronounced with conventional mixes tested at lower temperatures. For instance, when tested at 40^oC, at binder content 5.5%, the creep stiffness of IK mix is 14.5 MPa but the stiffness modulus of HMA mixtures with CK mix is 21.4 MPa which represents a 47.6% increase. Table 5 also shows that the SBS mixes exhibit the highest creep stiffness compared to the conventional mix type. On average, the creep stiffness of the SBS mixes is 29% more compared to conventional mixes when tested at 40^oC. Within the limited range of binder content investigated, the appear to be no relationship between percentage increase in stiffness versus binder content though there is a general tendency for the stiffness to increase as binder content increases but reduces beyond the maximum value.

3.2 Effect of Short Term Ageing on Creep Stiffness

Table 6 shows the creep stiffness results of mixes at their respective OBC after exposure to short term ageing. The unaged results are shown for comparative purposes. On average, subjecting mixes to short term ageing causes an increase in stiffness by approximately 10.5% when tested at both temperatures. However, the general trend remains as in unaged mixes, namely mixes become less resistant to permanent deformation at higher temperature. An increase in 20^oC test temperature can reduce the creep stiffness of STA mixes by 15.8%. Resistance to permanent deformation of STA mixes can be increased by up to 26% by incorporating geometrically cubical aggregates. Compared to conventional mixes with irregularly shaped aggregates, the creep stiffness of SBS modified mixes with shaped aggregates subjected to STA can be significantly increased by up to nearly 50%.

3.3 Relationship between Cumulative Strain and Time of Loading for STA Mixes

Figures 4 and 5 show the relationship between logarithm of cumulative creep strain and logarithm of loading time of specimens tested at 40^oC and 60^oC respectively. There is an initial absence of data due to pre-conditioning which was necessary to obtain a proper seating of the test platens on the specimen prior to the actual creep test. A log-log graph was plotted to linearise the original accumulated strain versus loading time curve. Nevertheless, the resulting graph is not entirely linear but consisting of two straight lines of different slopes. The first straight (primary line) has a steeper slope 'm' compared to the gradient of the second curve (secondary line). The y-intercept 'c' represents the extrapolated permanent strain at loading time equals 1, while the slope of the line represents the rate of change in permanent strain as a function of the change in loading time. The slope therefore indicates the sensitivity of mix to rutting. The resistance to permanent deformation of a mix is expected to increase when the relative intercept becomes less and the slope of the line decreases. Table 7 presents the coefficients of the linear regression for both primary and secondary lines. An attempt was also made to regress all test results into a single linear equation and the coefficients of the linear regression are also shown in Table 7. A comparison of the regression constants for all mixes after STA indicates that:

- The 'm' for unaged mixes is higher compared to STA mixes. Hence, ageing of mix causes a reduction in creep susceptibility.
- SBS mixes exhibit the lowest slope compared to conventional 80/100 mixes.
- Mixes with geometrically cubical aggregates show lower 'm' value compared to irregularly aggregates mixes.
- The modified mixtures indicate good permanent deformation characteristics compared to the conventional unmodified mixes.
- For all mixes tested, the 'm' value increases when the temperature increases.

It can be concluded that mixes subjected to STA, modified mixes and mixes incorporating geometrically cubical aggregates are the least susceptible to creep. However, mixes also become more sensitive to creep stiffness as temperature increases.

3.4 Effect of Long Term Ageing and Ultraviolet on Dynamic Creep

A similar analysis is carried out for specimens subjected to LTA in addition to ultra-violet. The corresponding results are shown in Table 8. Compared to unaged mixes, a percentage increase of the creep stiffness by two-fold is observed on LTA samples, indicating the extent of binder hardening that has taken place during the LTA process. The conventional mix is found to be more adversely affected when its average creep stiffness increased by about 22.8% while the corresponding increase of the SBS modified bitumen is approximately 16%. As in previous findings, creep

stiffness reduces at higher test temperature. The average percentage reduction is slightly less compared to those of STA specimens but much less compared to unaged mixes. This phenomenon can be explained in terms of the binder of aged mixes that has hardened hence making them less susceptible to temperature changes. The effect of temperature change on creep stiffness is lesser with the degree of ageing.

3.5 Relationship between Cumulative Strain and Time of Loading for LTA Mixes

Figures 6 and 7 illustrate the linear relationships between cumulative strain versus loading cycles plotted on a logarithmic scale. As in Section 3.3, the regression coefficients of the primary, secondary and single lines are summarized in Table 9. Similar trends with STA results are evident. The conventional and irregularly shaped mixes are more susceptible to ageing compared to mixes incorporating modified and geometrically cubical aggregate. The average 'm' for unaged, STA and LTA mixes are respectively $6.56x10^{-6}$, $3.61x10^{-6}$ and $1.86x10^{-6}$ respectively. It can be infer that each ageing process reduce mix sensitivity to creep by a half. Mixtures become less sensitive to creep at lower temperature as the bitumen becomes stiffer.

4. Conclusions

An increase in creep stiffness can be achieved when geometrically cubical re-crushed aggregates are used in asphaltic concrete mix compared to uncrushed irregularly shaped aggregates mix. An improvement in creep stiffness values is observed when SBS modified binder is used. Within the small range of binder content tested, there appear to be an optimum stiffness value for all mixes. Generally, mix creep stiffness reduces when the test temperature increases from 40^0C to 60^0C. The reduction is more pronounced with unaged mixes. The effect of ageing is to increase the creep stiffness but reduces the mix susceptibility to creep over time. The combined effect of geometrically cubical aggregates and modified binder can improve the creep stiffness to nearly 50%.

Acknowledgements

The financial support provided by Universiti Sains Malaysia in the form of a short term research grant for this study is very much appreciated. The authors wish to acknowledge the technicians of Highway Engineering Laboratory, School of Civil Engineering and technicians of Material Engineering, School of Materials and Mineral Resources Engineering for their help in carrying out the laboratory works. We also acknowledge Metso Minerals for loaning the Barmac Rock on Rock Vertical Shaft Impact (RoR VSI) crusher that enable preparation of the re-crushed aggregates to be made.

References

AASHTO. (2002), Mixture Conditioning of Hot Mix Asphalt. Standard Specification for Transportation Materials and Methods of Sampling and Testing. *AASHTO R30-02 Part 1B*, American Association of State Highway and Transportation Officials.

ASTM. (2005). Test Method for Indirect Tension Test for Resilient Modulus of Bituminous Mixtures. ASTM D4123, *Annual books of ASTM Standard*, Volume 04.03.

Campen, W. H., Smith, J. R. (1948). A Study of the Role of Angular Aggregates in the Development of Stability and Bituminous furies. *Proc. AAPT,* Vol. 17.

Daniel B. Knorr, J., Richard R. D., and Charles J. G. (2002). Effect of Various Aging Techniques on Asphalt Low-Temperature Properties. *Transportation Research Record 1583*, TRB, Washington, D. C., Pp: 37-44.

Hamzah M.O, Ramadhansyah P.J, Khairun Azizi M.A (2006). Effects of Temperature and Binder Types on Resilient Modulus of Asphaltic Concrete. *National Seminar on Civil Engineering Research (SEPKA), Universiti Teknologi Malaysia*, Johor, December 2006.

JKR. (1988). "Standard Specifications for Road Work", *Jabatan Kerja Raya Malaysia*, Kuala Lumpur.

Kamal, M. A., Shazib, S, and Yasin, B. (2005). Resilient behaviour of asphalt concrete under repeated loading & effects of temperature. *Journal of the Eastern Asia Society for Transportation Studies*, Vol. 6, pp. 1329 – 1343.

Parker F. and Brown E.R. (1992). 'Effects of Aggregate Properties on Flexible Pavement Rutting in Alabama', *ASTM STP 1147*, pp. 68-89.

Wedding, P. A., Gaynor, R. D. (1961). The Effects of Using Crushed Gravel as the Course and Fine Aggregate in Dense Graded Bituminous Mixtures. *Proc. AAPT*, VO1.30.

Zhao, Y. (2002). Permanent Deformation Characterization of Asphalt Concrete Using a Viscoelastoplastic Model. *Thesis Doctor of Philosophy*. Department of Civil Engineering. Raleigh, North Carolina.

Table 1. Aggregate Properties Used in the Mix

Property	Test Value of Aggregate Shape	
	Irregularly Shape	**Geometrically Cubical**
Flakiness Index (%)	17.57	7.94
Elongation Index (%)	33.24	11.89
Aggregate Crushing Value (%)	21.77	18.11
Aggregate Impact Value (%)	25.98	22.22
Water Absorption (%)	0.74	0.59

Table 2. Optimum Binder Content of the Mixes Investigated

Mix Type	Optimum Binder Content (%)	
	Irregularly Shaped	**Geometrically Cubical**
Conventional Mixes	5.0	4.8
SBS Modified Mixes	5.0	4.7

Table 3. The Mix Designation of Ageing Test

Binder Types	Aggregate Shape	Mix Conditioning	Mix Designation
80/100	Geometrically	Unaged	CK
	Irregularly	Unaged	IK
	Geometrically	Short Term	CKS
	Irregularly	Short Term	IKS
SBS	Geometrically	Unaged	CS
	Irregularly	Unaged	IS
	Geometrically	Short Term	CSS
	Irregularly	Short Term	ISS
80/100	Geometrically	Long Term	CKL
	Irregularly	Long Term	IKL
SBS	Geometrically	Long Term	CSL
	Irregularly	Long Term	ISL

Table 4. The Dynamic Creep Test Parameters Adopted in this Study

Parameter	Duration
Pulse period (ms)	1000
Pulse width (ms)	200
Test Loading Stress (kPa)	100
Terminal Pulse Count	3600

Table 5. Dynamic Creep Stiffness of Unaged Asphalt Mixes Incorporating Cubical and Irregularly Shaped Aggregates

Binder Type	**Mix Designation**	**Binder Content (%)**	**Creep Stiffness at Test Temperature**	
			40°C	**60°C**
Conventional 80/100	IK	4.5	14.5	12.7
		5.0	20.5	17.7
		5.5	18.6	12.4
	CK	4.3	21.4	13.7
		4.8	24.4	21.8
		5.3	20.0	12.8
SBS Modified	IS	4.5	19.6	15.2
		5.0	24.4	19.1
		5.5	23.1	12.7
	CS	4.2	26.3	15.9
		4.7	30.6	25.6
		5.2	29.5	14.2

Table 6. Dynamic Creep Stiffness (MPa) of Short-Term Aged Asphalt Mixes Incorporating Cubical and Irregularly Shaped Aggregates

Binder Type	**Mix Designation**	**Un-Aged**		**STA**	
		Temperatures (^{0}C)		**Temperatures (^{0}C)**	
		40°C	**60°C**	**40°C**	**60°C**
80/100	IK	20.5	17.7	22.8	18.7
	CK	24.4	21.8	27.6	24.3
SBS	IS	24.4	19.1	26.5	22.3
	CS	30.6	25.6	33.4	27.6

Table 7. Coefficients of the Linear Relationship between Log Cumulative Strain and Log Time of Loading for Primary, Secondary and Single Lines of STA Compared with Unaged Mixes

Type of Ageing			**Un-aged**			**Short Term Ageing**		
Primary Line								
Binder Type	**Mix Desig-nation**	**Tempe-rature (°C)**	**m ($1x10^{-6}$)**	**c ($1x10^{-3}$)**	**R^2**	**m $1x10^{-6}$)**	**c ($1x10^{-3}$)**	**R^2**
80/100	IK	40	71.5	44.2	0.78	32.2	29.4	0.78
	CK		51.6	40.2	0.80	29.2	29.4	0.77
SBS	IS		44.1	35.2	0.76	27.5	29.0	0.78
	CS		44.1	33.3	0.78	27.5	25.0	0.78
80/100	IK	60	38.2	33.3	0.76	23.0	23.5	0.78
	CK		37.7	33.1	0.80	22.5	23.1	0.78
SBS	IS		35.1	32.3	0.77	20.5	21.8	0.79
	CS		34.8	30.3	0.76	19.5	19.3	0.79
Secondary Line								
80/100	IK	40	6.9	62.6	0.94	3.7	41.6	0.96
	CK		6.5	58.6	0.94	3.5	41.6	0.96
SBS	IS		6.2	54.6	0.94	3.5	35.9	0.96
	CS		5.0	51.2	0.95	2.6	35.0	0.97
80/100	IK	60	4.8	49.9	0.95	2.5	34.5	0.97
	CK		4.5	47.2	0.96	2.3	32.3	0.97
SBS	IS		4.3	47.0	0.96	2.3	30.8	0.97
	CS		4.0	46.2	0.96	2.3	27.8	0.97
Single Line								
80/100	IK	40	8.8	56.9	0.85	4.9	38.5	0.80
	CK		8.2	55.1	0.72	4.6	38.5	0.80
SBS	IS		6.8	49.5	0.75	3.5	33.6	0.81
	CS		6.3	46.6	0.72	3.5	32.7	0.82
80/100	IK	60	6.1	45.8	0.79	3.4	32.2	0.83
	CK		5.8	43.7	0.76	3.3	30.1	0.83
SBS	IS		5.3	43.3	0.76	3.0	28.6	0.82
	CS		5.2	42.3	0.80	2.7	25.7	0.82

Table 8. Dynamic Creep Stiffness (MPa) of Long Term-Aged Asphalt Mixes Incorporating Cubical and Irregularly Shaped Aggregates

Binder Type	Mix Designation	Un-Aged Test		LTA Test Temperature	
		40°C	60°C	40°C	60°C
80/100	IK	20.5	17.7	24.9	21.7
	CK	24.4	21.8	30.3	27.3
SBS	IS	24.4	19.1	28.7	23.8
	CS	30.6	25.6	35.1	29.9

Table 9. Coefficients of the Linear Relationship between Log-Cumulative Strain and Log-Time of Loading for Primary, Secondary and Single Line soft LTA Compared with Unaged Mixes

Type of Ageing			Un-aged			Long Term Ageing		
Primary Line								
Binder	**Mix**	**Tempe-rature**	**m**	**c**	**R^2**	**m**	**c**	**R^2**
80/100	IK	40	71.5	44.2	0.78	17.8	18.2	0.85
	CK		51.6	40.2	0.80	17.5	16.2	0.84
SBS	IS		44.1	35.2	0.76	14.8	12.3	0.80
	CS		44.1	33.3	0.78	13.0	9.0	0.82
80/100	IK	60	38.2	33.3	0.76	11.3	7.8	0.80
	CK		37.7	33.1	0.80	11.0	7.3	0.80
SBS	IS		35.1	32.3	0.77	10.4	6.2	0.80
	CS		34.8	30.3	0.76	9.2	4.2	0.80
Secondary Line								
80/100	IK	40	6.9	62.6	0.94	1.8	25.5	0.99
	CK		6.5	58.6	0.94	1.8	23.6	0.98
SBS	IS		6.2	54.6	0.94	1.5	17.8	0.97
	CS		5.0	51.2	0.95	1.4	12.9	0.98
80/100	IK	60	4.8	49.9	0.95	1.4	12.7	0.98
	CK		4.5	47.2	0.96	1.4	10.6	0.98
SBS	IS		4.3	47.0	0.96	1.2	10.4	0.98
	CS		4.0	46.2	0.96	1.2	9.2	0.98
Single Line								
80/100	IK	40	8.8	56.9	0.85	2.4	23.7	0.84
	CK		8.2	55.1	0.72	2.3	21.8	0.83
SBS	IS		6.8	49.5	0.75	2.0	16.5	0.89
	CS		6.3	46.6	0.72	1.9	11.9	0.86
80/100	IK	60	6.1	45.8	0.79	1.9	11.4	0.85
	CK		5.8	43.7	0.76	1.8	9.6	0.85
SBS	IS		5.3	43.3	0.76	1.6	9.5	0.85
	CS		5.2	42.3	0.80	1.0	7.8	0.85

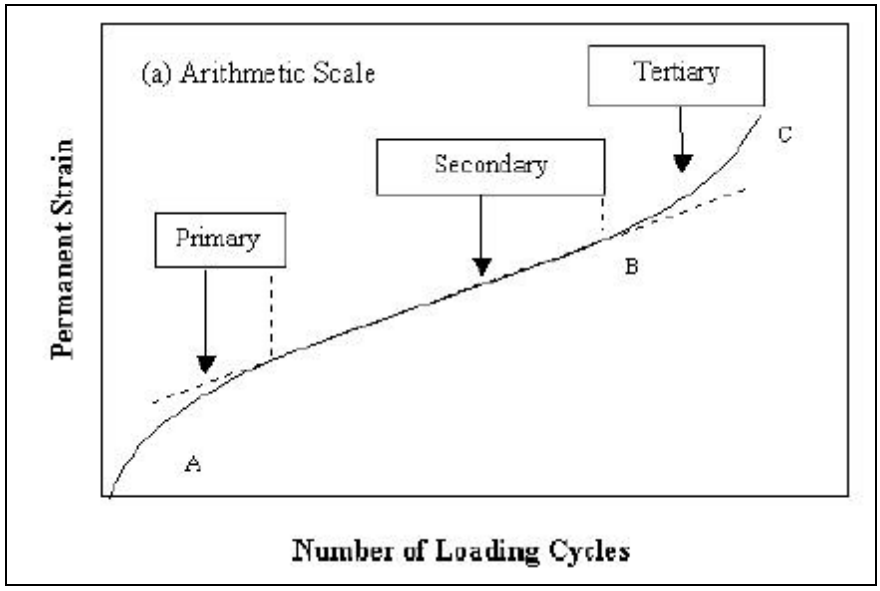

Figure 1. Typical Relationships between Permanent Strain and Number of Loading Cycles in Normal Scale (Zhao, 2002)

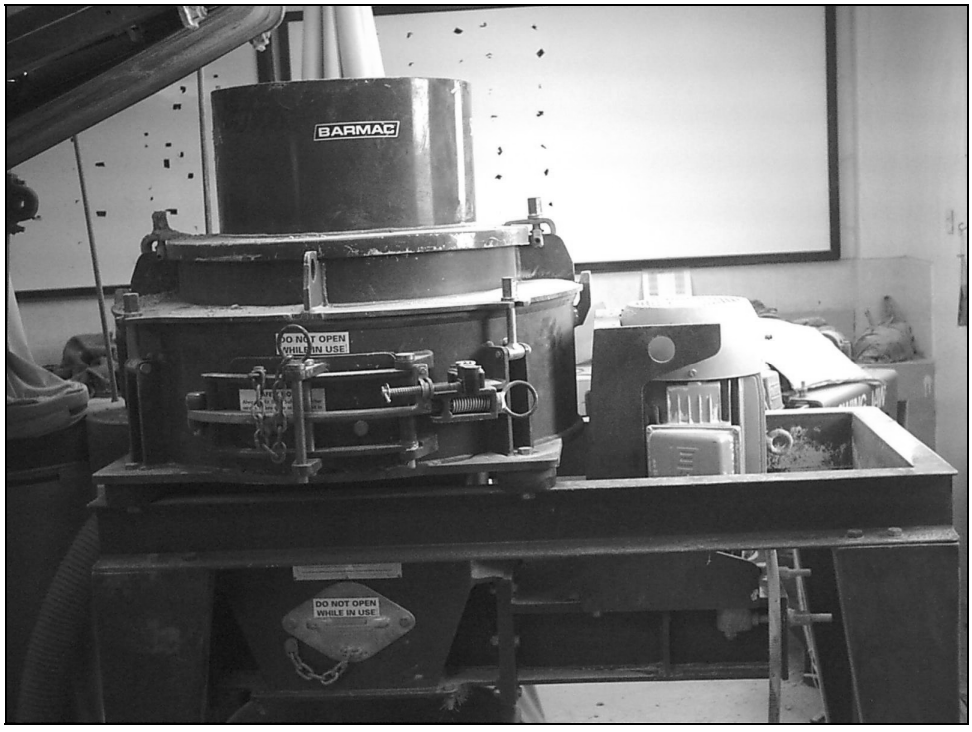

Figure 2. Vertical Shaft Impact Crusher Used to Crush the Aggregates

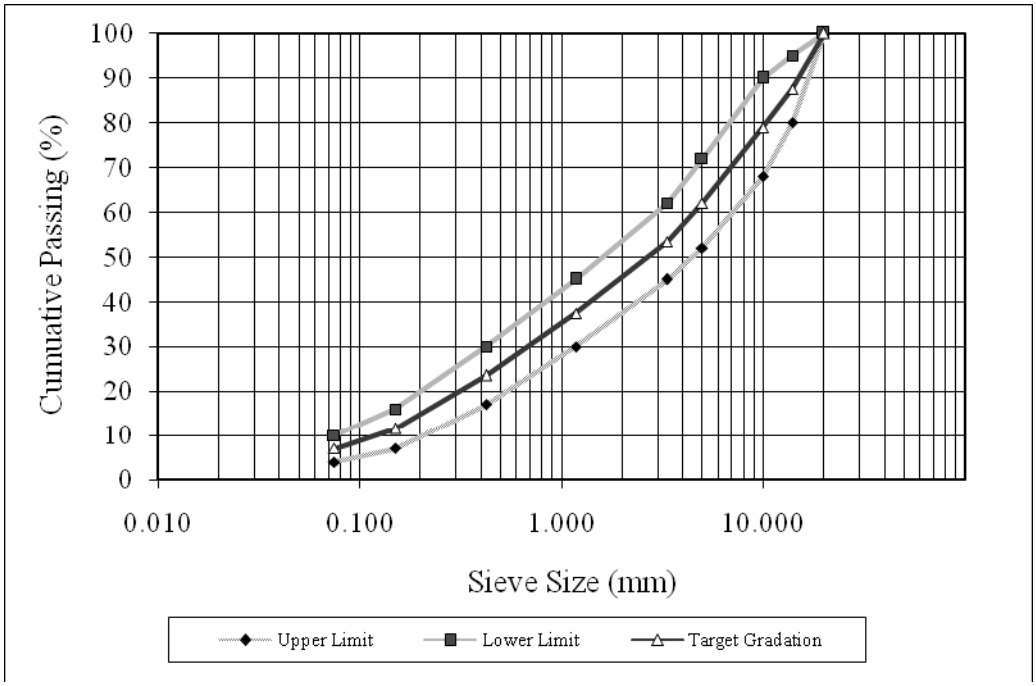

Figure 3. JKR Gradation Limits for ACW14 Used in this Investigation (JKR, 1988)

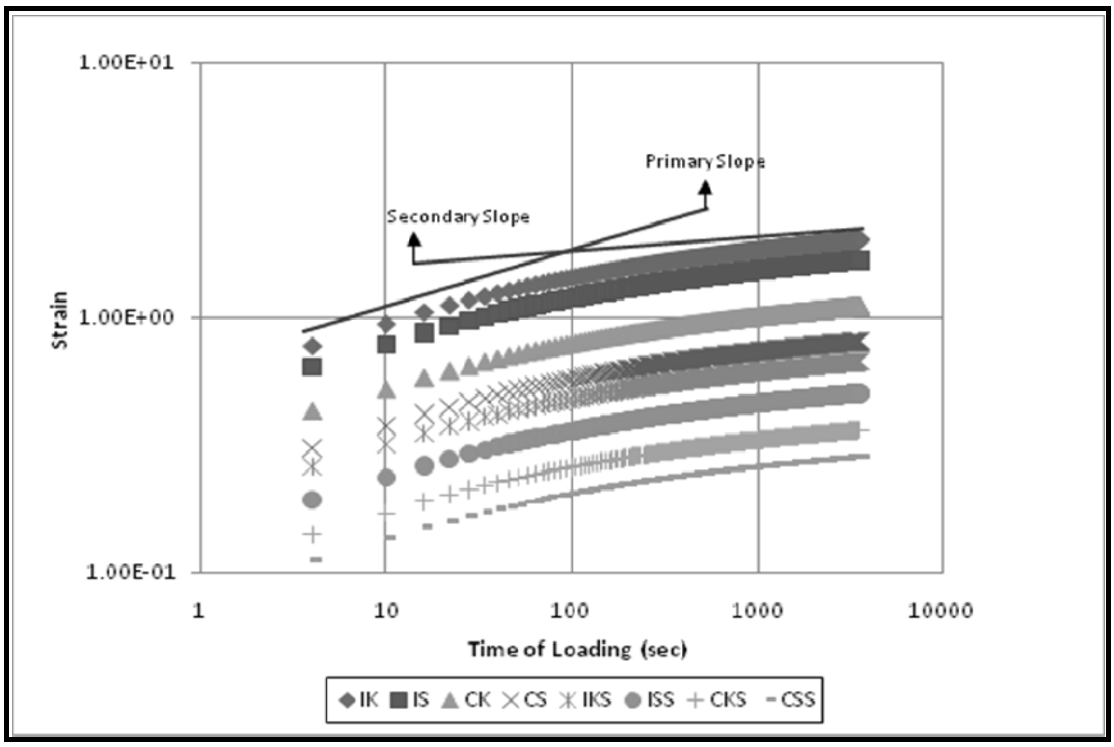

Figure 4. Relationship Between Log Cumulative Strain Versus Log Time of Loading (Test Temperature 40°C)

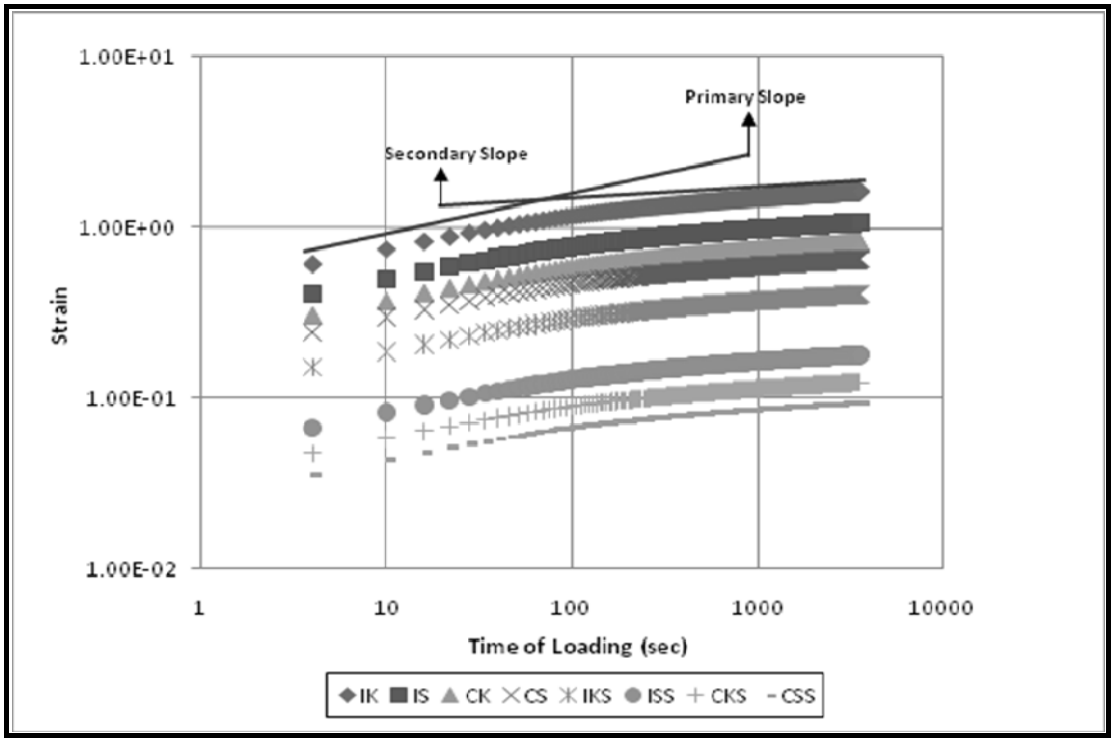

Figure 5. Relationship Between Log Cumulative Strain versus Log Time of Loading (Test Temperature 60^{o}C)

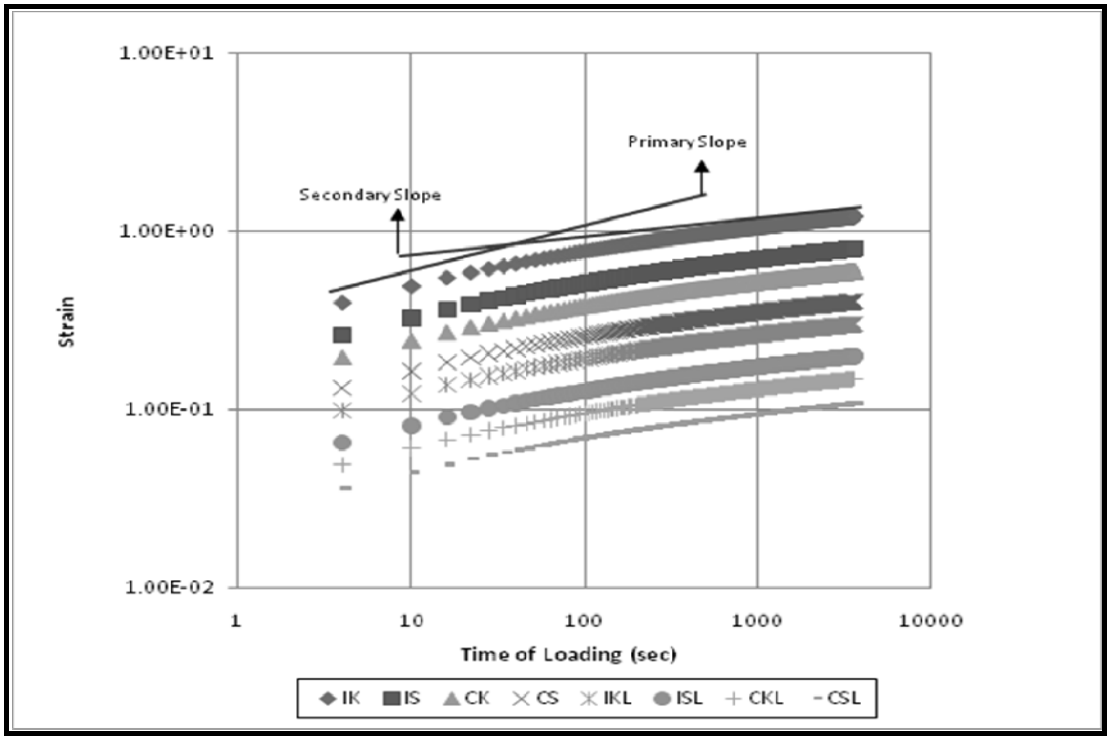

Figure 6. Graphical Determination of Primary and Secondary Slopes Log-Cumulative Strain versus Log-Time of Loading at 40^{o}C

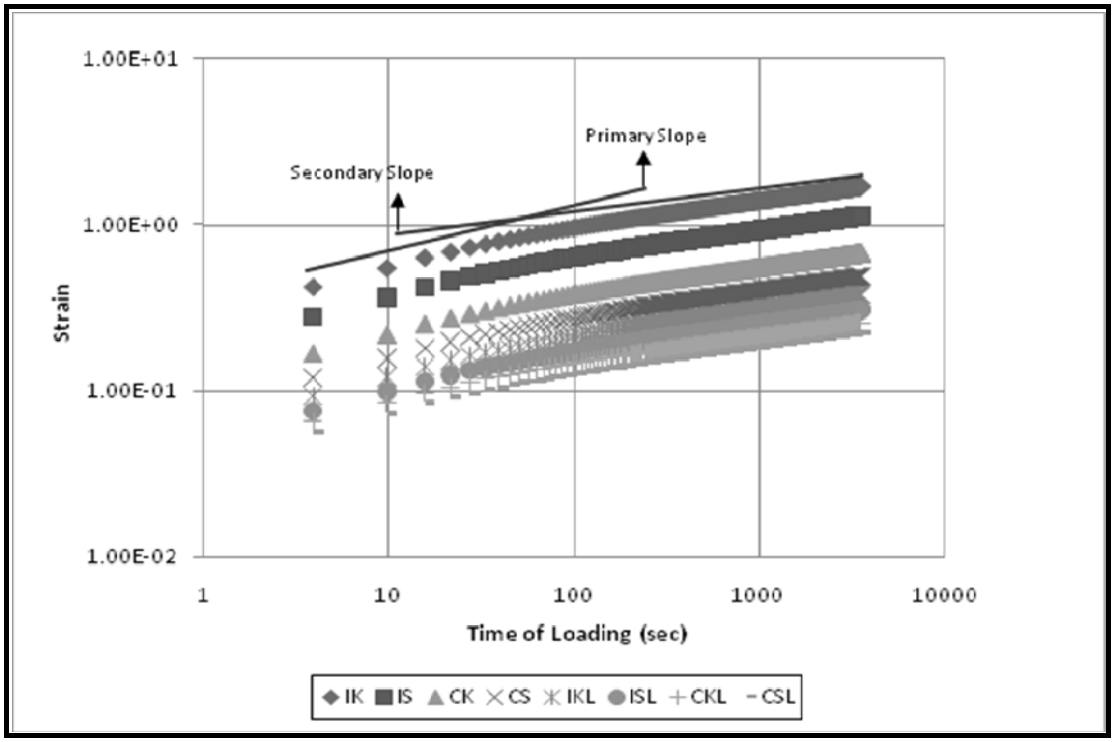

Figure 7. Graphical Determination of Primary and Secondary Slopes Log-Cumulative Strain versus Log-Time of Loading at 60^{o}C

Modern Applied Science

www.ccsenet.org/journal.html

Vol. 3, No. 7

July 2009

An Embedded System of Real-Time Acquisition and Display of Images

Yuwei Peng

The School of Science, Wuhan University of Technology, Wuhan 430070, China

E-mail: peng_yuwei@hotmail.com

Fen Leng

The School of Information Engineering, Wuhan University of Technology, Wuhan 430070, China

E-mail: lengfen_711@163.com

Abstract

In this paper, we propose a design of an embedded system which based on CPLD (Complex Programmable Logic Device) and only one chip of SRAM (Static RAM) in order to acquire and display the images real-time. The system uses Omni Vision's CMOS color image sensor OV7725 as the image acquisition chip and a 5.6-inch TFT-LCD (Thin Film Transistor Liquid Crystal Display), 18bit (RGB666) colors with resolution of 640 × 480 pixels, to display the images real-time, and the device of CPLD (EPM7160E) to control the timing, image format conversion, and TFT-LCD drive signal. At the same time the embedded system use one chip of SRAM as a cache memory to save an image quickly. The experimental results show that the system designed, with high practical value but less hardware, is easy to capture and display the images stably.

Keywords: CPLD, SRAM, CMOS, TFT-LCD, Embedded system

1. Introduction

As embedded systems are presses to deliver greater real-time performance in smaller form-factors with less power, designers must increasingly turn to application-specific design solutions. With the development of CMOS sensor, the embedded image-acquisition system develops fast. A LCD is a standard display device for hand-held embedded systems. As a result of it, the LCD is used for the embedded display system more often.

In tradition, there are several methods to drive the TFT-LCD, such as taking the FPGA and Double Access RAM, and even use two chips of SRAM in Ping-pong mechanism. In these ways, the system wastes too much hardware resource. On the other hand, the continuous images and video data usually transfer throughout the system by the modes of VGA (Video Graphics Array) interface and AV (Audio and Video Composite video connector) interface, the system which transfers the image and video by these interface needs the ADC (Analog to Digital Converter) and DAC (Digital to Analog Converter) of image and video data, and the coder and decoder devices, this solution also increase the cost of the whole embedded system.

For the above reasons, we propose a design of an embedded system for image acquisition and display. In this system, we use a CMOS sensor to acquire images, a TFT-LCD to show the images, a CPLD and only one chip of SRAM to accomplish the functions.

2. The hardware of system

The embedded system uses CPLD as the core unit to control the timing of this whole system, transform the data format of the real-time images, and control the SRAM in order to read and write the data of the real-time images, at last, the CPLD also generates the signals to drive the TFT-LCD in order to show the images on the screen of LCD.

We use the VHDL (Very-High-Speed Integrated Circuit Hardware Description Language) with the software MAX+PLUS Ⅱ, a development of integrated environment provided by the Altera for FPGA (Field-Programmable Gate Array) and CPLD, to design the functions of the CPLD in the embedded system.

The structure of the embedded system is shown in Figure 1.

In this system, we take the OV7725 as the main CMOS image senor device. The OV7725 Camera Chip sensor is a high performance 1/4 inch, single-chip VGA camera and image processor in a small footprint package. The OV7725 incorporates a 640×480 image array, capable of operating at 60 frames per second in VGA mode with complete user control over image quality, formatting and output data transfer. It also has automatic image control functions including AEC (automatic exposure control), AGC (automatic gain control), AWB (automatic white balance), ABF (automatic band filter), and ABLC (automatic blacked-level calibration). In order to make the OV7725 to work, we should set the register by standard SCCB interface.

We choose the EPM7160E serious CPLD as the main control chip. Which is a product of Altera, there are 3,200 usable gates, 160 macro cells and 104 I/O pins (maximum) in this chip.

In this system, the image we acquired is a constitution of 640×480 pixels with the format of RGB555. A frame image takes 307,200 words by 16bit. In order to save the data of a frame image, we use the IS61LV51216, A production of ISSI, a high-speed, 8M-bit static RAM organized as 525,288 words by 16 bits.

We use a 5.6-inch digital TFT-LCD, provided by the InnoLux, as the device of displaying the images. This TFT-LCD has 18bit colors in depth, and has a resolution of 640×480 pixels.

3. The settings of OV7725

The OV7725 has an image array capable of operating at up to 60 frames per second (fps) in VGA with complete user control over image quality, formatting and output data transfer. Its image quality controls include color saturation, hue, gamma, sharpness (edge enhancement level auto adjust), and anti-blooming.

The OV7725 should be set by standard SCCB interface in order to work. In this system, we should set several registers, and other registers could be set as the default value. In the embedded system, the OV7725 should output the image data with the mode of 640×480 pixels, RGB555, and 60fps.

In order to output the image in the mode of 640×480 pixels, six registers should be set in the table 1.

In order to output the data in the format of RGB555, the register COM7, address in 0x12, should be set as 0x0A.

In order to output 60 frames per second, the 48MHz crystal should be used as the main system input clock for the OV7725.

The sequence of the output image data is from left to right and from up and down, each line has 640 effective pixels, and each frame image has effective 480 lines. The scanning sequence of a frame image is shown in the Figure 2.

In this system, we use the MCU (Micro Controller Unit) to set the registers of OV7725 before it is used to collect the images. Because of the method of setting registers through SCCB bus and most MCU contains I^2C module rather than SCCB module, we use the MSP430F149, a production of TI, to simulate the SCCB bus in order to set the OV7725.

The VGA frame timing diagram is shown in the Figure 3. Because of one pixels is made up of two bytes in the mode of VGA and RGB555, one HERF signal contains 1280 clocks rather than 640 clocks in the mode of QVGA in RGB555.And the image data output pins, D9-D2, output the 8-bit data. The data format is shown in the table 2.

4. The TFT-LCD

The TFT-LCD used in the embedded system has a constitution of 640×480, and could show 18bit colors in one pixel. The drive signals of this LCD are made up of VSYNC, HSYNC, DE (or HV), PIXCLK and RGB data in 18bit, R [5:0], G [5:0], and B [5:0]. The logical supply power is 3.3V and the power for the back LED is 5V. The timing diagram is shown in the Figure 4. A frame image being displayed in the screen of LCD has 525 lines, and there are default 13 lines before the effective lines and 32 lines after the effective lines which contains 480 lines; At the same time, each line signal has 800 CLKINs, and the effective RGB data contains 640 CLKINs, there are default 144 CLKINs invalid before the effective CLKINs and 16 CLKINs invalid after the effective CLKINs. This LCD could work in the modes of DE or HV. In this system, we use the DE mode; the signal of DE decides the effective CLKINs which require the RGB data in each line. The display method of LCD could be set by the L/R and U/D. L/R decides whether the display works from left to right or right to left, and the U/R decides the LCD display from up to down or down to up. The settings of these two pins could achieve the screen flipping.

5. The function of CPLD

As it shown in the Figure 1, the CPLD has four modules: Decoder, Write SRAM, Read SRAM, and TFT-LCD Driver.

5.1 The Decoder Module

The Decoder module of the CPLD is to acquire and transform the data format of image. In digital image, the value of one color could be made up by values of Red, Green, and Blue. The OV7725 outputs the image data format with RGB555 in two 8bit bytes, as well as the controlling signals of VSYNC, HREF, and PCLK. Firstly, we should acquire the effective RGB data through these controlling signals; secondly, we should transform the data into a 16bit word in

order to save and process in the further. The origin data format is shown in table 2. The highest bit in the first byte is not used in the mode of RGB555.

The transformed data format is shown in the table 3. That is, we merge the first byte and the second byte into a word, and the highest bit is not used.

5.2 The Write SRAM Module

While receiving the data, CPLD sets the SRAM as the mode of write-only by the control signal of WE, OE, and CE. At the same time, the Wring SRAM module saves the image data into the IS61LV51216 with the method of cumulative. For example, The RGB data of the first pixels, the first line and the first dot, is saved at the address 0X00000, and the second RGB data of the second pixel, the first line and the second dot, is saved at the address 0X00001, and so on. Followed by analogy, the last RGB data of the whole image, the 640th line and the 480th dot, is saved at the address 0X4AFFF. The address and data are shown in the table.4.

These address signals are generated by the count of the clock input. In this system, we use the 48MHz crystal to generate the clock signal for the OV7725 and the CPLD.

5.3 The Read SRAM and TFT-LCD Driving Modules

When a frame image data saved successfully, the CPLD gives the control signal of WE, OE, and CE, to set the SRAM only to be read and not to be written. The Read SRAM and the TFT-LCD driver modules of the CPLD then read the data by cumulative. Because the TFT-LCD has 18bit colors with RGB666, but the image data saved in the SRAM is RGB555, we set the lowest bit of R[5:0], G[5:0], and B[5:0] as '0'. That is, the R5 sent to the TFT-LCD is the R4 saved in the SRAM. The R(n) sent to the TFT-LCD is the R(n-1) saved in the SRAM. (n=1.2.3.4.5.) And the R0 sent to the TFT-LCD is '0', as well as G[5:0] and B[5:0]. With the timing signals of VSYNC, HSYNC, DE, PIXCLK, the image data, made up of the format RGB666, also be sent to the TFT-LCD, the TFT-LCD received these signals and dates to show the image clearly.

6. The implementation of the embedded system

Throughout the system, the output images data of OV7725 are 60fps, that is to say, the OV7725 outputs 60 images in one second. But in the application of real-time display, according to the human eye's visual effect of temporary stay, as long as 24 frame images in one second the human would feel that the images are changing smoothly and continuous, and the smear, flicker, pause could not be recognized. In order to save the hardware resource without decreasing the effective of the images showing, we use 30 images, one half the output images of the OV7725. The specific process is like this:

When the OV7725 outputs the first frame image, the SRAM is set by the WE, CE, and OE to the write-only status, the Decoder and Writing SRAM modules of CPLD transform and save this frame image into the SRAM. When a frame image saving is finished successfully, the CPLD then gives control signals, WE, CE, and OE, to set the SRAM for read-only status. The Read SRAM and TFT-LCD driving modules read the data from SRAM and send the data with the TFT-LCD driving signals, VSYNC, HSYNC, DE, and PIXCLK, to TFT-LCD. In this reading process, the OV7725 is still output the second frame image, but the SRAM is set to be read only, so the system does not acquire this image data, that is, the system discard this frame image and does not save it. When the TFT-LCD of the system finished the showing a frame image, the CPLD then sets the SRAM to be written-only, and then acquires the third frame like the first frame. In the time of writing SRAM, the TFT-LCD does not refresh the image until the SRAM is set to read-only again.

In this method, OV7725 output 60 frames images and we only display one half, 30 frames. And it does not have influenced our visual and later process, such as detecting the moving objects and the process of real-time robotic vision.

7. Conclusion

Through using this real-time acquisition and display embedded system, we find that the images are displayed continuous, without flicker and lose frame phenomenon. Experiment confirmed that the embedded system of using CMOS to acquisition and the LCD to display the images based on CPLD and one SRAM is possible. In this way, the embedded system decreases the hardware resource, and has a high relevance in a particular field. At the same time, the images are saved in the SRAM, therefore, the embedded system can be expanded with the high performance micro-processor, such as DSP (Digital Signal Process) chip, ARM (Advanced RISC Machines), FPGA and so on, to do the further process well. For example, the license plate recognition of the cars, the target objects detection.

References

Henrry Andrian and Kai-Tai Song. (2005). Embedded CMOS Imaging System for Real-Time Robotic Vision. Aug.2005, Digital Object Identifier.

Inseok Choi, Hojun Shim and Naehyuck Chang. (2002). Low-Power Color TFT LCD Display for Hand-Held

Embedded Systems.2002, ISLPED'02

Integrated Sillicon Solution, Inc. IS61LV51216 Data Sheet. Oct.2003, www.issi.com

Jeffrey Ammon, Carl Hein. (1997). VHDL-Based Performance Modeling: An Application of the PWM Tool Suite to an Image Classification System. 19-22 Oct. 1997, Digital Object Identifier.

MAX7000 Programmable Logic Device Family Data Sheet. June 2003, www.altera.com

OmniVision Serial Camera Control Bus(SCCB) Functional Specification. Feb.2003, www.ovt.com

OmniVision Technologies, Inc. OV7725 Adcanced Information Datasheet. December 17, 2007. www.ovt.com

OV7725 VGA product brief.2008.1 www.ovt.com

Xiancheng Fu, Xuecheng Zou, jianming Lei. (2006). The Design of Central Control Unit of LCD Controller. 2006.6, Microelectronics&Computer.

Table 1. The Registers and Value

Address	Register Name	Value
0x17	HSTART	0x26
0x18	HSIZE	0xA0
0x19	VSTRT	0x07
0x1A	VSIZE	0xF0
0x29	HOutSize	0xA0
0x2C	VOutSize	0xF0

Table 2. The output data format of OV7725

The first byte								The second byte							
×	R4	R3	R2	R1	R0	G4	G3	G2	G1	G0	B4	B3	B2	B1	B0

Table 3. The data format saved in one address

A Word															
×	R4	R3	R2	R1	R0	G4	G3	G2	G1	G0	B4	B3	B2	B1	B0

Table 4. The image data and address

Address	The image pixels data
0x00000	Line 1, the 1st pixels
0x00001	Line 1, the 2nd pixels
……	……
0x0027F	Line 2, the 1st pixels
0x00280	Line 2, the 2nd pixels
……	……
0x4AFFE	Line 480, the 639th pixels
0x4AFFF	Line 480, the 640th pixels

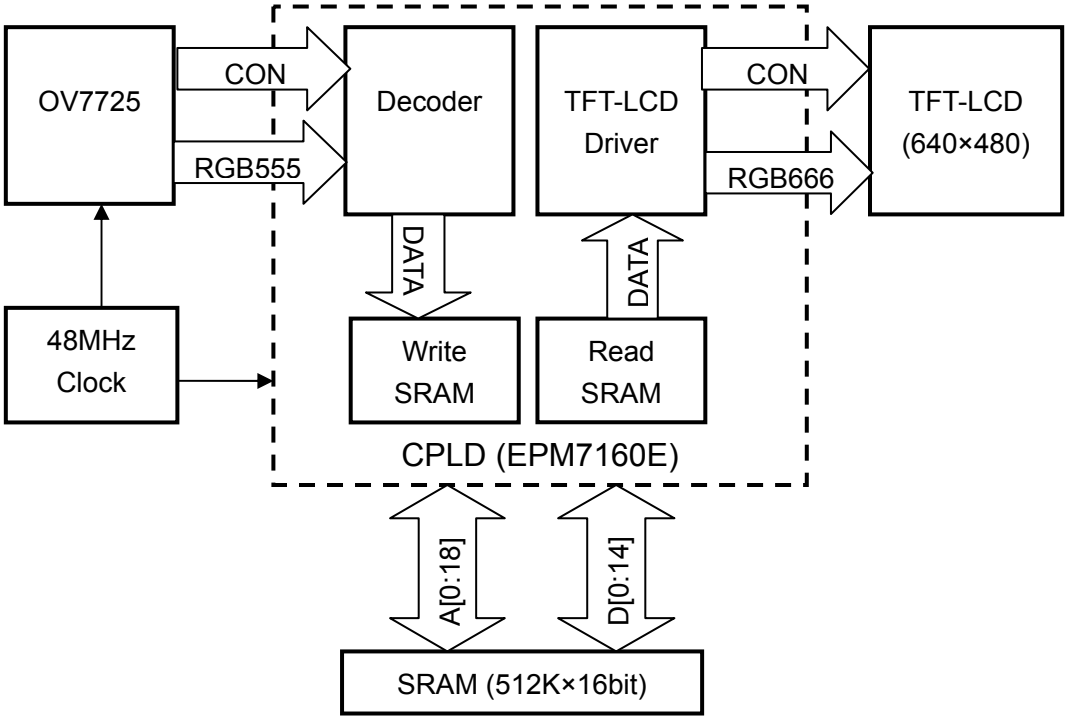

Figure 1. The hardware of the embedded system

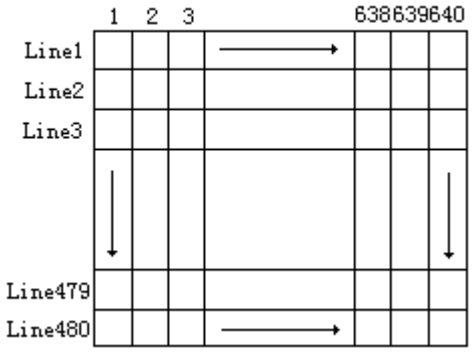

Figure 2. The scanning method of a frame image

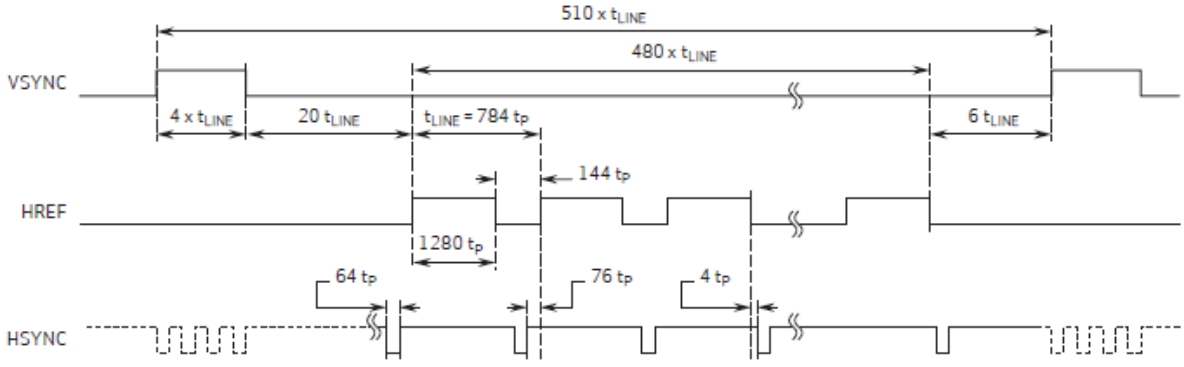

Figure 3. The output timing of OV7725

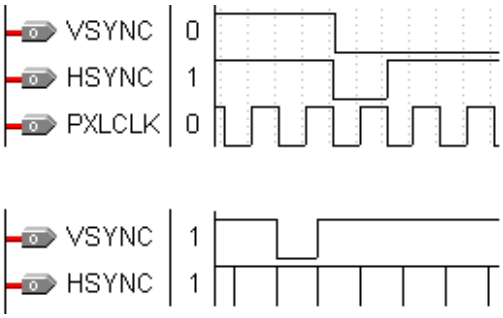

Figure 4. The timing of TFT-LCD driving Simulation by the MAX+PLUS Ⅱ

Modern Applied Science

www.ccsenet.org/journal.html

Vol. 3, No. 7

July 2009

Selection Criteria and Analysis of LCC Resonant DC – DC Converters for Automotive Applications

M. Prabhakar (Corresponding Author)
Department of EEE, Sri Venkateswara College of Engineering
Sriperumbudur, India – 602105
E-mail: prab@svce.ac.in

S. Arulmozhi
Department of EEE, Sri Venkateswara College of Engineering
Sriperumbudur, India – 602105
E-mail: arulmozhi@svce.ac.in

Dr. V. Kamaraj
Department of EEE, SSN College of Engineering
Kalavakkam, India – 603110
E-mail: kamarajv@ssn.edu.in

Abstract

In this paper, a technique is developed for the selection of LCC topologies for automotive applications. All available LCC topologies are categorised based on the order of their voltage gain expression. Source/sink requirement for automotive applications is specified based on which some topologies are found to be realizable. Voltage gain expressions for these topologies are obtained and plotted. From the voltage gain plot, two candidate topologies are chosen. Closed form expressions for current gain, stress across resonant tank elements, circulating reactive power and stored energy in the tank are obtained. In addition, the optimum value of Q which results in smallest possible resonant tank is determined and is found to be 0.545.

Keywords: Automotive applications, DC – DC converters, Resonant converters

1. Nomenclature

L	Inductance value of resonant inductor L.
C_1, C_2	Capacitance value of resonant capacitors C_1, C_2.
x	Ratio of capacitors.
Q	Loaded Q value of the resonant circuit.
R_L	Load resistance.
R_{eq}	AC equivalent of load resistance.
Z_n	Characteristic impedance of the resonant circuit.
Z_{in}	Input impedance of the resonant circuit.
ω	Angular switching frequency in radians per second.
ω_0	Angular resonant frequency in radians per second.
ω_n	Normalised switching frequency.

V_d Input dc voltage.

V_0 Output dc voltage.

M Voltage gain.

$V_{C1,rms}$ RMS value of voltage across capacitor C_1.

$V_{C2,rms}$ RMS value of voltage across capacitor C_2.

$V_{L,rms}$ RMS value of voltage across inductor.

$V_{C1,N}$ Normalised RMS voltage across capacitor C_1.

$V_{C2,N}$ Normalised RMS voltage across capacitor C_2.

$V_{L,N}$ Normalised RMS voltage across inductor L.

$V_{in,rms}$ RMS value of the fundamental component of square – wave voltage.

$I_{C1,rms}$ RMS value of current in capacitor C_1.

$I_{C2,rms}$ RMS value of current in capacitor C_2.

$I_{C1,N}$ Normalised RMS current in capacitor C_1.

$I_{C2,N}$ Normalised RMS current in capacitor C_2.

$I_{L,rms}$ RMS value of current in inductor L.

$I_{L,N}$ Normalised RMS current in inductor L.

I_0 Output dc current.

H Current gain.

2. Introduction

Resonant converters possess several desirable features like zero voltage switching (ZVS), zero current switching (ZCS), high frequency operation, high efficiency, small size and low electromagnetic interference (EMI). They have been successfully applied to dc power supplies for industrial, commercial and domestic applications. Due to the sinusoidal behavior of resonant converters, their switching losses are much reduced. Therefore, it is possible to operate these converters at high frequencies and thus reduce the size of their reactive components. Consequently, several of today's resonant DC – DC converter operates in megahertz frequency range (Robert L. Steigerwarld, 1984, Forsyth A.J, 1996). The series and parallel resonant converters are basic resonant converter topologies. Generally, the resonant tank consists of only two energy storage elements. Compared with the conventional second order resonant converters, higher order converters are shown to possess more desirable characteristics.

Resonant converter topologies in which the tank circuit consists of more than two or three energy storage elements have been reported in the open literature. A generalized analysis for the third order resonant converter based on sinusoidal approximation was presented and the investigation was limited to six topological "schemes" (Rudolf P. Severns, 1992). Investigation of three and four energy storage elements was reported and analysis of few topologies of the third order circuit was given (Issa Batarseh, 1994). The operation of LCL – T resonant DC – DC converter as a constant current power supply at a particular operating point was analysed (Mangesh Borage, 2005). However, most of the third order LCC topologies are not yet thoroughly analysed particularly for their suitability in automotive applications.

At present, some DC – DC converter topologies have been employed for automotive applications (Shaotang Chena, 1995, Zhenyue Hong, 2000, Itsda Boonyaroonate, 2002, Huang-Jen, 2006, Fang Z. Peng, 2003). The performance of some DC – DC converters for automotive applications has been compared (R.M.Schupbach, 2003). However, these converters were designed for an electric vehicle and hence fed the main drive motor only.

The objective of this paper is to analyse all possible third order LCC resonant converters for their suitability in automotive loads like wind shield wiper motor, head lamp, etc. Based on the desired voltage gain characteristic plot, two LCC topologies are analysed in detail. Closed form expressions for kVA/kW and energy stored in the resonant are obtained. From these expressions, the optimum value of Q which gives smallest possible resonant tank is determined.

3. Selection of topologies

3.1 Determination of order of resonant tank

Figure 1 shows a generalized representation of the resonant converter. The order of the converter is defined by the order of its commutational network. In case of one inductor and two capacitors (LCC) topology, 18 network combinations are possible (Issa Batarseh, 1994). Figure 2 shows all the possible network combinations.

The voltage gain of the system is determined from the resonant tank transfer function. All the LCC resonant topologies

shown in Figure 2 can be categorized based on the order of the resonant tank transfer function. The order is determined based on the following criteria:

(i) The order of the system is determined by the number of elements that contribute to dynamical change in energy.

(ii) Elements connected in shunt with the source and load does not contribute to the dynamical change in energy. Hence, the voltage gain (order) of such systems will always be unity.

(iii) A loop formed by two elements in which there is no possibility of dynamical change in energy between them, can be combined as a single element. When a possibility of dynamical energy change between this element and another element exists, then the order of the system will be 2.

Based on the above criteria, 18 possible LCC topologies are classified as unit gain, first, second and third order systems as shown in Table 1.

3.2 Choice of topology based on source/sink combination

The resonant tank can be excited from either a voltage (v) or current (i) source and can be used to feed either a voltage or current sink. Thus, two individual source and sink combinations are possible. These two individual combinations can be suitably arranged to give four possible source/sink combinations: v/v, v/i, i/i and i/v.

In automotive applications, the input power is fed from the battery. The converter output should exhibit good voltage regulation. Hence, the converter which is used for automotive application should be of v/v type source/sink combination.

3.3 Realisation of topologies for automotive applications

For a particular LCC topology to be realizable, the following conditions should be satisfied: (a) Loop containing capacitor(s) and voltage source or sink should not be formed. (b) Cutest containing inductor(s) and a current source or sink should not be formed.

This is because when the converter is driven or terminated by a two state square wave voltage source or sink respectively, when the voltage changes its state instantly, an infinite current spike will occur in the capacitor. Similarly, when the converter is driven or terminated by a two state current source or sink respectively, when the source or sink current changes state instantly, an infinite voltage spike will occur across the inductance.

Based on these conditions, only 8 topologies which are shown in Figure 3 are realizable for automotive application. Voltage gain for all the 8 topologies are obtained using AC analysis as explained in the next section.

4. Analysis of topologies

4.1 Introduction to AC analysis

In the ac analysis, the output rectifier and the filter are replaced by the equivalent ac resistance and the square-wave input voltage source is replaced by its fundamental sinusoidal equivalent. The power transfer from input to output is assumed to be only via the fundamental component and the contribution of all the harmonics is neglected (Robert L Steigerwarld, 1988, Robert W. Erickson, 2001).

The equivalent ac resistance for the rectifier with capacitive filter and the RMS value of the fundamental component of square-wave voltage (input to resonant tank) are given by

$$R_{ac} = \frac{\pi^2}{8} R_L \quad \text{and} \quad V_{in,rms} = \frac{2\sqrt{2}}{\pi} V_d \tag{1}$$

The resonant frequency and the normalised switching frequency is defined as

$$\omega_0 = \frac{1}{\sqrt{LC}} \quad \text{and} \quad \omega_n = \frac{\omega}{\omega_0} \tag{2}$$

The characteristic impedance and Q of the resonant network is

$$Z_n = \sqrt{\frac{L}{C}} \quad \text{and} \quad Q = \frac{\omega_0 L}{R_L} = \frac{Z_n}{R_L} \tag{3}$$

The voltage and current gain is defined as

$$M = \frac{V_0}{V_d} \quad \text{and} \quad H = \frac{I_0}{V_d / Z_n} = MQ \tag{4}$$

The voltage and current base values are given by

$$V_b = V_d \text{ and } \quad I_b = I_{in} = \frac{V_d}{Z_{in}} \tag{5}$$

Voltage gain for all candidate topologies is computed by using equations (1) – (5). From the voltage gain expression, a

characteristic plot is obtained for each topology. This is compared with the desired characteristic plot to decide upon the suitability for automotive applications. Table 2 gives the voltage gain expression for all candidate topologies.

4.2 Desired voltage gain plot

For automotive applications, fixed frequency operation over wide load ranges is preferred. This will ensure open loop mode of operation of the converter and thus results in simple configuration. In addition, it is desirable if the converter has good load regulation. This means that the output voltage or in turn the voltage gain needs to remain a constant at any one normalised frequency for various values of Q. Figure 4 shows the nature of desired voltage gain characteristics.

4.3 Topology selection based on voltage gain plot

Voltage gain plots for all the 8 topologies are plotted. Only two topologies, 1 and 2, meet the desired requirement. Figure 5 and Figure 6 shows the voltage gain plots for 1 and 2 respectively. Other topologies do not give the desired voltage gain characteristic.

For instance, in topology 6, voltage gain converges to zero at a normalised frequency of 1. This feature is not desirable as the output voltage would not be sufficient enough to meet the load requirements. For topology 8, voltage gain never remains a constant when loaded Q is varied. In order to obtain desired voltage gain, switching frequency has to be changed in accordance with load variation. Hence, it cannot be used in automotive application without using complicated closed loop control to change the frequency to obtain the required voltage gain. Similar justification can be applied to remaining topologies also. Figure 7 and Figure 8 shows the voltage gain plots for topology 6 and 8 respectively.

4.4 Stresses across resonant elements

To design a resonant converter, the voltage and current stress that the resonant elements are subjected must be known. The voltage and current stresses are derived from circuit theory basics. Table 3 and Table 4 gives expressions for normalised voltage and current stresses experienced by resonant elements L, C_1 and C_2 for topology 1 and 2 respectively. The constants A and B are defined in (6) and (7).

$$A = \left(1 + j\frac{\pi^2\omega_n x}{8Q} - \omega_n^2(1+x) - j\frac{\pi^2\omega_n^3 x}{8Q}\right)\frac{2\sqrt{2}}{\pi} \tag{6}$$

$$B = 1 - \frac{1}{\omega_n^2} + j\frac{8Q}{\pi^2\omega_n x}\left[\frac{1}{\omega_n^2} - (1+x)\right] \tag{7}$$

5. Optimization of resonant tank size

The size of the resonant tank depends on the energy stored in the tank elements and the (kVA/kW) ratio. In order to obtain smallest possible resonant tank, the energy stored in resonant tank and (kVA/kW) ratio has to be minimum at a particular value of loaded quality factor Q. The energy and (kVA/kW) ratio are computed from the stress equations. These parameters are plotted with respect to Q. From the plot, the value of Q which gives smallest possible resonant tank is determined.

From the voltage gain plot, it is observed that the voltage gain for both topologies remain constant at $\omega_n = 0.7$. Hence, the energy and (kVA/kW) ratio are computed at this operating point. The expressions for these parameters are given by (8) – (11) for topologies 1 and 2.

$$E_1 = \frac{\pi^2}{16Q}\frac{0.00375\frac{\pi^4}{Q^2} + 0.0218\frac{\pi^2}{Q^2} + 0.028}{0.00199\frac{\pi^4}{Q^2} + 0.0004} \tag{8}$$

$$E_2 = \frac{0.45Q\left(0.0092Q^4 + 4.5171Q^2 + 3.363\right)}{Q^2\left(1.063 + 0.0022Q\right)^2} \tag{9}$$

$$\left(\frac{kVA}{kW}\right)_1 = \frac{\pi^2}{8Q}\left[\frac{0.127\frac{\pi^2}{8Q} - j\left(0.03 + 0.072\left(\frac{\pi^2}{8Q}\right)^2\right)}{\left(j0.7\frac{\pi^2}{8Q}\right)^2}\right] \tag{10}$$

$$\left(\frac{kVA}{kW}\right)_2 = \left[\frac{0.166Q - j0.061\frac{8Q^2}{\pi^2} + j1.486\frac{\pi^2}{8}}{Q}\right] \tag{11}$$

Figure 9 and Figure 10 shows the energy and (kVA/kW) ratio plots respectively. It is observed that at Q = 0.545, these parameters are minimum. Thus, the size of the resonant tank is expected to be minimum when Q = 0.545. The resonant tank elements have to be designed suitably.

6. Conclusion

In this paper, selection of LCC topologies based on order of the resonant tank network is discussed in detail. The existence of various orders of resonant tank is justified. Similar arguments as mentioned in this paper can be used to select other possible multi element topologies and determine the order of their voltage gain expression also. The voltage gain requirement for automotive application is specified and the realizable topologies are further short listed and analysed. Only 1 and 2 gives load–independent voltage gain of 2 and 1.5 respectively at $\omega_n = 0.7$. Analysis of these two realizable topologies is presented in detail. Closed form expressions for various performance parameters like stresses across resonant tank elements, energy stored in the resonant tank and (kVA/kW) ratio are obtained. Based on these parameters, the size of the resonant tank is optimized. The value of Q which results in minimum tank size is computed and found to be 0.545. It is expected that this would help in designing the DC – DC converter with a smaller resonant tank and thus fulfill the high power density requirement.

Acknowledgment

The authors with to thank the management and staff of Sri Venkateswara College of Engineering, Sriperumbudur and SSN College of Engineering, Kalavakkam for providing necessary encouragement and support while carrying out this work.

References

Fang Z., Peng, Fan, Zhang, and Zhaoming, Qian. (2003). A magnetic – less DC-DC converter for dual voltage automotive systems, *IEEE Transactions on Industry Applications,* 39: 511-518.

Forsyth A.J. (1996). Review of resonant techniques in power electronic systems, *Power Engineering Journal,* 110-120.

Huang-Jen, Chiu and Li-Wei, Lin. (2006). A bidirectional DC – DC converter for fuel cell electric vehicle driving sytem, *IEEE Transactions on Power Electronics,* 21: 950-958.

Issa Batarseh. (1994). Resonant converter topologies with three and four Energy storage elements, *IEEE Transactions on Power Electronics,* 9: 64-73.

Itsda Boonyaroonate and Shinsaku Mori. (2002), A compact DC/AC inverter for automotive application, Proc. of IEEE Intl. Symposium on Circuits and Systems, 5: 829-832.

Mangesh Borage, Sunil Tiwari and Swarna Kotaiah. (2005). Analysis of LCL-T resonant converter as a constant – current power supply, *IEEE Transactions on Industrial Electronics,* 52: 1547-1554.

R.M. Schupbach and J.C. Balda. (2003). Comparing DC – DC converters for power management in hybrid electric vehicles, Proc. of IEMDC, 3: 1369-1374.

Robert L. Steigerwald. (1984). High frequency resonant transistor DC – DC converters, *IEEE Transactions on Industrial Electronics*, 31: 181-191.

Robert L. Steigerwald. (1988). A comparison of half – bridge resonant converter topologies, *IEEE Transactions on Power Electronics,* 3: 174-182.

Robert W. Erickson, Dragon Maksimovic. (2001). *Fundamentals of power electronics,* 2nd ed., Springer International, 705-726.

Rudolf P.Severns. (1992). Topologies for three element converters, *IEEE Transactions on Power Electronics,* 7: 89-98.

Shaotang Chena and Thomas A. Lipo. (1995). Soft – switched inverter for electric vehicle drives, Proc. of APEC 1995, 2: 586-591.

Zhenyue Hong, Richard Duke and Simon Round. (2000). A resonant DC link inverter for an electric vehicle, *Journal of Electrical and Electronics Engineering,* 21: 65-71.

Table 1. Topology categorisation based on order

Order	Unity gain	1st order	2nd order	3rd order
Topology Number	7, 18	8, 11, 16	3, 9, 10, 14, 15, 17	1, 2, 4, 5, 6, 12, 13

Table 2. Voltage gain expression for all topologies

Topology	Voltage gain
1	$M = \dfrac{j\dfrac{\pi^2\omega_n x}{8Q}}{1-\omega_n^2(1+x)+j\dfrac{\pi^2\omega_n x}{8Q}\left(1-\omega_n^2\right)}$
2	$M = \dfrac{1}{1-\dfrac{1}{\omega_n^2}+j\dfrac{8Q}{\pi^2\omega_n x}\left[\dfrac{1}{\omega_n^2}-(1+x)\right]}$
3	$M = \dfrac{j\dfrac{\pi^2\omega_n}{8Q}}{1+j\dfrac{\pi^2\omega_n}{8Q}(1+x)-\omega_n^2(1+x)}$
4	$M = \dfrac{j\dfrac{\pi^2\omega_n}{8Q}\left(1+x-\omega_n^2 x\right)}{1-\omega_n^2+j\dfrac{\pi^2\omega_n}{8Q}\left(1+x-\omega_n^2 x\right)}$
5	$M = \dfrac{j\dfrac{\pi^2\omega_n}{8Q}\left(1-\omega_n^2 x\right)}{1-\omega_n^2(1+x)+j\dfrac{\pi^2\omega_n}{8Q}\left(1-\omega_n^2 x\right)}$
6	$M = \dfrac{j\dfrac{\pi^2\omega_n}{8Q}\left(1-\omega_n^2 x\right)}{1-\omega_n^2 x+j\dfrac{\pi^2\omega_n}{8Q}\left(1+x-\omega_n^2 x\right)}$
7	1
8	$M = \dfrac{1}{1-j\dfrac{8Q}{\pi^2\omega_n x}}$

Table 3. Voltage and current stresses of topology 1

Element	Voltage Stress	Current Stress
L	$\frac{-\omega_n^2(1+x)-j\frac{\pi^2\omega_n^3 x}{8Q}}{A}$	$\frac{j\omega_n(1+x)-\frac{\pi^2\omega_n^2 x}{8Q}}{A}$
C_1	$\frac{1+j\frac{\pi^2\omega_n x}{8Q}}{A}$	$\frac{j\omega_n-\frac{\pi^2\omega_n^2 x}{8Q}}{A}$
C_2	$\frac{1}{A}$	$\frac{j\omega_n x}{A}$

Table 4. Voltage and current stresses of topology 2

Element	Voltage Stress	Current Stress
L	$\frac{\pi}{2\sqrt{2}}\left[\frac{1-j\frac{8Q}{\pi^2\omega_n x}}{B}\right]$	$\frac{2\sqrt{2}}{\pi}Q\left[\frac{-\frac{1}{\omega_n^2 x}-j\frac{\pi^2}{8\omega_n Q}}{B}\right]$
C_1	$\frac{\pi}{2\sqrt{2}}\left[\frac{-\frac{1}{\omega_n^2}-j\frac{8Q}{\pi^2\omega_n}\left(1+\frac{1}{\omega_n^2 x}\right)}{B}\right]$	$\frac{2\sqrt{2}}{\pi}Q\left[\frac{1-\frac{1}{\omega_n^2 x}-j\frac{\pi^2}{8\omega_n Q}}{B}\right]$
C_2	$\frac{2\sqrt{2}Q}{\pi\omega_n x}\left[\frac{1}{B}\right]$	$\frac{2\sqrt{2}}{\pi}\frac{Q}{B}$

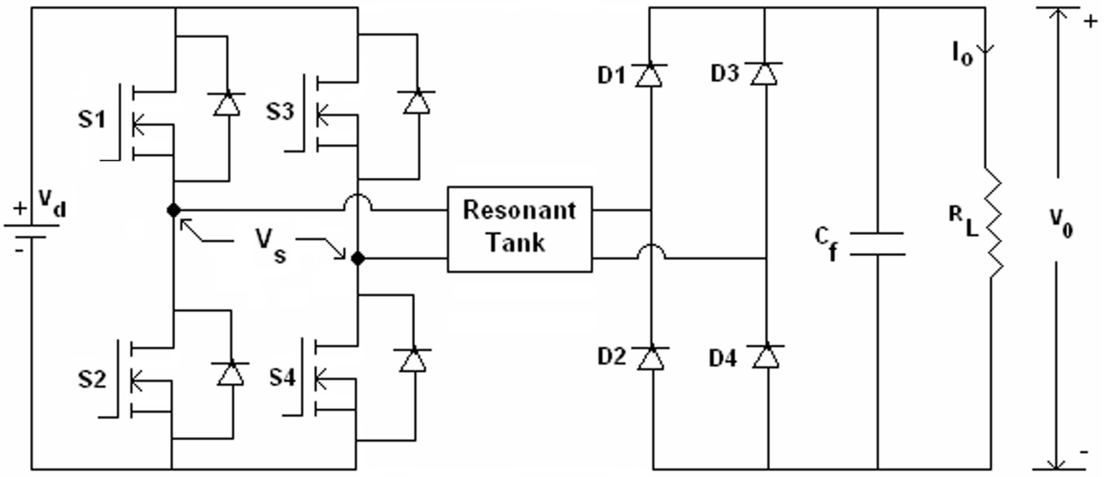

Figure 1. Generalised representation of a resonant converter

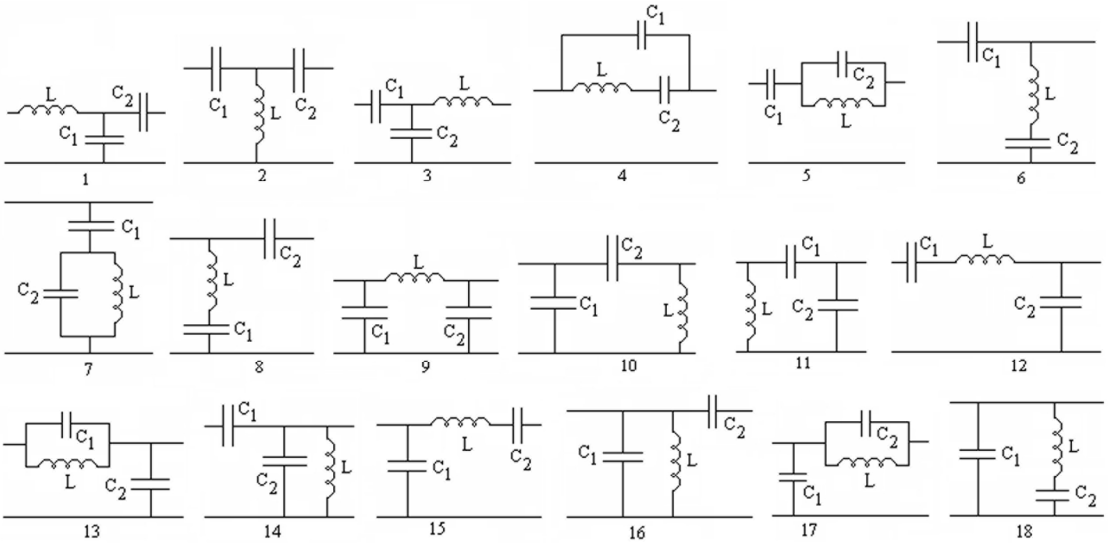

Figure 2. All possible LCC topologies

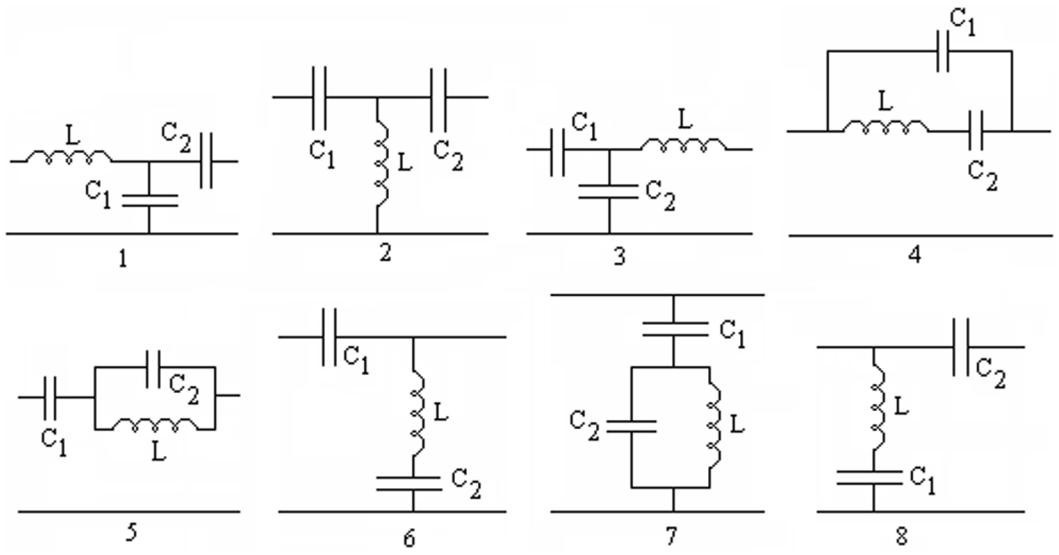

Figure 3. Realisable topologies

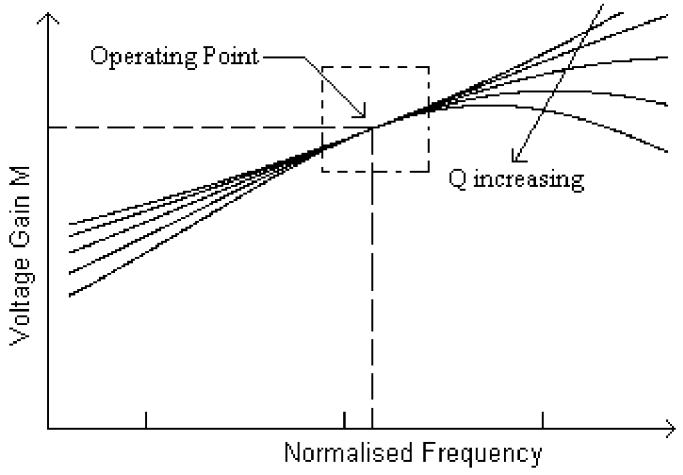

Figure 4. Desired voltage gain plot

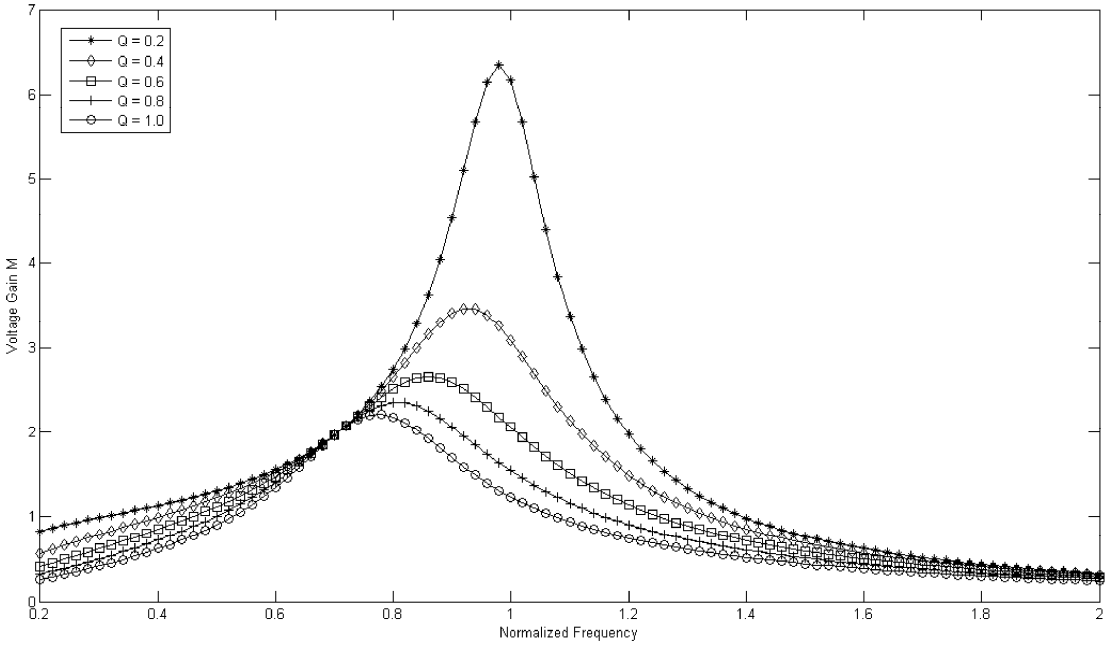

Figure 5. Voltage gain plot of topology 1

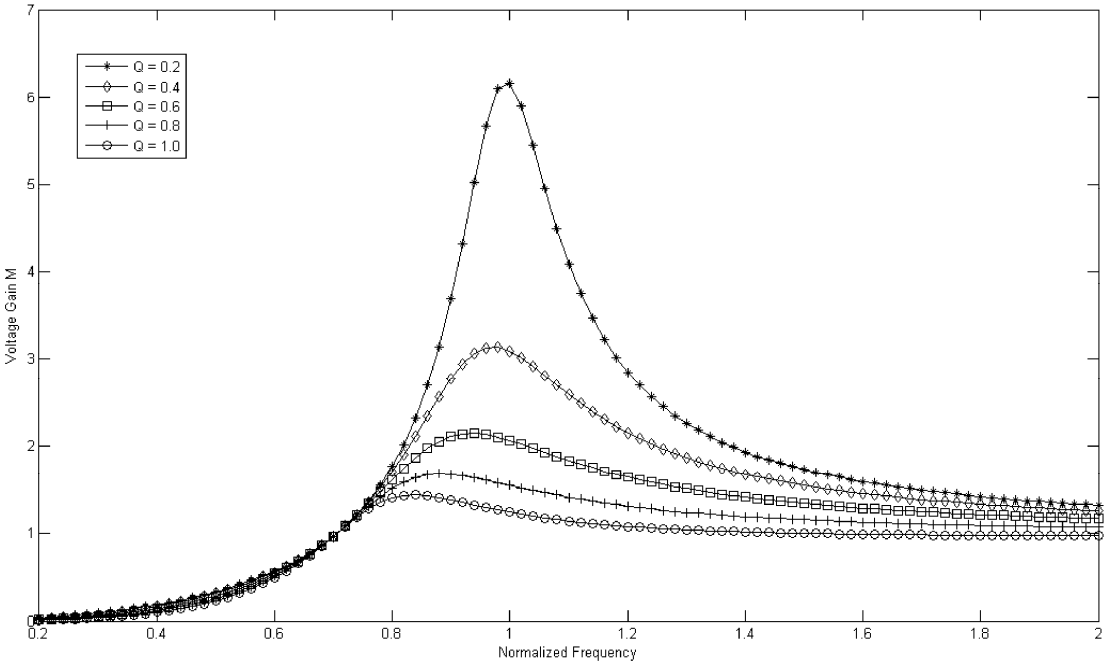

Figure 6. Voltage gain plot of topology 2

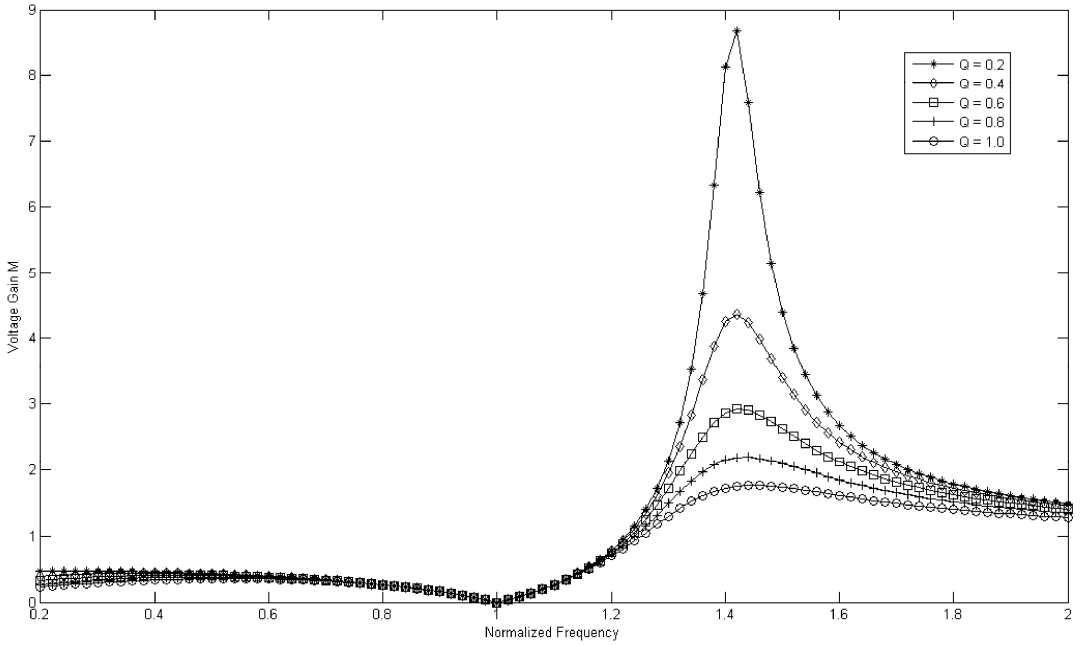

Figure 7. Voltage gain plot of topology 6

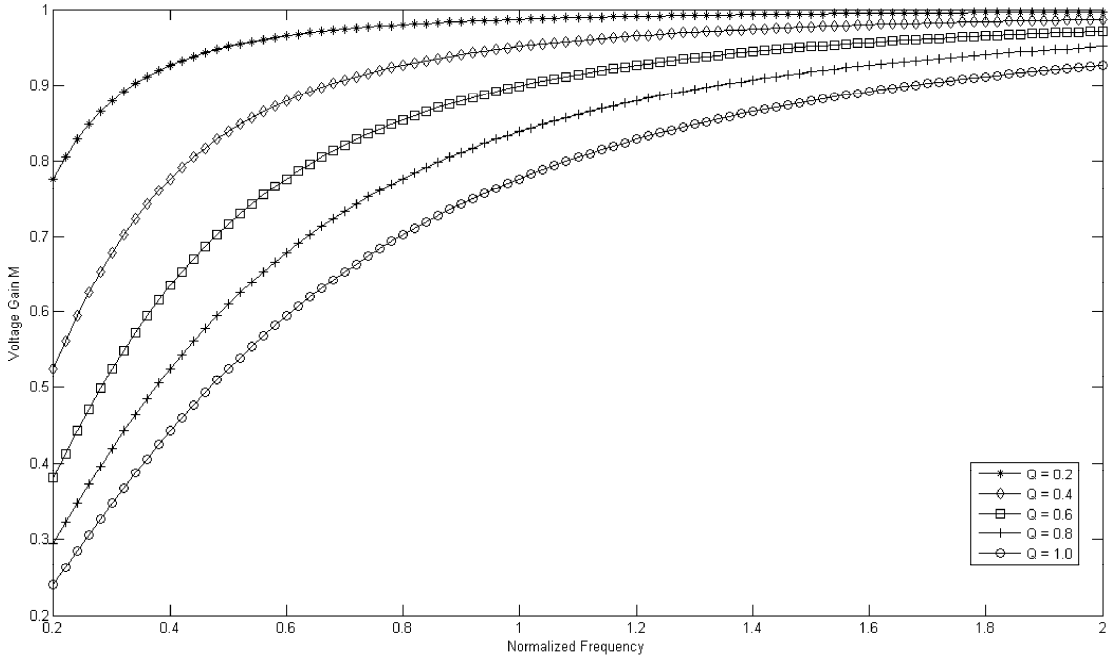

Figure 8. Voltage gain plot of topology 8

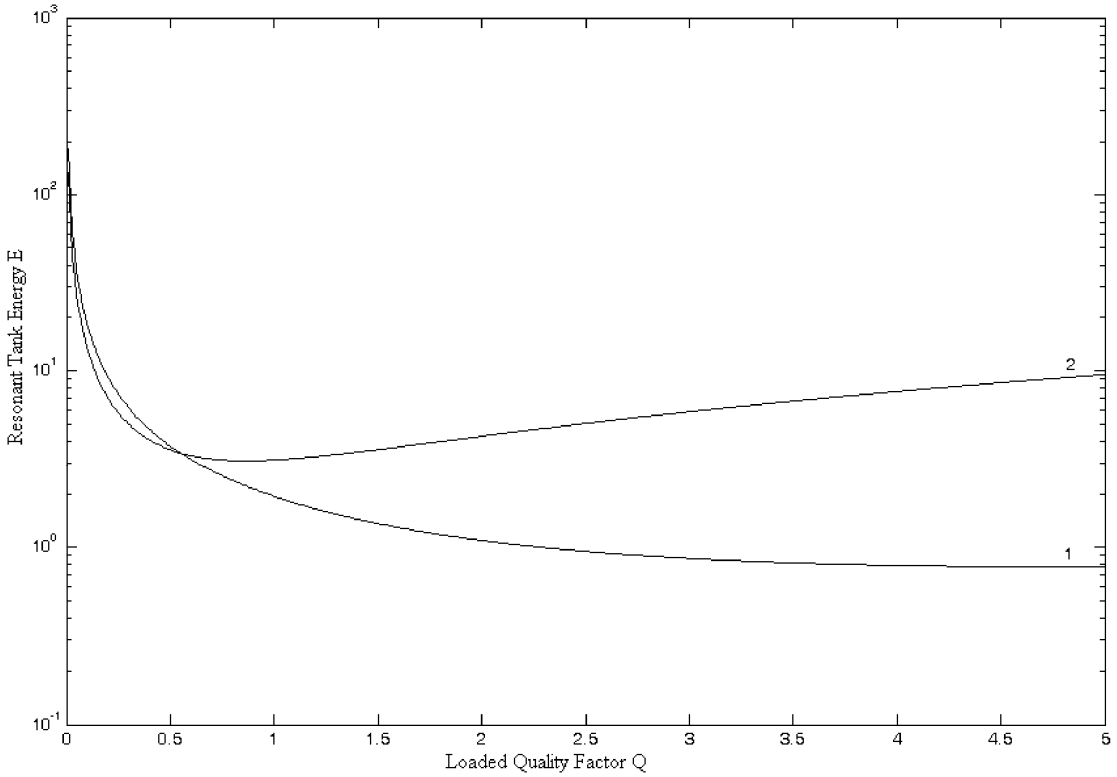

Figure 9. Energy vs Q for topology 1 and 2

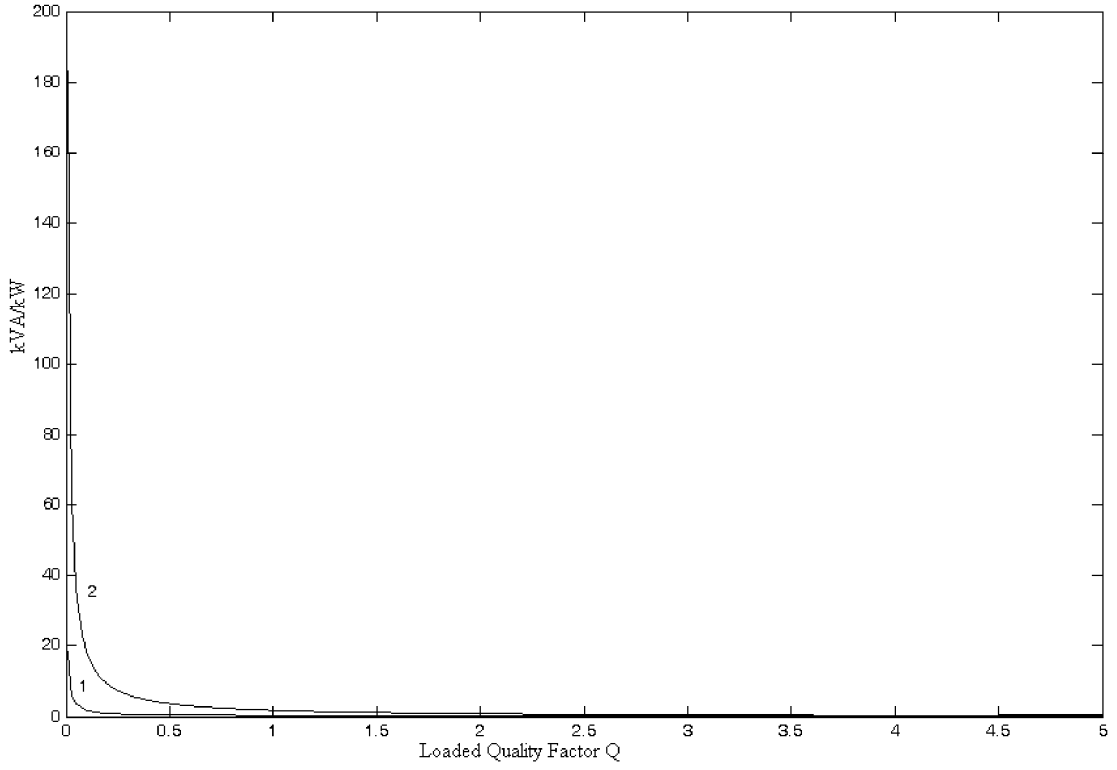

Figure 10. kVA/kW ratio plot for topology 1 and 2

Modern Applied Science

www.ccsenet.org/journal.html

Vol. 3, No. 7

July 2009

Simulation of Gravity Feed Fuel for Aeroplane

Yaguo Lu, Zhenxia Liu & Shengqin Huang

School of Power and Energy, Northwestern Polytechnical University, Xi'an 710072, China

Tao Xu

Military Representatives office of NDMMP, Xi'an 710025, China

Abstract

Gravity feed is one fuel supply way for aeroplane and the simulation of it is very important. The traditional method to calculate the gravity feed is to assume that only one tank in fuel system supplies the needed fuel to the engine, and then calculated for the single branch. Actually, all fuel tanks compete for supplying fuel and the key problem for gravity feed calculation is to simulate the multiple-branch and transient process. The present paper gives the mathematical model for fuel flow pipe, pump, check valve and the simulation model for fuel tank at first, and then presented a new calculation model for gravity feed fuel of aeroplane fuel system based on the flow network theory and time difference method. The model takes into consideration all fuel tanks and can solve the multiple-branch and transient process of gravity feed. Finally, the thesis gives a numerical example for a certain type of aircraft, achieved the variations of fuel level and flow mass per second of each fuel tanks, the variations of the fuel pressure at the engine inlet, and predicted the maximum time that the aeroplane could fly safely under gravity feed. The numerical example indicts that the method proposed here is intrinsically superior to the traditional methods and is closer to understanding the real seriousness of the fuel supply situation.

Keywords: Gravity feed fuel, Element model, Network theory, Multiple-branch, Transient process

Nomenclature

Q volumetric flow rate

P pressure from a datum at certain points

P_s air pressure in fuel tank

γ specific gravity of the fluid

g acceleration of gravity

ρ density of fuel

Z elevation from a datum at certain points

L pipe diameter

D pipe length

f friction factor for pipes

K dimensionless experimental coefficient accounting for head losses

h height fuel level from the bottom of tanks

$A(h)$ tank cross-sectional area at h

Re Reynolds number

μ dynamic viscosity of fluid

$P_{in,out}$ pressure at the inlet and outlet of elements

V velocity of fluid

Δ pipe roughness

ξ resistance characteristic constant of pump

a characteristic constant of check value

P_c crack pressure of check value

1. Introduction

The function of fuel system of aircraft is to store fuel and supply it to the engine under certain flow rate and pressure continuously (Hampus Gavel, Petter Krus, Johan Andersson.)(Hampus Gavel, Petter Krus, Johan Andersson, et al., 2005). Generally, it has two different ways for fuel transfer, the simplest one is by gravity(Hampus Gavel, Petter Krus, Johan Andersson.)(Hampus Gavel, Petter Krus, Johan Andersson, et al., 2005), and another is by pumps. But when flying, it exist the possibility that all the pumps stop working under some situation, such as electrical and mechanical accident. So the simplest method changes to the vital one and the simulation of gravity feed become significant.

Fuel transfer system is a system, which comprises many fuel tanks and much complex pipelines. The traditional method to calculate the gravity feed is to assume that only one tank in fuel system supplies the needed fuel to the engine, and then calculated for the single branch. Actually, gravity feed fuel is a transient process and all fuel tanks compete for supplying fuel according to their ability of fuel supply. The fuel level in fuel tanks decreases when fuel transferring and the ability of one fuel tank for fuel supply decreases also. With these changes, there might have several fuel tanks supplies fuel simultaneously. Thus the fuel supply network is a complex system in which may have many branches. The key problem to calculate gravity feed is the simulation of multiple-branch and transient process. The present paper established a new calculation method for gravity feed of aeroplane fuel system. This model can solve the multiple-branch and transient process simulation of gravity feed fuel and it is intrinsically superior to the traditional methods.

2. Gravity feed analysis

The fuel transfer system of a certain aircraft is composed of fuel tanks, fuel pumps, pipes, check valves and other common flow resistance components. When fuel transfers under gravity, the fuel flows spontaneously through the fuel pump and the check valve. Here, the fuel pump is stop operating, which is considered as a resistance element specially. The function of the check valve is to prevent the fuel backward flow between fuel tanks.

Fuel tank supplies fuel according to its ability of gravity feed. There might have some factors effect the ability, which include the air pressure in tanks, P_s, the gravitational potential energy of fuel and the resistance of fuel offer pipeline, h_w. The pressure in tanks is related to vent system of aircraft and approximately equal in different tanks. The gravitational potential energy of fuel changes with the fuel level, h, and the elevation from the bottom of tank to engine inlet, Z. Figure 1 is a schematic diagram of gravity feed fuel.

3. Theory

3.1 Flow network theory

In order to decide the flow rate and pressure drop through the flow network, first, the theory of mass conservation may be imposed at each junction of the flow network. Therefore, the algebraic summation of all flow entering a junction is zero (Wu Dingyi, 1997)(S. M.Chun, 2003)(Cao Lianhua, Zhuang Damin, Ning Chunli, et al, 2002). For the incompressible flow, at a node, the continuity equation is

$$\sum_{i=1}^{n} Q_i = 0 \tag{1}$$

Second, the continuity of energy per unit mass may be applied along the same pipeline. The energy potential between two nodes in certain pipe is equal. For the incompressible flow on the same pipeline, the energy balance equation (Victor L. Streeter, E. Benjamin Wylie, Keith W. Bedford, 1998). is

$$\frac{P_a}{\gamma} + \frac{V_a^2}{2g} + Z_a = \frac{P_b}{\gamma} + \frac{V_b^2}{2g} + Z_b + h_w \tag{2}$$

Where, P_a, P_b, and V_a, V_b and Z_a, Z_b represent pressure, velocity and elevation from a datum at certain points, a and b. h_w is frictional head loss. γ is specific gravity of the fluid, g is acceleration of gravity.

3.2 Element Model

(1) Pipe flow

For the incompressible flow, the pressure drop through a pipe is induced by the energy Equation (2).

$$P_a - P_b = \rho f(Q,D)\frac{8Q^2}{\pi^2 D^4}\left\{\frac{L}{D}+\frac{K}{f(Q,D)}\right\}+\gamma(Z_b - Z_a) \tag{3}$$

Where, K is the dimensionless experimental coefficient accounting for head losses in bend, elbows etc. For the general elbow, K = 0.5, and the T-type joint, K = 1.0(Victor L. Streeter, E. Benjamin Wylie, Keith W. Bedford, 1998). ρ is the density of fluid. Q is volumetric flow rate. f is a friction factor for pipes of circular cross section and can be decided below.

1) laminar flow, $\mathrm{Re} \le 2000$

$$f(Q,D) = \frac{64}{\mathrm{Re}} \tag{4}$$

2) turbulent flow, Re>2000

$$\frac{1}{\sqrt{f(Q,D)}} = -2.0\log\left(\frac{\Delta}{3.7D}+\frac{2.51}{\mathrm{Re}\sqrt{f(Q,D)}}\right) \tag{5}$$

Where, Δ is pipe roughness, Re can be expressed by $4\rho Q/\pi\mu D$. μ is dynamic viscosity of fuel.

(2) Fuel Pump flow

The fuel pump is stop operating when fuel transferring under gravity, and it could be considered as a local resistance element. The relationship between flow rate and pressure difference can be expressed by Equation (6).

$$P_{in} - P_{out} = \xi Q^2 \tag{6}$$

Where, ξ is constant that decide by resistance curve of fuel pump.

(3) Check valve flow

The function of the check valves is to prevent the fuel backward flow between two fuel tanks. The valve remains completely closed until the positive pressure differential exceeds the crack pressure. The relationship between flow rate and pressure difference can be expressed by Equation (7).

$$P_{in} - P_{out} = aQ^2 + P_c \tag{7}$$

Where, a is a constant that decide by characteristic curve which obtained by experimentation, and P_c is the crack pressure.

(4) Fuel tank model

The illustration of model of fuel tank is show in Figure 2. Where, Z is the tank's parameter of location, P_s is air pressure in fuel tank, and h is the fuel level. Because of Z is constant when the fuel system of aircraft has been design finished, h is the only variable that effects the gravitational potential energy of fuel and further effects the ability of gravity feed of fuel tank. We presented the curve for fuel tank, which show the relationship between cross-section area, $A(h)$ and fuel level, h. These curves could be used to simulate the changes of fuel level in gravity feed process which detailed in the next part. The curves of the five fuel tank for one aeroplane are illustrated in Figure 3~7.

3.3 Transient Process Simulation

This study used the time difference method to simulate the transient process. Based on this method, we divided the whole process of gravity feed into many small time sections, Δt_1, Δt_2, $\ldots \Delta t_n$. In one time interval Δt_i, it assumed that the whole flow process is steady-state, and the fuel flow rate of each fuel tank is considered as a constant.

On the basis of the difference method, the transient process is simulated below:

1) Define the fuel level of each fuel tank, h_i^t, at the beginning time, $t=t_0$, of gravity feed.
2) Define the boundary condition.
3) Network calculation

Calculation for the whole fuel transfer system using flow network theory, obtain the flow rate of each fuel tank, Q_i^t, and the pressure distribution in flow system.

4) Using the fuel tank model to calculate the new fuel level of each fuel tank, $h_i^{t+\Delta t}$.

$$\begin{cases} \Delta h_i^t = \dfrac{Q_i^t \cdot \Delta t}{A(h_i^t)} \\ h_i^{t+\Delta t} = h_i^t - \Delta h_i^t \end{cases} \tag{8}$$

Define the new fuel level of each fuel tank when $t = t + \Delta t$, $h_i^{t+\Delta t}$.

Repeat step 3) to step 5), the whole transient process of gravity feed could be simulated.

3.4 Numerical

Based on the established method, we calculated the gravity feed for one certain type of aircraft. The aircraft has two (right and left) fuel transfer system, the right system showed in figure 8 transferring fuel for the right engine and the left providing fuel for the left engine, the two system also can supply fuel to one engine simultaneity in addition .

As show in figure 8, the right fuel transfer system has five fuel tanks, and the tank 4 and tank 5 assembled in the wing, the check values which installed in the fuel transfer pipes to prevent the fuel backward flow between fuel tanks.

The right system gravity feed has been simulated in this section with the flight condition: flight height is 7km and the engine is 0.5 rated condition. The calculation boundary condition for network is the air pressure in each fuel tanks (approximately equal the atmospheric pressure at 7km) and the fuel flow rate to the engine which is 2800kg/h ($0.000997 m^3/s$).

We also should give the fuel level in each fuel tanks when calculation. All the fuel tank is assumed filled at the beginning of the calculation and the fuel level for the five fuel tanks could be obtained from the tank relation curves showed in Figure 3~7.

In the simulation, we obtained the variation of fuel level in each fuel tank, the fuel flow rate for each fuel tank and the variation of pressure at the engine inlet. The calculate results are showed in figure 9~11.

4. Analysis

Figure 9 and Figure 10 give respectively the variations of fuel level and flow rate per second of each five fuel tanks within a period of 16000 seconds. Figure 11 shows the changes of fuel pressure in engine inlet.

As show in Figure 9 and Figure 10, the tank 1, tank 3 and tank 4 all supplies fuel to the engine at different flow rate at the beginning of gravity feed. The flow rates of the three tanks are changes with time, and the flow rate of tank 4 exceeds the flow rate of tank 1 at approximate 9000s. Specially, the tank 2 and tank 5 also begin to offer fuel one after the other with their flow rate increasing and fuel level descending. This all characteristics indict that all fuel tanks compete for supplying fuel according to its' ability of gravity feed respectively.

As show in Figure 11, the fuel pressure in engine inlet decreases gradually. Once the fuel pressure less than the minimum pressure limit in engine inlet, the gravity feed fuel would not ensure the aircraft fly safely under one flight condition. From Figure 11 we could also approximately predict the maximum flight time under gravity feed.

5. Conclusion

The thesis established a new calculation model for gravity feed of aeropalne fuel transfer system based on flow network theory and time difference method. This model can solve the multiple-branch and transient process of gravity feed. The model of non-working pump, check valve and fuel tank are also presented.

The results of the simulation of fuel transfer system for one certain type of aircraft show that all fuel tanks compete for fuel supply according to their abilities of gravity feed respectively, but not only one tank offers fuel alone.

Acknowledgements

The authors would like to acknowledge Prof. Lian Xiaochun and Mr. Xiao Hong for their suggestion and critical review throughout the period of the research.

References

Cao, Lianhua, Zhuang, Damin, Ning, Chunli, et al.: (2002). Numerical Calculation of Fluid Network System of Fighter. *Aircraft Design*. 2002,No.4, pp 37-41.

Hampus Gavel, Petter Krus, Johan Andersson, et al.: (2005). Probabilistic Analysis in the Conceptual Phase of an Aircraft Fuel System, 46th AIAA/ASME/ASCE/AHS/ASC Structures, Structural Dynamics & Materials Confer18-21 April 2005, Austin, Texas.

Hampus Gavel, Petter Krus, Johan Andersson.: Quantification of The Elements in The Relationship Matrix - A Conceptual Study of Aircraft Fuel System. in Proceedings of 42nd AIAA Aerospace Sciences Meeting and Exhibit, Reno, Nevada.

S.M.Chun. (2003). Network Analysis of An Engine Lubrication System. *Tribology International*. 2003, Vol.36, No.8, pp.609-617.

Victor L. Streeter, E. Benjamin Wylie, Keith W. Bedford. (1998). Fluid Mechanic. McGraw-Hill Companies, Inc. 1998.

Wu Dingyi. (1997). Network Algorithm of Internal Flow System. *Journal of Aerospace Power*. 1997, Vol.17, No.6, pp.653-657.

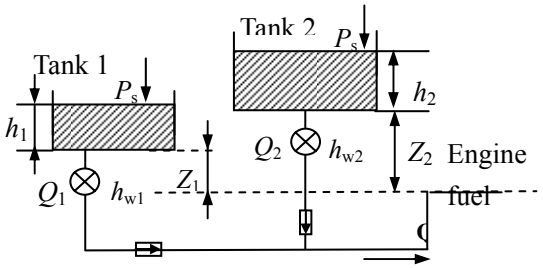

Figure 1. The schematic diagram of gravity feed fuel

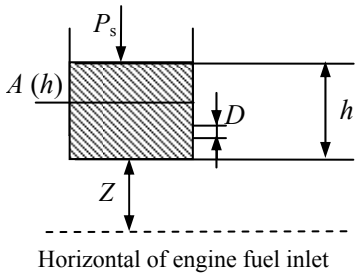

Figure 2. Model of fuel tank

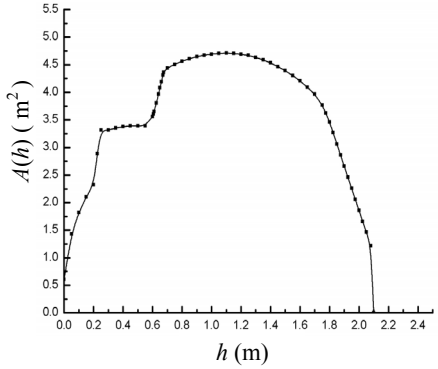

Figure 3. The relation curve for fuel tank 1

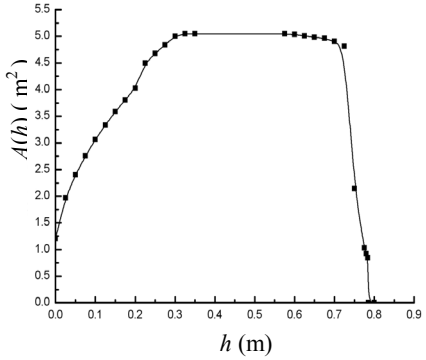

Figure 4. The relation curve for fuel tank 2

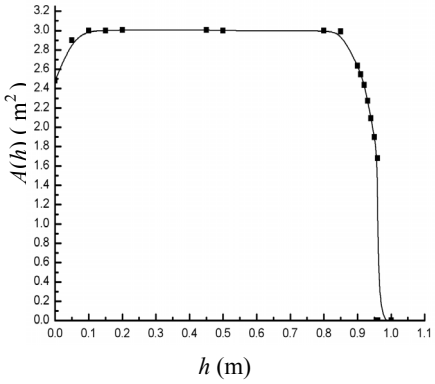

Figure 5. The relation curve for fuel tank 3

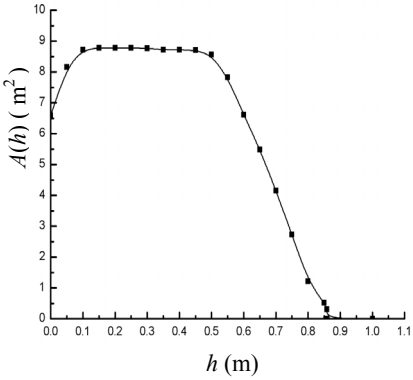

Figure 6. The relation curve for fuel tank 4

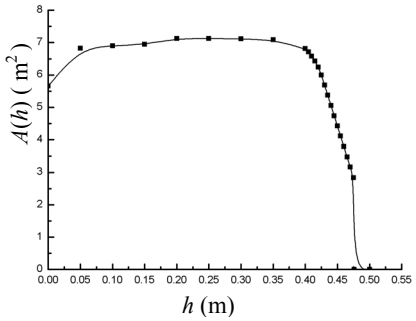

Figure 7. The relation curve for fuel tank 5

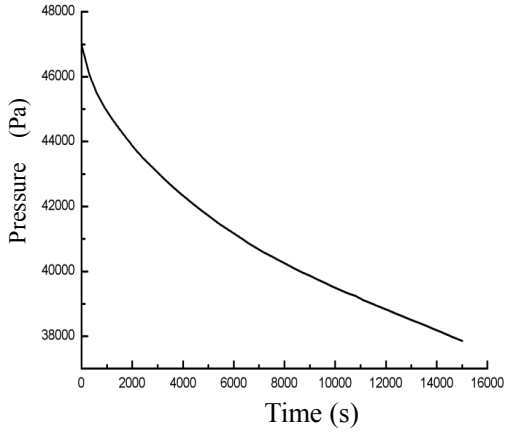

Figure 11. Changes of the fuel pressure at engine inlet

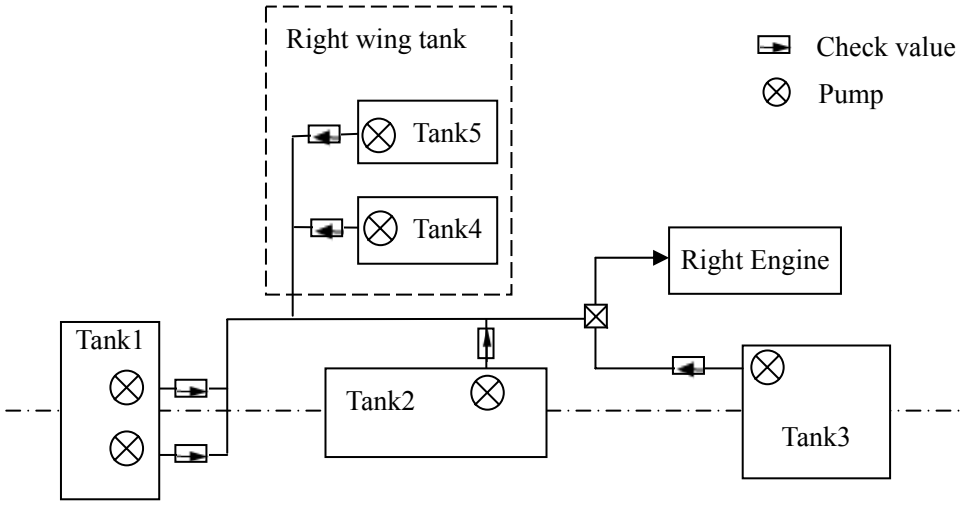

Figure 8. Right fuel transfer system for one aircraft

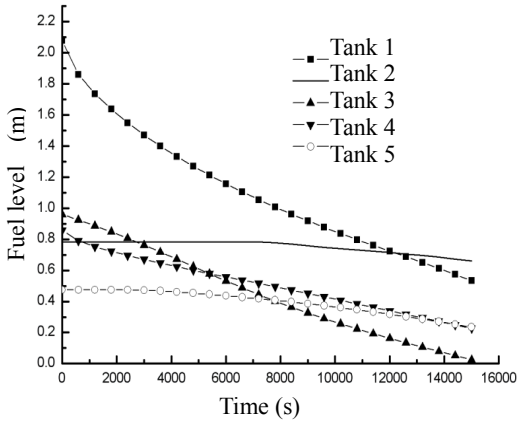

Figure 9. Variation of fuel level in each fuel tank

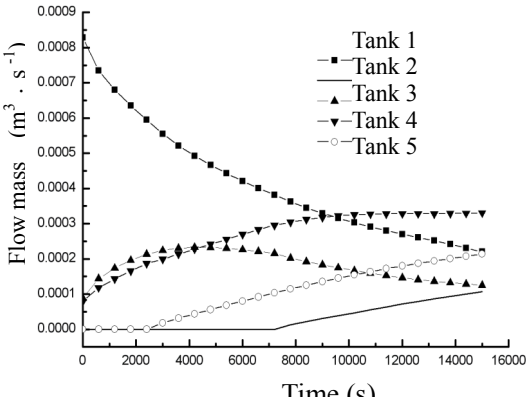

Figure 10. Variation of flow mass of each fuel tank

Modern Applied Science

www.ccsenet.org/journal.html

Vol. 3, No. 7

July 2009

Kinetic Study on Decolorization of the Dye Acid Orange Using the Fungus *Phanerochate Chrysosporium*

Balu

Department of Chemical Engineering, Anna University, Chennai, India

K.V.Radha (Corresponding author)

Department of Chemical Engineering, Anna University, Chennai, India

E-mail: radhavel@yahoo.com

Abstract

A dye decolorizing fungal strain, *Phanerochaete chrysosporium* MTC 787 was used in batch experiments for decolorization of the dye, Acid orange10. Effects of initial substrate (dye) and fungal concentrations on the rate and extent of dye decolorization were investigated. The initial pH and oxidation–reduction potential (ORP) was kept at 4.5 and −250 mV, respectively. The rate and extent of dye decolorization increased with increasing dye concentration up to 100 g l^{-1} and then decreased for larger dye concentrations. The rate of enzyme utilization and dye decolorization also increased linearly with increasing initial biomass concentration. A kinetic model describing the rate of enzyme utilization and substrate inhibition as function of the initial substrate and flow rate was developed. The kinetic constants were determined using the experimental data. The initial biomass should be above 3.2 x 10^5cell/ml to obtain high rates and decolorization percentage and to avoid substrate inhibition.

Keywords: *Phanerochaete chrysosporium*, Kinetics, Dye, Model, pH, Fungus, Enzyme, Potential

1. Introduction

Synthetic organic colorants are used for several purposes in the textile, cosmetic, paper making, food and pharmaceutical industries. Textile dyeing processes exhibit highly colored wastewater in large amounts, which is let into the natural water streams. Around 10,000 different types of dyes and pigments are produced and an average of 10-15% of these dyes are let into the wastewater stream (Pearce 2003).Since these dyes exhibit colours in the land, lots of work are carried in the field of decolorizing the dyes before it is let into the land or water resources (O'Neill 1999). Several work involving chemical, physico-chemical, membrane treatment and biological treatment are on its way to purify the wastewater (Francis perineau 1982). In the biological treatment processes, organisms such as *Phanerochaete chrysosporium*, *Coriolus versicolor*, *Pseudomonas* species, *Aspergillus* Sp., are involved in decolorization (Knapp 1995). White-rot fungi are well known for their outstanding ability to produce extra cellular oxidative enzymes, which initiate lignin degradation. The white-rot fungi best involved for treating dyes is *P. chrysosporium* and we have chosen the same for our reactor studies as the enzymes produced by the fungus which causes decolorization are highly non-specific and degrade a variety of dyes (Radha 2005).

While much research has been carried out on the uptake of dye and other pollutants little attention has been given to study the kinetics. Decolorization of dyes using microorganism is affected by several factors (Chulhwan 2006) which include the specific surface properties of the microorganism and the physicochemical parameters of the dye solution such as pH, initial dye concentration and initial biomass concentration (Loukidou 2004). Many other parameters also affect the capacity of microorganism to bind on the immobilizing agents (Wu 2006).The combined effects of two or more component of the microorganism depend on the nature of dye. They compete for the binding sites and in combination of one or more dyes, competence is for the order of the dye addition and it also includes the residence time in the reactor which may initiate the competence level (Aksu 2003).In order for the better utilization of the enzyme and the whole cells they are immobilized onto a solid support which leads to advantageous reactor operation system. The equilibrium established between the dye component and the immobilizing agent and the non-reacted component in solution can be represented through kinetics. The major objective of this study is to investigate the kinetics of dye

solution for a large range of dye concentration and biomass concentrations and to determine the kinetic constants using the experimental data.

2. Materials and Methods

2.1 Experimental set-up

Batch experiments were performed by using sterile Erlenmeyer flasks and a gyratory incubator shaker at 37 °C and 150 rpm. In variable substrate (dye) concentration experiments, the Erlenmeyer flasks (500 ml) were charged with 180 ml of deionized water containing desired concentrations of dye between 10 and 100 g l^{-1} and 200 mg l^{-1}. Na - thioglycolate was the reducing agent which is used to adjust the oxidation–reduction potential (ORP) to −250 mV. The Erlenmeyer flasks were prepared in duplicates, sterilized at 121 °C for 20 min and inoculated with 20 beads calcium alginate immobilized *P.chrysosporium*. Variable biomass concentration experiments were performed by inoculating the experimental flasks with different amounts of inoculum (10–100 beads) and dye solution (10–100 ml of constant concentration) to obtain a total volume of 200 ml in every flask. The initial pH of the media was adjusted to 4.5. Inoculated flasks were placed on a gyratory shaker at 37 ±2 °C and 150 rpm. Samples were withdrawn aseptically from the experimental flasks periodically for analysis of enzyme activity, biomass and percentage decolorization. A control flask free of fungal immobilized cells containing 100 g l^{-1} dye and 100 mg l^{-1} Na-thioglycolate was used to determine decolorization of any dye in the absence of fungal cells. Duplicate flasks were used to test the reproducibility of the data.

2.2 Microorganism

P.chrysosporium MTCC-787 obtained from Microbial Tissue culture collection centre, Chandigarh, India in lyophilized form was used in all experiments. The fungal strain was cultivated in laboratory using an incubator shaker under sterile conditions at pH 4.5. Pure cultures grown under respective conditions were used for inoculation of experimental flasks.

2.3 Medium composition

Medium used for cultivation of inoculum culture consisted of glucose (10 g l^{-1}), Malt extract (0.5 g l^{-1}), NH_4Cl (0.054g l^{-1}), KH_2PO_4 (0.136 g l^{-1}), $MgSO_4 \cdot 7H_2O$ (0.044g l^{-1}), $MgCl_2.6H_2O$ (0.0775 g l^{-1}), $CaCl_2.2H_2O$ (0.1g l^{-1}), and 200 mg l^{-1} Na-thioglycolate as the reducing agent at pH 4.5. The initial oxidation–reduction potential (ORP) of the media was nearly about −250 mV indicating the anaerobic conditions. The fungal culture grown on a shaker in the aforementioned media at 37 °C and 150 rpm was used as inoculate for the experimental flasks. The experimental flasks contained desired concentrations of dye and 100 mg l^{-1} Na-thioglycolate (ORP = − 250 mV) in deionized water at pH 4.5. Dye concentration was varied between 10 and 100 g l^{-1} in variable substrate experiments. In the variable inoculum size experiments the initial biomass concentration was varied between 1.2 x 10^5cells/ml and 4.5 x 10^5cells/ml while the dye concentration was constant at 100 g l^{-1}.The dye Acid orange 10 was obtained from Department of Textile Technology, Anna University, Chennai, India and was kept in sterile state before use.

2.4 Immobilization

The fungus *P.chrysosporium* was inoculated on malt agar and incubated at 35^{o}C, until extensive spore growth occurred. The samples were removed from the flasks periodically and centrifuged at 8000 rpm to remove solids from the liquid media. Analysis was made for the enzyme activity which included lignin peroxidase and manganese peroxidase. Suspensions of 2ml were added to 100 ml of 2% sodium alginate. The mixture was gently stirred at room temperature to produce a uniform suspension and then dropped into 100ml of 20% Calcium chloride solution. The beads so obtained were stored in calcium chloride solution at 4^{o}C for 2 h to complete gel formation (Sheldon 2005). The insoluble and stable immobilized *P.chrysosporium* alginate beads thus obtained were further used for the decolorization studies. Plain beads were prepared without the spore suspension and these were used as the reference beads.

2.5 Analytical methods

Samples were collected at regular intervals and dye concentrations were measured using a spectrophotometer [UV/VIS Shimadzu spectrophotometer (model U 2000)].

Enzyme activities were determined spectrophotometrically using the different enzyme assays individually for lignin peroxidase, manganese peroxidase.

Lignin Peroxidase activity was determined spectrophotometrically (Tien and Kirk 1983) with Veratryl alcohol as substrate. One unit was defined as the amount of enzyme that oxidized 1µmol of Veratryl alcohol in 1 minute at 310nm and the activities are reported as U/ litre.

Manganese Peroxidase activity was assayed at 610nm using Dimethoxyphenol as the substrate as suggested by Field et al., 1993. One unit was defined as the amount of enzyme that oxidized 1µmol of Dimethoxyphenol per minute and the activities are reported as U/ litre.

The samples were analyzed in triplicates and the results were reproducible within 3% deviation. Oxidation reduction potentials (ORP) and pH were measured using a pH meter with either an ORP or a pH probe.

3. Results and discussion

3.1 Effect of initial substrate concentration

The Acid orange 10 concentrations were varied between 10 and 100 g l^{-1} in this set of batch experiments while the initial biomass concentration was constant and kept as 25 beads. Variations of dye concentration and enzyme activity with time are depicted in Fig 2a and b, respectively for different initial dye concentrations. Percentage decolorization was almost completed within 72 h when dye concentration was less than 10 g l^{-1}. Complete enzyme utilization took place when dye concentration was larger than 100 g l^{-1} (Fig 2a) due to substrate inhibition at high dye concentrations. Percentage decolorization also reached the maximum level after 72 h of incubation when dye concentration was less than 10 g l^{-1} while complete dye decolorization took longer for higher dye concentrations. An incubation time of 72 h was considered in all further calculations. The pH values dropped from an initial level of 4.5 to 3.0 at the end of 72 h when dye was less than 100 g l^{-1}. The final pH for dye concentrations above 100 g l^{-1} was between 4.7 and 5.2 at the end of 72 h. The ORP decreased from −150 mV to nearly −350 mV in all experiments, except the one with 10 g l^{-1} dye for which the final ORP was −250 mV at the end of 72 h. There was no decolorization taking place in the control flasks. The results of the duplicate experiments were almost the same within 2% deviation indicating the reproducibility of experimental data. Variations of specific rates of enzyme utilization and decolorization with dye concentration are shown in Fig 3a and b. Specific rates (R_{SX}= (So-S)/ (t.X), g enzyme/g biomass hour) were calculated for the first 72 h. The specific rate of enzyme utilization increased with dye concentrations up to 100 g l^{-1} dye indicating substrate limitations at low dye concentrations. The rate decreased with increasing dye concentrations above 100 g l^{-1} due to substrate inhibition at high dye concentrations (Fig.3a). Similar trends were also observed in the specific rate of dye decolorization (R_{PX}= (P-Po)/ (t.X), g dye/g biomass.h). Dye decolorization rate for the first 72 h period increased at low dye concentrations below 100 g l^{-1} due to substrate limitations, but steadily decreased with increasing dye concentrations for dye larger than 100 g l^{-1}due to substrate inhibition (Fig 3 b). Dye concentration should not exceed 100 g l^{-1} for higher percentage decolorization.

3.2 Effect of initial fungal concentration

Biomass (fungus) concentration is another important parameter affecting the rate and extent of dye decolorization. A series of batch shake flask experiments were performed with varying initial biomass concentrations between 25 and 200 beads containing (approximately 3.2 x 10^5 cells/ml to 8.9 x 10^6 cells/ml) with a constant dye concentration of 100 g l^{-1}. Fig 4 a and b depict variations of enzyme activity and dye concentrations with time for different initial biomass concentrations. Enzyme utilization was completed within 24 and 30 h when biomass concentrations were above 100 and 150 beads respectively. However, enzyme utilization was rather slow for biomass concentrations below 150 beads since the rate is directly proportional with the biomass concentration. Enzyme utilization was completed after 72 h when biomass concentration was less. (Fig.4a). Decolorization percentage also reached the maximum level after 72 h of incubation when biomass concentration was above 50 beads. Nearly 120 h were required for maximum decolorization when biomass concentrations were lower than 50 beads as shown in Fig.4b. pH values in experimental flasks decreased from an initial pH of 4.5 to pH 3.6–3.8 depending on the initial biomass concentrations. Therefore, pH variations were not significant to require pH control. The final oxidation reduction potentials (ORP) at the end of 72 h were between −250 and −275 mV with an initial ORP of −250 mV for all experimental flasks. Biomass concentrations increased with time to give a yield coefficient of 1.1 g X g S^{-1} on the average. There was no enzyme utilization and decolorization in the control flask free of biomass. The results of the duplicate experiments were almost the same within 2% deviation.

Fig 5 a and b depict variations of volumetric rates of enzyme utilization and decolorization with the initial fungus concentration. The time periods considered for calculating the rates were until complete utilization of enzyme (24, 31 and 48 h for different biomass concentrations and 120h for decolorization), since decolorization continued a little while after complete enzyme utilization. The volumetric rate of enzyme utilization increased with biomass concentration almost linearly yielding nearly 200 mg l^{-1} h^{-1} enzyme utilization rate at 25 beads biomass concentration (Fig.5a). Percentage decolorization rate also increased with biomass concentration as shown in Fig.5 b. The maximum dye decolorization rate of 0.105 ml l^{-1} h^{-1} was obtained with 100 beads containing 5.2 x 10^5 cells/ml of initial biomass concentration.

3.3 Kinetic modeling and estimation of the kinetic constants

The following kinetic model was used to describe the initial rate of substrate utilization [12].

$$v = \frac{kX_o S_o}{k_s + S_o}\left(\frac{k_{SI}}{k_{SI} + S_o}\right) \quad (1)$$

Where V is the initial rate of dye utilization (g S l^{-1} h^{-1}); Xo and So are the initial biomass and the substrate (dye) concentrations (g S l^{-1}); K is the rate constant (g S g X^{-1} h^{-1}); K_s is the saturation constant (g l^{-1}); K_{SI} is the substrate inhibition constant (g l^{-1})

The first term in the right hand side of Eq. (1) represents enzyme utilization rate at low dye concentrations according to Monod equation and the second term represents substrate (dye) inhibition at high concentrations. According to the data presented in Fig 3 a, enzyme utilization rate increased with dye concentration up to 75 g l^{-1} and then decreased for greater dye concentration due to substrate inhibition. For dye concentrations less than 75 g l^{-1}, the inhibition term in Eq. (1) can be neglected and the Eq. (1) takes the following form:

$$v = \frac{kX_o S_o}{k_s + S_o} = \frac{R_m S_o}{k_S + S_o} \tag{2}$$

Where $R_m = K X_o$ is the maximum rate of substrate (dye) utilization in g S l^{-1} h^{-1}.

In the double reciprocal form Eq. (2) takes the following form:

$$\frac{1}{v} = \frac{1}{Rm} + \left(\frac{k_S}{R_m}\right)\left(\frac{1}{S_o}\right) \tag{3}$$

When the experimental data (Table 1) for dye concentrations below 75 g l^{-1} was plotted in form of $1/V$ versus $1/S_o$ the following constants were found for R_m and K_s. Therefore, Eq. (2) takes the following form for $S_o < 75$ g l^{-1}:

$$v = \frac{kX_o S_o}{k_s + S_o} = \frac{17X_o S_o}{570 + S_o} \tag{4}$$

Extremely high value of K_s indicated that the kinetics can be approximated to first order. Since S_o is much lower than K_s (i.e., $S_o/K_s < 0.13$) for $S_o < 75$ g l^{-1}, then S_0 in the denominator may be neglected to yield

$$v = \left(\frac{k}{k_s}\right) X_o S_o = 0.0298\ X_o S_o \tag{5}$$

For dye concentrations above 75 g l^{-1}, substrate inhibition was observed as presented in Fig. 4 a. Therefore, at high substrate concentrations ($S_o > 75$ g l^{-1}) only the inhibition term was considered and the Eq. (1) was approximated to the following expression:

$$v = R_{sm}\left(\frac{k_{SI}}{k_{SI} + S_o}\right) = k' X_o \left(\frac{k_{SI}}{k_{SI} + S_o}\right) \tag{6}$$

In double reciprocal form, Eq.(3) takes the following form:

$$\frac{1}{v} = \frac{1}{R_{sm}} + \frac{S_o}{R_{sm} k_{SI}} \tag{7}$$

When the experimental data for $S_o > 75$ gl^{-1} (Table 1) was plotted in form of $1/V$ versus S_0 the following constants were obtained from the slope and intercept of the line:

$R_{sm} = 1.62$ g S $l^{-1}h^{-1}$, $K_{SI} = 93$ g l^{-1}, K' = 3.24 g $X^{-1}h^{-1}$ since Xo was 0.5 g l^{-1}. Then, Eq. (7) takes the following form:

$$v = k' X_o \left(\frac{k_{SI}}{k_{SI} + S_o}\right) = 3.24 X_o \left(\frac{93}{93 + S_o}\right) \tag{8}$$

V values for $S_o < 75$ gl^{-1} and $S_o > 75$ gl^{-1} were estimated using equations (6) and (8), respectively. Table 1 summarizes the experimental and the predicted values of V for all dye concentrations tested. Good agreement between the predicted and the experimental values of V indicated accuracy of the kinetic constants and the validity of the rate expressions for the experimental conditions used.

4. Conclusions

Dye decolorization using Acid orange 10 was investigated as functions of the substrate (dye) and biomass concentrations using batch experiments. The rate and extent of Percentage decolorization of the dye or dye utilization

increased with increasing dye or dye concentration up to 100 g l^{-1} indicating substrate limitation at low dye or dye concentrations. Further increase in dye concentration above 100 g l^{-1} resulted in gradual decrease in the rate and extent of percentage decolorization indicating substrate inhibition at high dye concentrations. Dye concentrations should be kept below 100 g l^{-1} in batch experiments to avoid substrate inhibition possibly due to high osmotic pressure. Fed-batch experiments may also be used to overcome substrate inhibition at high dye concentrations. Increasing biomass concentrations resulted in improved enzyme utilization and percentage decolorization. Both the rate and the extent of percentage decolorization increased almost linearly with the biomass concentrations between 100 and 200 beads containing approximately 8.9 x 10^6 cells ml^{-1}. Maximum dye decolorization of 99.65% (vv^{-1}) was obtained with 200 beads where there was high biomass concentration. Optimum biomass concentrations above 50 beads were generally advantageous resulting in shorter time period and higher percentage decolorization. Substrate utilization kinetics was found to be first order for low dye concentrations of less than 75 g l^{-1} above which substrate inhibition was observed. The developed kinetic model used was found to be suitable for representation of the experimental data.

Acknowledgement

This study was supported by Anna University, Chennai, India.

References

Aksu Z. Proc. Biochem. (2003). Reactive dye bioaccumulation by saccharomyces cerevisiae,38, 1437- 1444.

Chulhwan P, Byunghwan L, Eun-Jung H, Jinwon L, Sangyong K, (2006). "*Decolorization of acid black 52byfungalimmobilization*".Enz.andMicrob.Technology, 39,371-374.

Field J.A, De Jong E, Feijoo G, De Bont J.A.M. (1993). '*Screeining for lignolytic fungi applicable to the biodegradation of xenobiotics*,' Trends Biotechnol.,Vol. 11, pp. 44-49.

Francis perineau, Jacques M and Antoine G. (1982), '*Adsorption of Ionic dyes on Charred plant material*', J. Chem. Technol. Biotechnol. 32 749-758

Knapp J.S, Newby P.S and Reece L.P. (1995). '*Decolorization of dyes by wood rotting basidiomycete fungi*,' Enz. Micobiol. Technol., 17,664-668.

Loukidou M.X, Karapantsios T.D, Zouboulis A.I and Matis K.A. (2004). '*Diffusion kinetic study of cadmium (II) biosorption by Aeromonas caviae*,' Jl.of chem. Technol Biotechnol., 79, 711-719.

O'Neill C,Freda R.H, Dennis L.H. (1999). "*Colour in textile effluents – Sources, measurements, discharge contents and simulation: a review*, J. Chem. Technol. Biotechnol. 74 (1999) 1009-1018.

Pearce C.I, Lioyd J.R, Guthrie J.T. (2003). "*The removal of color from textile wastewater using whole bacterial cell: a Review*," Dyes Pigments. 58, 179-196.

Field J A, De Jong E, Feijoo G, De Bont J A M., '*Screening for lignolytic fungi applicable to the biodegradation of xenobiotics*,' Trends Biotechnol., 11(1993) 44-49.

Radha K.V, Regupathi I, Arunagiri A, Murugesan T. (2005). '*Decolorization studies of synthetic dyes using Phanerochaete chrysosporium and their kinetics*', Process Biochemistry, 40, 3337-3345.

Sheldon M.S, Small H.G. (2005). "*Immobilization and biofilm development of Phanerochaete chrysoporium on Polysulphone and ceramic membranes*", J. Mem. Sci. 263, 30 -37.

Tien M and Kirk T.K. (1983). '*Lignin peroxidase of P.Chrysosporium'*, Meth. in Enzymol.,161, 238- 249.

Wu J and Yu H. (2006). '*Biosorption of 2,4 dichlorophenol by immobilized rot fungus Phanerochaete chrysosporium from aqueous solutions*,' Biores. Technol., 37,102-106.

Legends for figures:

Figure 1. Enzyme production by the fungus *P.chrysosporium*.

(▲) LiP production (△)MnP production

Figure 2a. Variation of dye concentration with time.

(b) Variation of enzyme activity with time.

Dye concentration (g l^{-1}): (△) 10, (▲) 50, (□) 100, (■) 150, (○) 200 and (●) 225.

Figure 3a. Variation of specific rate of enzyme utilization with dye concentration.

(b) Variation of specific rate of percentage decolorization with dye concentration.

Figure 4a. Variation of enzyme utilization with time.

(b) Variation of percent dye concentration with time.

Biomass concentration (number of beads):

(▲) 25, (▲) 50, (□) 100, (■) 150, (○) 200 and (●) 250.

Figure 5a. Variation of dye utilization rate with initial biomass concentration.

(b) Variation of decolorization rate with initial biomass concentration.

Legends for Table:

Table 1. Experimental and the predicted rate data used for kinetic modeling

Where X_0 = 0.5 g l^{-1}, R_m = 8.5 g S $l^{-1}h^{-1}$, K_{SI} = 570 g l^{-1} and K = 17 g S g X^{-1}

Table 1. Experimental and the predicted rate data used for kinetic modeling

S_o (g l^{-1})	$1/S_o$	$V_{theor.}$ ($gl^{-1}h^{-1}$)	$1/V$	$V_{predicted}$ ($gl^{-1}h^{-1}$)
25	0.04	0.358	2.79	0.357
50	0.02	0.673	1.49	0.685
75	0.013	1.006	1.00	0.988
100	0.01	0.792	1.26	0.781
125	0.008	0.685	1.46	0.690
150	0.0067	0.628	1.59	0.620

X_0 = 0.5 g l^{-1}, R_m = 8.5 g S $l^{-1}h^{-1}$, K_S = 570 g l^{-1} and K = 17 g S g X^{-}

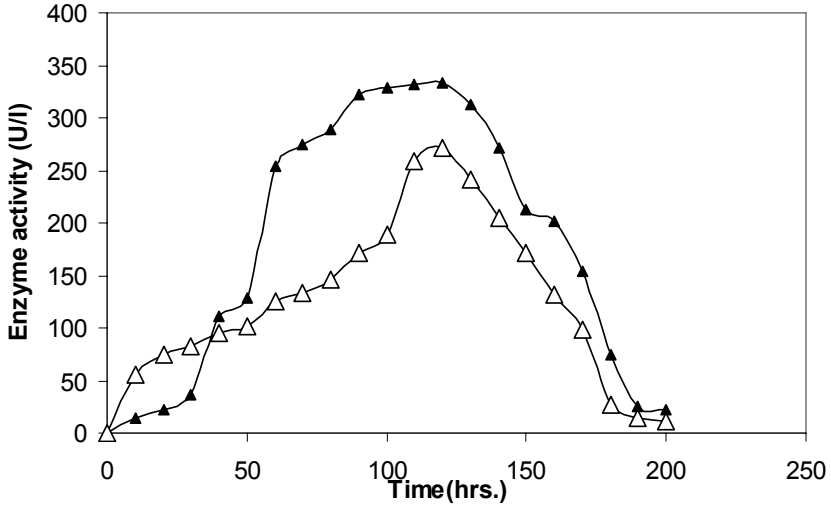

Figure 1. Enzyme production by the fungus *P.chrysosporium*

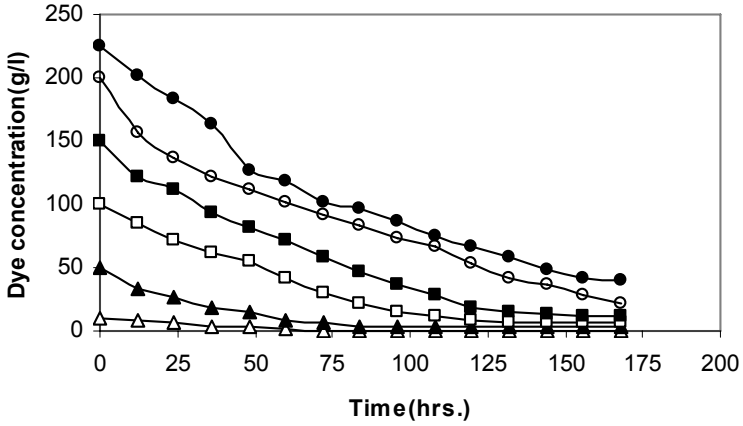

Figure 2a. Variation of dye concentration with time

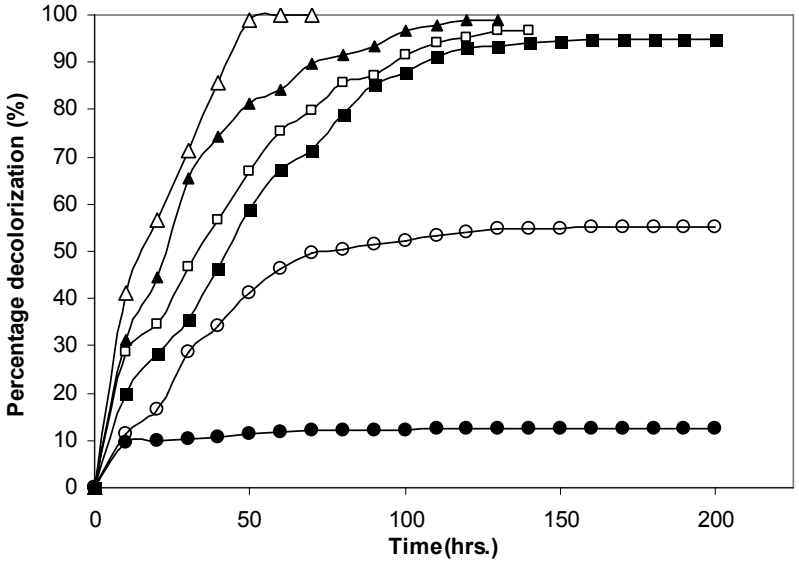

Figure 2b. Variation of enzyme activity with time

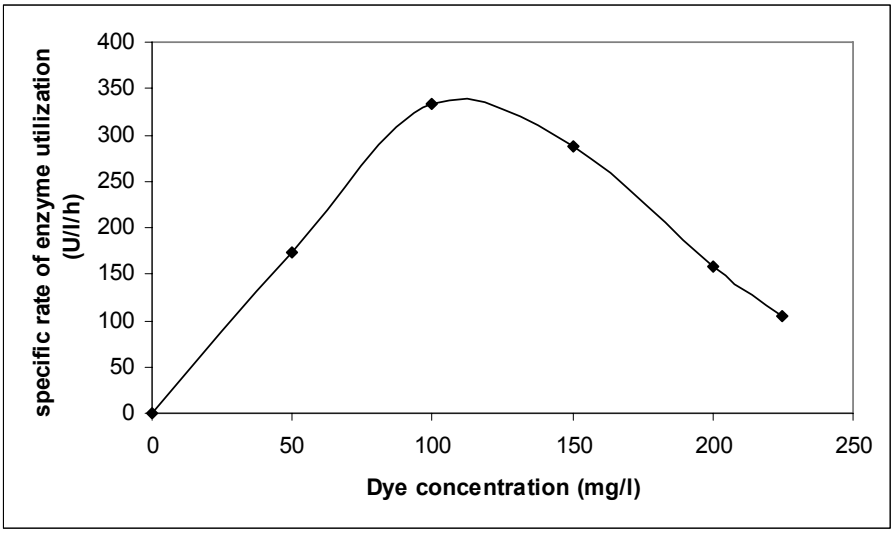

Figure 3a. Variation of specific rate of enzyme utilization with dye concentration

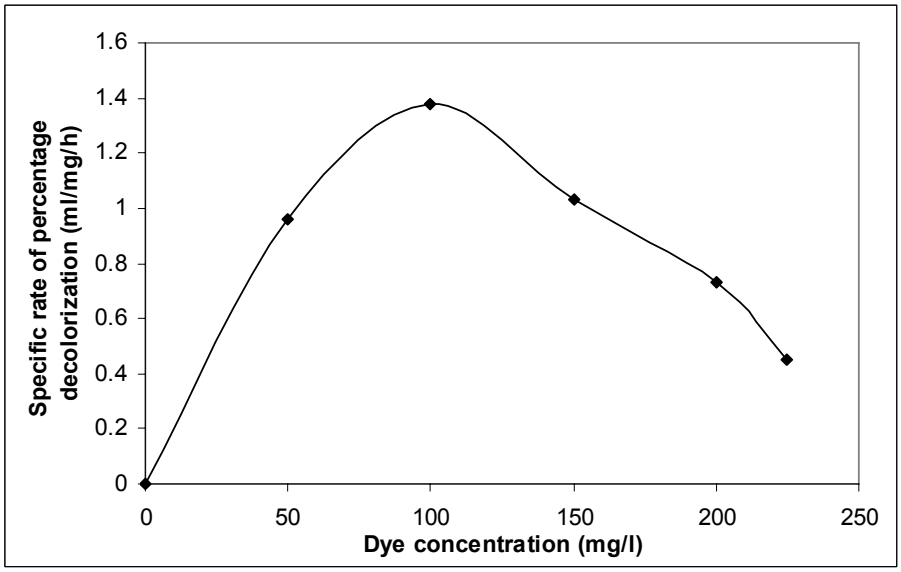

Figure 3b. Variation of specific rate percentage decolorization with dye concentration

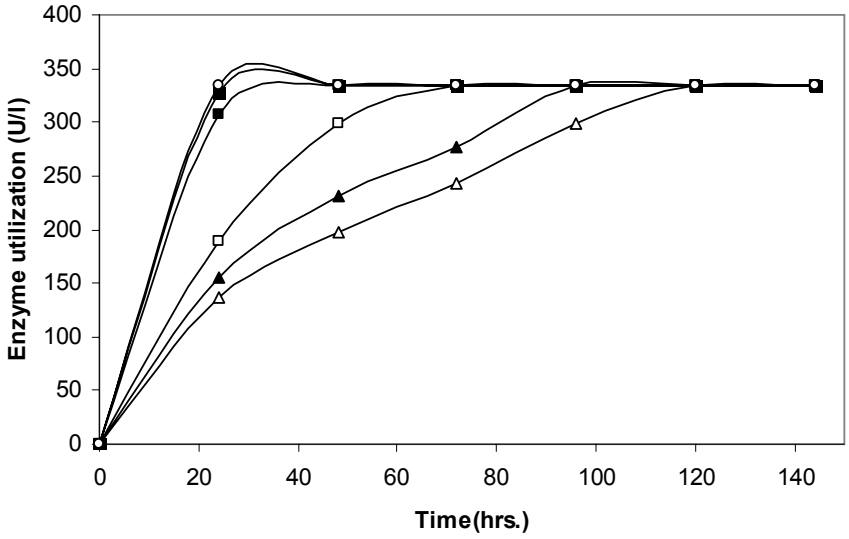

Figure 4a. Variation of enzyme utilization with time

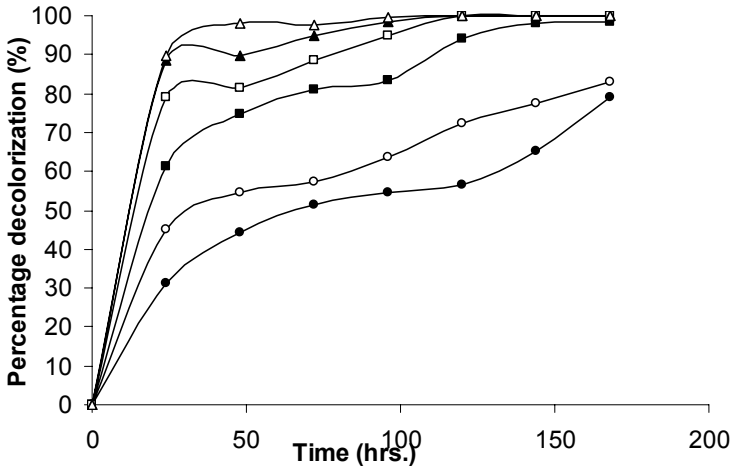

Figure 4b. Variation of percent dye concentration with time

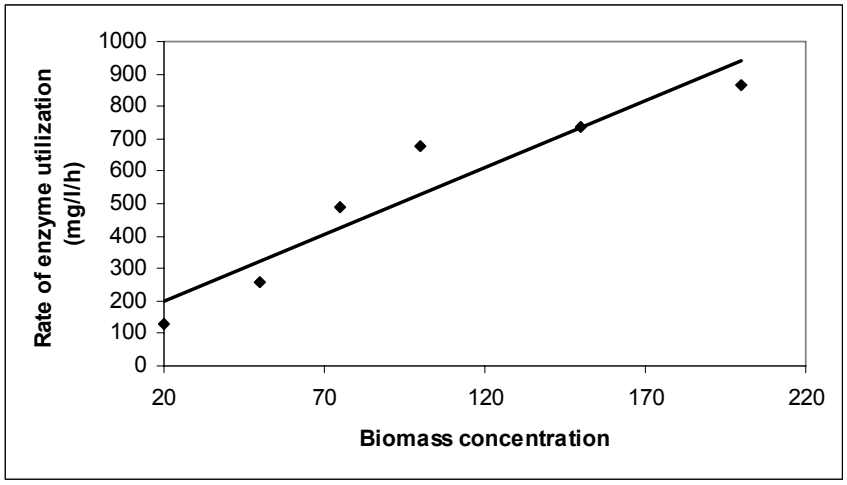

Figure 5a. Variation of enzyme utilization rate with initial biomass concentration

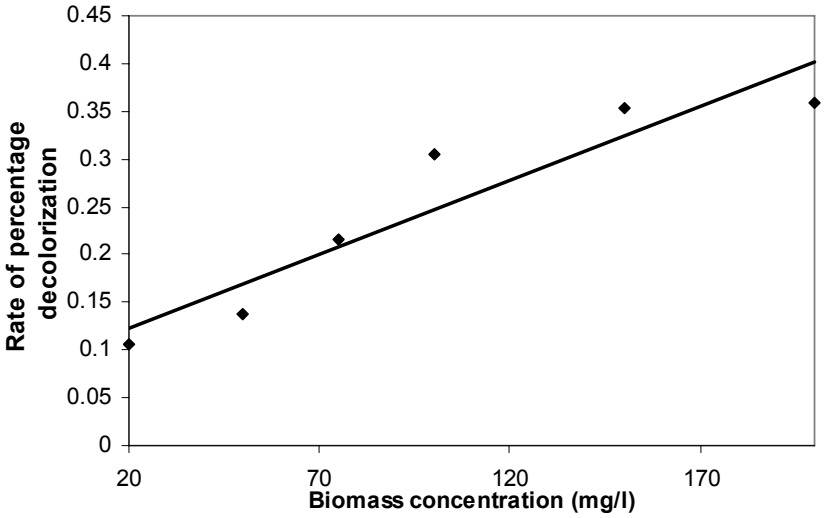

Figure 5b. Variation of decolorization rate with initial biomass concentration

Modern Applied Science

www.ccsenet.org/journal.html

Vol. 3, No. 7

July 2009

Study on Agricultural Insurance Based on Products Marketing

Lixin Tang

School of Management, Yangtzeu University, Jingzhou 434023, China

E-mail: tanglixin@yeah.net

Abstract

Agricultural insurance is a kind of important measure to stable agricultural production and countryside social life. But in China, the development of agricultural insurance faces up with difficult position. This paper analyzes the characteristics of agricultural insurance, introduces overseas agricultural insurance situation, and then puts forward innovative thoughts on agricultural insurance. Agricultural insurance should put a lot of efforts in marketing pattern.

Keywords: Agricultural insurance, Marketing pattern, Grant-in-aid

Introduction

The No.1 documents issued in 2007 by central recently focus the attention on developing modern agricultural activity again. According to statistics of our country, agricultural insurance has increased rapidly in 2006, the income of insurance expenditure got up to 8.5 billion which has increased 16.2 percent compared with the past .The agricultural has become the new point of growth in the insurance business. Our country is a great agricultural nation and natural disaster area. So it's necessary and urgent to accelerate our country insurance innovative.

1. The property of agricultural insurance

1.1 The natural attribute of agricultural insurance

The agricultural insurance has high risk, high payment limited anticipated income etc. Moreover, because of the dispersed service the management expense and the operation cost are all very high. These characteristics have decided the payment ratio of agricultural is higher than the safety line of the normal management in insurance company. According to pertinent data demonstration, from 1985 to 2004, our country Agricultural insurance has only realized two years meager profit, other 18 years was lose completely, the integrate ratio of Agricultural had exceeded 120 percent by far. In order to decrease the ratio of insurance fee and the management cost of insurance company. The integrate ratio of agricultural every government all gives different policy allowance and favorable measures to agricultural insurance so as to guarantee the agricultural insurance has well developed.

1.2 The society attribute of agricultural insurance

The agricultural special status had decided the agricultural insurance is not the pure commodity, but is the public product. It has intensity exterior public and policy type. In the developed country, the government must offer this kind of business operating subsidy, the financial tax revenue preferential benefit, with administrative convenient measure. In order to keep the family income stability, the USA government advocates Agricultural insurance strongly so that farmers, even if due to the loss caused by natural disasters, the payment of insurance can also help them keep the life stable and renew the Agricultural production, thus prevent the bankruptcy of farmers from spreading throughout the basis of economic development and social stability of USA.

1.3 The politic attribute of agricultural insurance

Our country is a great country which has 23 percent of rural population in the whole; the development of agriculture and the stability of the country have an important effect on our country's entire national economy, as well as the coordinated development of country's stability and unity and the steady of development. The development of agricultural insurance can be divided into decentralization and transfer of agricultural risk, which is a significant guarantee to protect the interests of farmers and achieve sustainable development of agriculture under the condition of the market economy. Our country mainly depends on government financial allowance to solve the risks and retrieve peasant agriculture losses for a long period of time. However, because of the limited of the government financial fund, always "emergency hard on the poor", can't solve the problem fundamentally. In contrast, the mature experience of the

overseas as well as some areas' spontaneous practice in domestic shows that changing into the method by marketization, avoiding the risk and compensation loss by the means of insurance is effective.

2. The situation of the agricultural insurance in oversea

2.1 The agricultural insurance of America

In 1938, America promulgated "Federal Crop Insurance Act" and at the same year set up a government agency under the act. The Federal Crop Insurance, which responsibility is operating and managing the nation crop. Beginning in 1939 the implementation of the government crop insurance schemes, thus the federal government opened a history of agricultural insurance. The most prominent feature of agricultural insurance to fund the establishment of official country is crop insurance companies. Its operating system has experienced from the "single-track" and then to the "single-track system" ever-charging. From 1939 to 1980, the federal crop insurance company, at this stage is operated by government agencies alone "single-track system". From 1980 to 1996, in order to improve the participate rate of crop insurance and reduce the supervision costs of crop insurance, the operating system in the US began the introduction of private and commercial insurance companies and insurance agents to participate in crop insurance operatives and product sales, that is, government agencies and commercial co-operation of agricultural insurance company's "dual track". After 1996, the Federal Crop Insurance crop began to exit the business operated by the government of the policy of incentives and subsidies gradually, the private insurance companies start to operate all of the agricultural insurance agent business directly.

American Agricultural Insurance Company has entered a private company to run a separate "single-track system" time. In this "single-track" system, the Federal crop insurance companies are only responsible for formulating regulations to carry out auditing and oversight functions and to provide reinsurance. At present, the model of United States agricultural insurance business can be summarized as follows: private insurance companies operating the original insurance, the government providing reinsurance.

2.2 The agricultural insurance of Japanese

The Japanese government has always attached importance to the legal construction of agricultural insurance, early in 1929 has enacted "Livestock Insurance Act", then in 1938 "Agricultural Insurance Act" has enacted, in 1947 "Agricultural Disaster Compensation Law", then in accordance with the needs of agricultural development, in 1957, 1963, 1966, 1972, 1978, 1985 and 2003, the legal system of agricultural insurance was amended, which provided a strong institutional guarantee for the continued development of Japanese agricultural insurance. The Japanese government premium subsidies to farmers, and the higher insurance rates, the more subsidies of the state treasury. The Government has also undertaken to provide agricultural insurance services team grant (except for liberty insurance business), and has offered reinsurance business for the Masonic federation.

Japanese agricultural insurance adopts the form of Masonic portfolio. Agricultural insuranceis based on cities, towns and villages of the agricultural portfolio for Masonic as the Grass-roots organizations, which is voluntary cooperation of farmers organizations, and conducts agricultural insurance business directly; county-level institutions (both, prefectures) have established the agricultural portfolio Masonic United and have assumed Masonic portfolio reinsurance; the Government as the leading organ of the agricultural insurance portfolio undertake all the re-insurance excluding the share of Masonic insurance. The system of government leadership and agricultural Masonic portfolio that combines up-down pattern of agricultural insurance organizations has formed. Under normal circumstances, the above-mentioned organizations assume their respective proportion of liability insurance as follows: Masonic portfolio 10-20%, Federation of 20-30%, the Government 50-70%. Encountered in heavy disasters, the Government assumes 80-100% of insurance claims. It shows that Japanese agricultural insurance business model is: the original operating Masonic portfolio insurance, Masonic federation provided a combination of reinsurance, the second-level reinsurance provided by the government.

3. Thoughts on Chinese agricultural insurance

Chinese agricultural insurance should not only learn the foreign successful experiences in agricultural insurance, but also find their own suitable agricultural insurance development models: on the one hand the Government needs play an important role in the agricultural insurance, on the other hand, insurance companies should play their subjective initiative, make efforts at promotion modem.

3.1 Intensify the government support to agricultural insurance

3.1.1 Intensify agricultural insurance legislation to protect the development of agricultural insurance in the form of legal ,to ensure that the interests of agricultural producers; the Government should be in the functions and roles in carrying out agricultural insurance with a clear legal form ,to avoid government support agricultural insurance randomness, and to increase awareness of farmer's insurance.

3.1.2 To lighten the scope of agricultural insurance business appropriately and carry out "in order to raise the risk insurance." With the improvement income levels of farmers, the farmers have a lot of insurance needs. Establishing the "big agricultural insurance" concept will include agricultural insurance, including rural areas, agriculture, farmers and other related insurance business into a comprehensive business scope of agricultural insurance companies, that is, we started up traditional farming, aquaculture and other policies agricultural insurance business, at the same time, carried out all agriculture-related property insurance, liability insurance and life, accidental injury insurance business, also boarded in the agricultural insurance implement "based on agriculture (Village insurance) premium farmers (village dangerous)", to make Policy-oriented insurance agency to make additional commercial insurance, to use commercial insurance policy to make up for loss of profits, in order to achieve the means of policy and market a combination , the two complementary advantages.

3.1.3 The Government makes financial subsidies, tax concessions to agricultural insurance. Support for agricultural insurance should make full use of policy instruments to formulate preferential and flexible support policy to support the development of agricultural insurance.

3.2 In terms of insurance companies should make an affect even more miserable

3.2.1 The design agricultural product must act according to circumstances

In 2003, PICC Property Insurance Company in Jilin Province has launched the "Jin Lu Yin He" series of insurance products, including comprehensive agricultural risks insurance, the self-insurance of rural family and so on. Currently the part of the series products has been extended to the whole country and has gotten well social benefits. At the same time, Jilin People's Insurance National Insurance also have increased demand for insurance to the scarcity of national forest resources and plant fast-growing trees situation, have adjusted a forest fire products, and have developed the forest insurance effectively; In addition, the business of rural small credit insurance business also have been exploited.

In 2004, Jilin People's Insurance focus on the design and promotion of the series of"Jin Lu Yin He "'s combination of 11 products, the first national property portfolio risk insurance industry of insurance products marketing first, put the needs of rural production and living of the family property, personal injury, post-harvest crops, livestock, General Electricity, development of students early childhood, transport of agriculture, and other cadres to practice risk groups divided according to different needs and meet the new requirements of the development of the rural economy effectively.

The past two years, close to People's Insurance according to different consumer groups designed different kinds of insurance products - for specialized work to adapt or go out to populations in need of the physical design of a traffic accident fixed insurance products to meet the child care needs of students in low-cost fixed policy, to adapt to a lower level of rural income needs of low-cost combination Nongjiale policy, to adapt to high-income level of rural households in the demand for new mid-priced portfolio of insurance products in rural areas, according to urban and rural areas designed to ease sharing of accidental injuries, such as a fixed policy promulgated successively later. It is the demand from farmers, the refinement of insurance consumer demand before the agricultural insurance has been the development of space.

3.2.2 The marketing model based on Agriculture.

In the new situation of insurance market, the promotion pattern of agricultural insurance will certainly changed dramatically. Now, we need to make the most use of the situation in the rural network, at the same time, downward the rural insurance promotion services division continuously. Now individual marketing teams have been extended to the rural county town gradually. And, we should take advantage of the banks, postal services and other agencies and industry to spread villages, with the help of electricity, credit cooperatives, village committees, etc, to agent insurance services widely. In particular, we should cooperate with the Net of the rural road safety projects, so as to provide risk protection for farm vehicles. According to statistics, at the end of June 2006, Jilin People's Insurance Rural Insurance promotion Services has grown to 309, and 495 salesmen. Agencies and industry have developed to 31 in rural.

3.2.3 The development of agricultural insurance based on Agro-enterprise

Current agricultural industrialization economic organizations, especially large-scale agricultural products processing enterprises rapid development of the first farmers, enterprises and farmers on the requirements of the growing insurance business, take part in the proportion of insurance constantly improve, to expedite the development of agricultural insurance to provide a wealth of insurance resources. Under the situation of the Policy-oriented agricultural insurance haven't started yet , if commercial insurance companies can make full use of existing institutions network, portfolio of property, cargo, liability, accident insurance and other insurance products, the rapid classification of batches covering the first agricultural enterprises, can make agricultural insurance developed rapidly .

Head of agricultural industrialization of agricultural enterprises are at or above the county head government offers various kinds of support and validation for naming a large scale, organization Driven many farmers, good reputation, high-tech, management stability, anti-risk ability and so on. Practice shows that the better the quality of such enterprises,

Loss Prevention convenient, low pay, the overall risk. Agro-enterprises through the first contact farmers, can change over the past one to do a traditional model of insurance, unified propaganda guidance, unity insurance, disaster prevention, claims, Greatly reducing the operating costs of insurance companies, insurance companies or Marketing Support Services Department can undertake this region-related businesses

Insurance salesman from taking the string Tuen retail direct sales model to the rural credit cooperatives, the Agricultural Bank and other institutions and industry promotion channel model; From farmers for the dispersion of bulk single-sales services for the agricultural industry groups EC single-sales Service, insurance companies, promotion service model should be the expansion of diversification. It is precisely this mixed pattern of changes in marketing, in a sense in order to break through a long period of time constraints in the development of rural insurance business huge human inputs and material costs, low rate of business development and some other problems.

References

Gao, Wei. (2007). The inspiration of Japanese Agricultural insurance development. *The financial of Xi'an*. 2007. 02. 12-14.

Guo, wenchao & Liang, Hong. (2006). The research about the model of our country's Agricultural insurance. *The theoretical*. 2006. 12. 62-65.

Shang, Xiaoyang. (2006). Agricultural insurance: Government Units to sing good ride.*China Securities*. 2006. 09-20.

Sun, Rong & Huang, Yingjun. (2007). The Development of Our country's Agricultural insurance:Recalling, Present situation And Prospects. *Ecological economy*. 2007-01. 26-33.

Modern Applied Science

www.ccsenet.org/journal.html

Vol. 3, No. 7

July 2009

Prediction of the Coating Thickness of Wire Coating Extrusion Processes Using Artificial Neural Network (ANN)

Bekir Cirak (Corresponding author)

Department of Mechanical Engineering

Naturel Science Instutie, Sakarya Unıversıty, Adapazarı – TURKEY

E-mail: bekircirak@mynet.com.tr

Recep Kozan

Department of Mechanical Engineering

Engineering Faculty, Sakarya Unıversıty, Adapazarı – TURKEY

E-mail: kazan@sakarya.edu.tr

Abstract

This paper presents a new method of modeling the nonlinear parameters of a coating systems base on neural Networks with artificial neural network neurons. Artificial neural networks (ANNs) are a new type of information processing system based on modeling the neural system of human brain. The wire coating thickness and quality depend on the wire speed, polymer viscosity, polymer melt temperature and the gap between the wire and exit end of the die. In this paper, results of experimental investigation are presented by comparing the coating quality on galvanized mild steel wire using EP 58 PVC molten is used as the coating material in a wire coating extrusıon unit at different extruder temperatures and extruder speeds.

The coating thickness and quality are also discussed for different wire speeds of up to 15 m/s. A three layer back propogation artificial neutral network (ANN) model was used for the description of wire coating thickness.On comparing the experimental data, the predictions the ANN model predictions, it is found that the ANN model is capable of predicting the coating thickness. The neural network model shows how the significant parameters influencing thickness can be found. Inthis studies, a back propagation neural network model is developed to map the complex non-linear wire coating thickness between process conditions .

Keywords: Wire coating extruder, Coating thickness, Artificial neural network (ANN), PVC, Extrusion

1. Introduction

Polymer coating is often applied to wires, strips, tubes or ropes for insulation or protection against corrosion. There are three different methods which are mostly used for this coating process. These methods are coaxial extrusion, dipping and electro-statical deposition process. The first two processes can be reasonably fast but bonding between the continuum and the coating material is not so strong. The third process offers much stronger bonding but is relatively slow. If the coating material can be forced onto the continuum uniformly the bonding can be improved significantly.

Artificial neural network (ANN) computing was originally inspired by the operations of biological brains. It was developed to simulate the strong learning, clustering and reasoning capacity of biological neurons.With a strong learning capability and use of parallel computation and nonlinear mapping, neural networks can be successfully applied to identifying several nonlinear systems and control problems.

The analysis for different coating processes could be found in the literature. Hydrodynamic wire coating with Nylon 6 using a tapered bore pressure unit has been presented.(B. Caswell, R.I. Tanner, 1978)(C.L. Tucker, 1989)(H. Zhang, M.K. Moallemi, S. Kumar, 1991)

Coextrusion method for coating has been studied theoretically and experimentally. (S. Nakazawa, J.F.T. Pittman, 1982)(V.S. Mirnov, 1993)

Present study of dip coating process. An experimental study of the electro-statical deposition process has been presented.

A continuously increasing number of commercial products are produced by polymer extrusion using plasticating extruders, which are among the most widely used equipments in polymer process industry.The extrusion process has a

standard setup includinga feeding section, a barrel and a head with a die for shaping. In the feeding section, the solid polymer is fed into the extruder through a hopper in the form of pellets or irregular small bits. Then, the polymer is transported along the barrel by means of a rotating screw.

A continuously increasing number of commercial products are produced by polymer extrusion using plasticating extruders, which are among the most widely used equipments in polymer process industry.

The extrusion process has a standard setup including a feeding section, a barrel and a head with a die for shaping. In the feeding section, the solid polymer is fed into the extruder through a hopper in the form of pelletsor irregular small bits. Then, the polymer is transported along the barrel by means of a rotating screw. The barrel wall is equipped with a number of electric heaters which melt the polymer. The material is melted and pushed towards the die where the extruded final product is shaped and expelled. During the process, the polymer undergoes very complex thermo-mechanical transformations inducing strong changes in the physical properties of the material.(Ming-Der Jean, Chyuan-Du Liu, Jen-Ting Wang, 2005)

A high-quality extrusion is essentially characterized by a precisely-regulated output volumetric flow; this can be achieved by finely regulating the temperature and the pressure of the die at the output of the extruder (Noriega, del pilar, & Rauwendaal, 2001).(Hulya Kacar Durmus, Erdogan Ozkaya,Cevdet Meric, 2004)

Paste extrusion is widely used in the food, chemical, ceramic and pharmaceutical industries. Recently, issues arise in the electrical industry for manufacturing superconducting wire and for carrying out electrical insulation of superconducting cables by extrusion. It can thereby be seen that the role of paste extrusion is important in many industries. The process generally involves paste preparation, die extrusion, drying, and firing in order to create a final product. Benbow and Bridgwater have summarised the stages for forming products. Paste flow and the material properties are crucial factors for product quality. Studies including the effect of the particle size binder material , carbohydrate, liquid-phase rheology and mixing procedure on the extrusion process and the extrudate have been carried out.(C.D. Han, D. Rao, 1978)

The barrel wall is equipped with a number of electric heaters which melt the polymer. The material is melted and pushed towards the die where the extruded final product is shaped and expelled. During the process, the polymer coating is often applied to wires, strips, tubes or ropes for insulation or protection against corrosion. (fig.3)

The plasticating extruder is one of the main pieces of equipment used in the polymer processing industries. As plastics is found more uses, with more stringent quality specifications, the methods of increasing polymer production while improving product quality are needed. Extrusıon molding is the most widely used process in manufacturing plastic products. Since the quality of extrusıon coated plastic parts are mostly influenced by process conditions, how to determine the optimum process conditions becomes the key to improving the part quality.(S. Basu, 1981)

2. Material and experimental procedure

In this study, EP 58 PVC coating plastic material was used as test material. The material was supplied from EL-Kİ KABLO (Manisa/Turkey). The experimental value and datas is given from this company (Table 1)

The die heating zones were maintained at the same temperature, which was also varied during the experiments.The some of temperatures for each heating zone (barrel) and the different screw speeds are shown in Table 1. Sixty combinations were tested for their effect on the parameters of the extruded parts. The process settings were varied randomly and continuously; i.e. without stopping the process. Each setting was allowed to run. Table 1 shows first 30 experimental value used in training and other 30 experimental value used in testing.

To measure the coating thickness, each sample is measured at five different positions along its length by a micrometer and the average diameter of the coated wire is noted. A small portion of the wire sample is cold mounted and polished. An optical microscope is then used to assess the actual coating thickness and the concentricity of the coating on the wire. Fig.1. shows geometry model and this model to consist of an optical microscope.

The geometry gives distance of coating centre between wire centre of wire coating section.In this paper, the wire coating states of an industry example, shown in Fig. 2, was studied. The polymer material used for coating the cover is PVC.

Also the geometry gives distance of coating centre between wire centre of wire coating section.The other words, the eccentricity (unüniform coating) and concentricity (üniform coating) of the wire coating states of an industry example, shown in Fig.3 was studied. Fig.3 shows the state of eccentricity of the coating on wire with wire velocity of 2050 d/dk (15 m/s) and extruder temperature of 150 ◦C. Fig. –b shows the quality of concentricity of coating at wire velocity of 2065 d/dk (19 m/s) and extruder temperature of 175 ◦C.The coating is not absolutely concentric but for general application is considered to be satisfactory.

The experimental set up consists of the drawing bench, the wire bobbine, the cooling pool, the drive system (electrical motor), the polymer feeding and melting unit (extruder) and the drawer and winder unit. A schematic diagram of the process is shown in Fig. 4.

The polymer granules are filled in the hopper and the hopper is connected to the body of extruder.

The process parameters for the investigations carried out were as follows. Polymer characteristics Polymer type EP 58 PVC, Polymer melt temperature 150 – 200 ◦C and Wire characteristics Wire diameter 1,40 mm(0,20 x 7 mm), Wire material Galvanized mild steel. Experimental work was carried out at polymer melt temperatures of 150, 185 and 200 ◦C.

A pvc compound was prepared using a proprietary formula which includes PVC resin, foaming (blowing) agent, heat stabilizer, lubricant, process aid, and filler. The extrusion process parameters; i.e. barrel heating zones' temperatures and screw speed were varied systematically and in random order to vary of the extruded parts.(S. Akter, M. S. J. Hashmi, 2006)

The available extruder incorporated three heating zones along the barrel and two independent heating zones at the die sections. In order to maintain a constant heat profile in the barrel, the ratio between the three heating zones was fixed during all experiments while varying the temperatures of all three barrel zones accordingly.

3. Artificial neural networks

In recent years artificial neural networks (ANNs) have emerged as a new branch of computing, suitable for applications in a wide range of fields. Artificial neural networks have been recently introduced into plastic extrusıon.(Geng-Qun Huang, Han-Xiong Huang, 2007)

In this study, experimental and ANNs results have been compared. A lot of studies have been published in which the prediction of various parameters on coating thickness were investigated systematically.S.Akter,M.S.J. Hashimi of paper is presents a new neural network approach to polymer coating extrusıon.(B. Caswell, R.I. Tanner, 1978)

Among the several proposed types of artificial neural network models, the back propagation network is the most extensively used learning algorithm that includes nodes with continuously differentiable activation functions. Each node performs a particular nonlinear operation that involves a weighted sum of its inputs. Its outputs are fed into trained nodes. The error at each neuron or node is calculated and the weight for each neuron is modified until the desired error between the actual and the required output is achieved. A well-trained ANN can be used to simulate and predict the output response for various control factor-level settings. (Geng-Qun Huang, Han-Xiong Huang, 2007)

ANN method is proposed to optimize the polimer extrusıon process. In this method, a back propogatıon neural network model is developed to map the complex non-linear relationship between process conditions and quality indexesof the extrusıon coated parts.

In this study, we use a three-layered back propagation network that includes an input layer, a hidden layer and an output layer shown in Fig.5, Fig.6 and Fig.7.

Artificial neural network (ANN) is a data modeling tool that is able to capture and represent the complex relationship of the input and output data. Back-propagation neural network is the most widely used neural network. It has feed forward network architecture constituted by a set of processing units, also known as neurons, which are arranged in a layered structure. The connections between the units are weights, which are used to store the knowledge of the network. The Back-propagation neural network has been applied in many engineering applications.(Nidal H. Abu-Zahra, Ashish Seth, 2002)

A back propagation can make accurate predictions when applied to the coating treatment process because it can model complex nonlinear, multiple functional relationships using training and testing samples for self-learning and recalling.

3.1 Structure of an ANN model for coating thickness

Many different process parameters affect the quality of the extrusıon molded products. Variables with greater influence on the part quality need to be selected in order to simplify the problem by saving both the sample collecting time and the computing time.

In this paper, the selection of process variables as inputs of ANN model is based on the relative significance of each variable on the objective performance. The neuron number of the input layer of ANN is determined by the number of variables selected, and the neuron number of the output layer is determined by the number of the objective indexes.

In this paper, a three-layer ANN model with one hidden layer was used, where the neuron number of the hidden layer was determined by trials. The transfer function between the input layer and the hidden layer is 'Tansig', while the transfer function between the hidden layer and the output layer is 'Purelin'.

The architecture of a neural network depends on its network topology, transfer function, and learning algorithm. A typical Back-propagation neural network, as shown in Fig. 4, is composed of three layers, namely, input layer, hidden layer, and output layer. (Shen Changyu, Wang Lixia, Li Qian, 2007)

ANNs are widely accepted as a technology offering an alternative way to simulate complex and ill-defined problems. They have been used in diverse applications in control, robotics, pattern recognition, forecasting, power systems, manufacturing, optimization, signal processing, etc., and they are particularly useful in system modeling.

A neural network is a computational structure, consisting of a number of highly interconnected processing units called neurons. The neurons sum weighted inputs and then applies a linear or non-linear unction to the resulting sum to determine the output and the neurons are arranged in layers and are combined through excessive connectivity. (Nidal H. Abu-Zahra, Ashish Seth, 2002)

Back propagation network is a typical ANN that has been widely used in many research fields. Back propagation network have hierarchical feed forward network architecture, and the outputs of each layer are sent directly to each neuron in the layer above.(Ming-Der Jean , Chyuan-Du Liu, Jen-Ting Wang, 2005)

Back propagation network are trained by repeatedly presenting a series of input/output pattern sets to the network. The neural network gradually 'learns' the governing relationship in the data set by adjusting the weights between its neurons to minimize the error between the actual and predicted output patterns of the training set. A separate set of data called the test set is usually used to monitor network's performance.

When the mean squared error (MSE) of the test set reaches a minimum, network training is considered complete and the weights are fixed. In essence, a neural network is a function that maps input vectors to output vectors.(Nidal H. Abu-Zahra, Ashish Seth, 2002)

The outputs of the neurons in the input layer are same as their inputs shown in Eq. (1) for the hidden layer, each neuron receives total outputs from all of the neurons in the input layer as

$$\mathrm{net}_j = \sum_{i=1}^{n} w_{ij} x_i + \theta_j \qquad (1)$$

where net*j* is the net input to the *j*th neuron in the hidden layer, *n* the number of neurons in the input layer, *wij* the connection weight from the *i*th neuron in the input layer to the *j*th neuron in the hidden layer, *xi* the input to the *i*th neuron in the input layer, and *θj* is the threshold value of the *j*th neuron in the hidden layer.

The output of a neuron in the hidden layer is calculated by applying the net input to a transfer function. The sigmoid function shown in Eq. (2) was used as the transfer functions between input layer and hidden layer.

$$y_j = f(\mathrm{net}_j) = \frac{1}{1 + e^{\mathrm{net}_j}} \qquad (2)$$

For the output layer, the output of the neurons is shown in Eq. (3)

$$o_k = \sum_{j=1}^{m} w_{jk} y_j + \theta_k \qquad (3)$$

where *ok* is the output of the *k*th neuron in the output layer, *m* the number of neurons in the hidden layer, *wjk* the connection weight from the *i*th neuron in the hidden layer to the *k*th neuron in the output layer, *yj* the output from the *j*th neuron in the hidden layer, and *θk* is the threshold value of the *k*th neuron in the output layer.(Shen Changyu, Wang Lixia, Li Qian, 2007)

In this work, a back propagation neural network model was developed to build the relationship between parison thickness distribution and the objective function. The thicknesses of 0.5 positions arranging uniformly along the parison were selected as input parameters for the ANN model. The output parameter was the objective function value.

The architecture of a neural network depends on its network topology, transfer function, and learning algorithm. A typical back propagation neural network, as shown in Fig. 8, is composed of three layers, namely, input layer, hidden layer, and output layer.

There is no definite rule available to determine the appropriate number of neurons in the hidden layer. In this paper, it was determined by a trial and error method. The results showed that the ANN model with 13 neurons in the hidden layer could give a better converging rate and generalization. The architecture of the ANN model used in this work is shown in Fig.8.

The ANN model for the coating thickness variation of the part built by the above methods is shown in Fig. 8. The node number of the hidden layer was determined by train trials and the final value obtained was 9, that made the configuration of ANN as 6–9–1.

A neural network system is presented for use in wire coating process. The tan-sigmoid transfer function was used as the activation function for the hidden layers, and linear transfer function was used for the output layers. Network architecture for coating thickness and the contrast of prediction results and numerical experiment results of relationship between coating thickness variation and process parameters are shown in Fig. 8.

All the input and target data were scaled in the range between [0.1, 0.9] using the following normalization equation shown in Eq. (4)

$$V' = \frac{V - V_{\min}}{V_{\max} - V_{\min}} \times 0.8 + 0.1 \qquad (4)$$

where V is the original data, Vmin and Vmax the minimum and maximum values of V, respectively, and V is the normalized data of the corresponding V. Totally 300 patterns were obtained from numerical simulation by changing the thickness distribution of the coating surface along its length.

Among them, 270 patterns were used as training ones. Once the mean square error (MSE) for the training patterns reduced within a given tolerance (set at 10−6 in this work), or the number of training iterations reached a predetermined one (set at 1000 in thiswork), the network-training course was stopped. Fig.9 shows iteration number versus mean square error for training nonlinear coating thickness.

The results of training and testing are confirmed experimentally. According to the back propagation models, the R2 for training and for testing is 0.924 and 0.822, respectively, which means that the experimental hardfacing roughness values and their predicted values are strongly linear for both models. The values predicted by the back propagation model analysis yield a best-fit average percentage error of 4.61% from the actual data.

Figs. 10 show the development of training and testing RMS errors for 8-18-1 and 8-18-18-1 neural models over 10,000 learning epochs

The 8-18-1 neural network models, which exhibit well-trained network performance, are superior to the other networks used because the RMS errors for training and testing are rapidly minimized, converging to 0.035 and 0.061 following after 4400 learning epochs, respectively.

Fig.11 shows the evolution of the mean square error of the ANN model during training. The trained network model was validated for its predictive capability.The result indicates that the ANN has a good performance graphics in Fig. 11.

3.2 Train/test samples

This paper deals with the ability of the varied step of each variable is set to obtain a series of set-point values of variables inside the varied range based on baseline. The samples of all set-points are then assigned as input–output data to train and test the ANN. The samples are randomly divided into two groups.

Those samples including the baseline set were methodically assigned to the training set, and all the remaining samples were assigned to the test set. After being trained, the ANN model can map the non-linear relationship between quality indexes and variables of injection molding. It can then be used in the optimization of online process conditions and the part quality control of molded products.

The contrast of prediction results and numerical experiment results of relationship between coating thickness variation and process parameters are show in Fig. 10. The result indicates that the ANN has a good performance, and it can accurately map the relationship between the volumetric shrinkage variation and the process parameters. First 30 experimental value used in Training and other 30 experimental value used in Testing at table 1.

The simulation function based on the ANN was used as the objective function of the optimization problem, and the process window for each variable as given above was used as the boundary restrictions.

The remaining 89 samples were then used to test and to train the performance of the ANN. As shown in Fig. 12,13 most of the samples have consistent outputs of ANN prediction and numerical experiment, and the result is quite satisfactory. Once the optimal ANNs was designed, the ANNs were trained and used to predict coating thickness for various set of environmental conditions (Figs.14).

The results obtained in ANNs application are close to test results. Therefore by using trained ANNs values, the intermediate results that were not obtained in the tests can be calculated. Two value have been selected for test phase (Figs.15).

The number of the hidden layer with 18 neurons is obtained from Table 2. Table 2 reveals that the suitable number of neurons in the hidden layer is determined by trial and error. However, 11 neural network constructs are obtained using the MATLAB1 interface. The 6-9-1 and 6-13-1 neural models both have small and stable RMS errors for various constructs, respectively.

Fig. 16. shows the experimental data and the predictions of the coating thickness by employing an ANN The process of extrusion was carried out with a sequence of eight extruder velocities, 505, 500, 495, 490, 485, 480, 475 and 470 rpm represented by v1 to v8, respectively.

Fig. 17 and 18. Shows experimental data and predictions of extruder screw speed with coating thickness by the 6 -13 – 1 ANN model. Also experimental data and predictions of extruder screw speed with coating thickness by the 6 - 9 - 1 ANN model. 6-13-1 ANN model is prefer one of this models.

Fig. 19 shows the drawing force at a temperature of 150◦C. The theoretical drawing force has also been shown in this figure. The drawing force generally increases with the increase in the wire velocity. The theoretical drawing force matches well with the experimental force though it is slightly higher in magnitude.

Fig. 20 shows the coating thickness for ep 58 pvc at the extruder temperature of 150 ◦C. These tests were carried out at wire velocities of up to 16 m/s. The coating was continuous and the thickness was uniform at 0.05mm over the entire range of velocities.The pvc melt started to burn as the melt temperature increased beyond 120 ◦C. This degradation of polymer led to slightly lower quality coating at higher wire velocities.

However, the coating on the polymer for different ranges of velocities, and melt temperatures appeared to be concentric. Some samples were prepared and polished for examination under an optical microscope. The cross section of the wire was observed to be circular and the coat ing was reasonably concentric.

Fig.3-a illustrates the coating concentricity at extruder temperature 175 ◦C and wire velocity of 19 m/s which appears to be slightly eccentric. Fig.3-b shows the coating is reasonably concentric. Results the quality of concentricity of the coating on wire with extruder temperature 150 ◦C and wire velocity of 15 m/s .

4. Conclusion

This paper has presented knowledge based and neural network approaches to wire coating for polymer extrusıon. Experimental results of wire coating extrusıon with EP 58 PVC have been presented. Due to some limitation in the present experimental set up the drawer speed is limited to about 16 m/s. Therefore, experiments were carried out within the speed range of up to 15 m/s. The polymer coating on the wire is continuous for speeds of up to 15 m/s.

The bonding quality of the coating with wire was found to be very good. Concentricity is beter in the case of extruder with screw speed 485 rpm and wire velocity 2050 rpm (15 m/s.) Application of screw speed and wire velocity (drawer speed) generally improves the quality of the coating.

Conventional wire coating with EP 58 PVC using a tapered bore die unit has been presented. The experiments were carried out within the speed range between 2 and 15 m/s. The polymer coating on the wire is continuous and concentric for speeds of up to 16 m/s. The concentricity quality of the coating with wire was very good.

References

B. Caswell, R.I. Tanner, (1978). Wire coating die design using finite element methods, *Polym. Eng. Sci.* 18 (5(April)) 417–421.

C.D. Han, D. Rao, (1978). Studies on wire coating extrusion. 1. The rheology of wire coating extrusion, *J. Polym. Eng. Sci.* 18 (October) 1019–1029.

C.L. Tucker, (1989). Computer Modelling for Polymer Processing, Hanser Publishers, Munich, Vienna, New York, pp. 311–317.

Geng-Qun Huang, Han-Xiong Huang, (2007). Optimizing parison thickness for extrusion blow molding by hybrid method, *Journal of Materials Processing Technology.* pp. 512–518 Center for Polymer Processing Equipment , China

H. Zhang, M.K. Moallemi, S. Kumar, (1991). Thermal analysis of the hot dipcoating process, *journal of heat transfer in metals and container less processing and manufacturing,* ASME 49–55.

Hulya Kacar Durmus, Erdogan Ozkaya,Cevdet Meric, (2004). The use of neural networks for the prediction of wear loss and surface roughness of AA 6351 aluminium alloy, department of mechanical engineering. p.p. 201-205 Celal Bayar University, Manisa / Turkey

Ming-Der Jean , Chyuan-Du Liu, Jen-Ting Wang, (2005). Design and development of artificial neural networks fordepositing powders in coating treatment , applied surface science. p.p. 290–303 *Computer Science, and Statistics*, State University of New York USA

Nidal H. Abu-Zahra , Ashish Seth, (2002). In-process density control of extruded foam PVC using wavelet packet analysis of ultrasound waves, Industrial and Manufacturing Engineering Department, University of Wisconsin-Milwaukee, pp. 1083-1095 USA

S. Akter , M . S . J . Hashmi, (2006). wire drawing and coating using a combined geometry hydrodynamic unıt : theory and experiment , *journal of materials processing technology*, pp. 98 – 110 Ireland

S. Basu, (1981). A theoretical analysis of non-isothermal flow in wire-coating co-extrusion dies, *J. Polym. Eng. Sci.* 21 (December) 1128–1137.

S. Nakazawa, J.F.T. Pittman, (1982). A finite element system for analysis of melt flow and heat transfer in polymer process, in: Numerical Methods in Industrial Forming Process, Pineridge Press, Swansea, UK, 1982, pp. 523–533.

Shen Changyu, Wang Lixia, Li Qian. (2007). Optimization of injection molding process parameters using combinationof artificial neural network and genetic algorithm method, *National Engineering and Research Center for Advanced Polymer Processing Technology.* (2007). pp. 412-418 Zhengzhou University, China

V.S. Mirnov. (1993). Increase of polymer coating wear resistance by electrophysical modification, in: P.K. Datta, J.S. Gray (Eds.), *Surface Engineering: Engineering Applications*, vol. II, The Royal Society of Chemistry, 1993, pp. 80–90.

Table 1. Range of experimental process parameters

EXPERİMENTAL VALUES : 1- a , 1-b								
EXPERİMENTAL NAME : Wire Coating Thickness (t)								
WİRE DİAMETER : 1,40 mm (7 x 0,20 mm)								
EXPERİMENTAL TYPE : Concentricity , Eccentricity								
COATİNG MATERİAL : EP 58 PVC								
TİME İNTERVAL : 10 min.								
	İNPUT						OUTPUT	ANN
	Screw Speed (rpm)	1.Barrel Heating (°C)	2.Barrel Heating (°C)	3.Barrel Heating (°C)	Die Heating (°C)	Wire Velocity (d/dk)	Coating Thickness (mm)	
Setting Value	485	103	150	160	165	2050	0,5	
No								
1	485	103	147	159	166	2050	0,495	First 30 experimental value used in Training and other 30 experimental value used in Testing
2	486	102	147	160	166	2050	0,496	
3	485	104	148	161	165	2053	0,496	
4	487	103	150	160	165	2052	0,495	
5	485	103	150	165	165	2050	0,497	
6	484	105	149	161	165	2051	0,496	

54	484	102	147	159	165	2049	0,495	
55	485	104	150	160	165	2048	0,495	
56	486	103	149	159	165	2051	0,496	
57	485	105	149	161	166	2049	0,498	
58	484	106	148	159	166	2050	0,499	
59	483	102	147	159	166	2051	0,5	
60	484	103	149	159	165	2050	0,5	

Table 2. The various RMS errors of ANN models through learning epochs

Number of trials	Neuron of input-hidden-output	RMS error of training sample	RMS error of testing sample
1	6-8-1	0.03482	0.06143
2	6-9-1	0.03482	0.06168
3	6-10-1	0.03482	0.06210
4	6-11-1	0.03482	0.06151
5	6-12-1	0.03481	0.06164
6	6-13-1	0.03481	0.06158
7	6-14-1	0.03481	0.06165
8	6-15-1	0.03485	0.06157
9	6-16-1	0.03483	0.06166
10	6-17-1	0.03482	0.06157
11	6-18-1	0.03483	0.06161

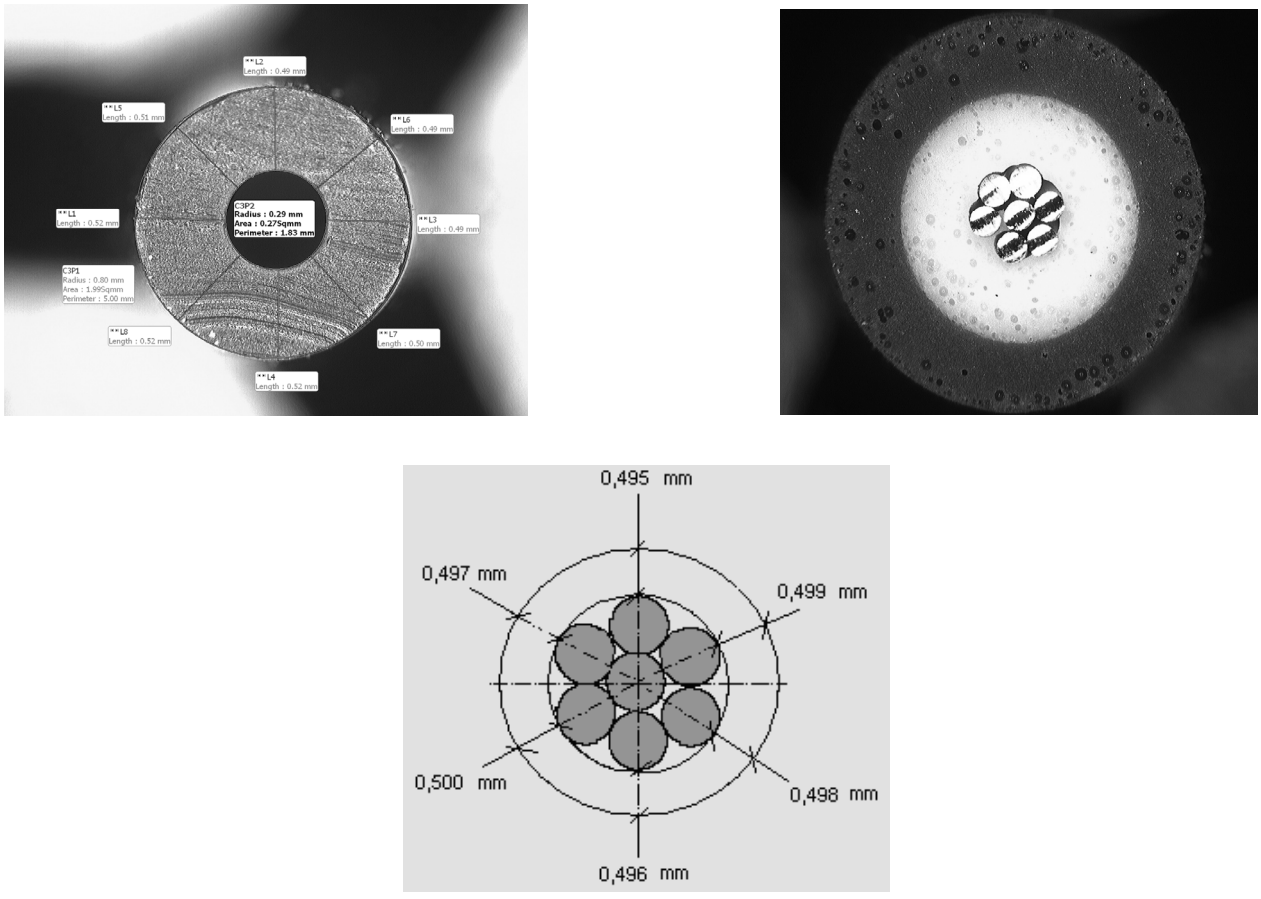

Figure 1. Geometry model

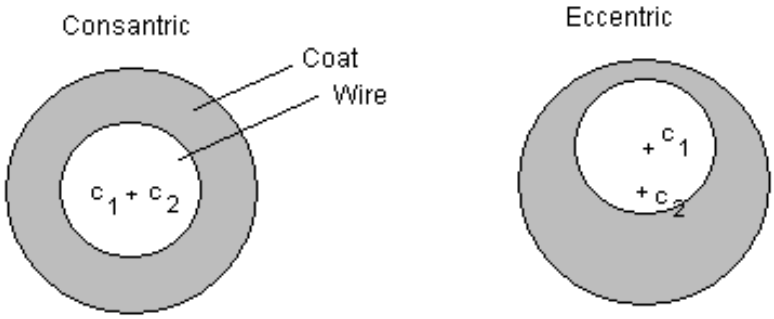

Figure 2. The relationship between centres of wire and coating

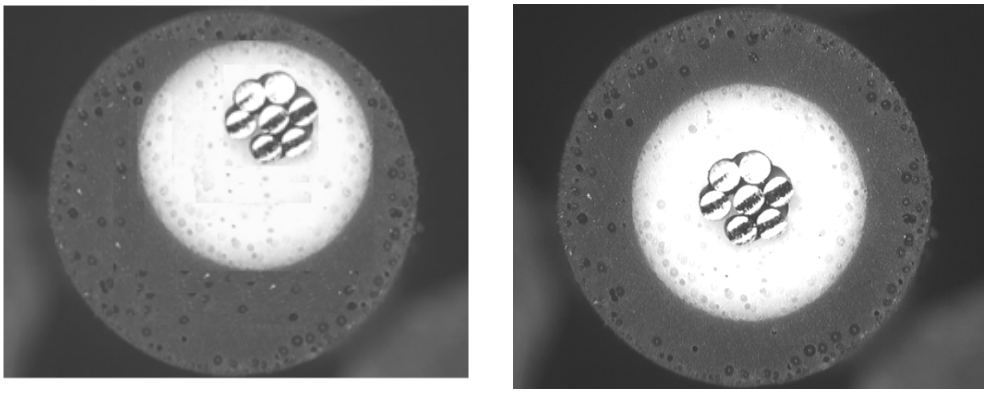

a- Eccentricity state b- Concentricity state

Figure 3. Wire coating states

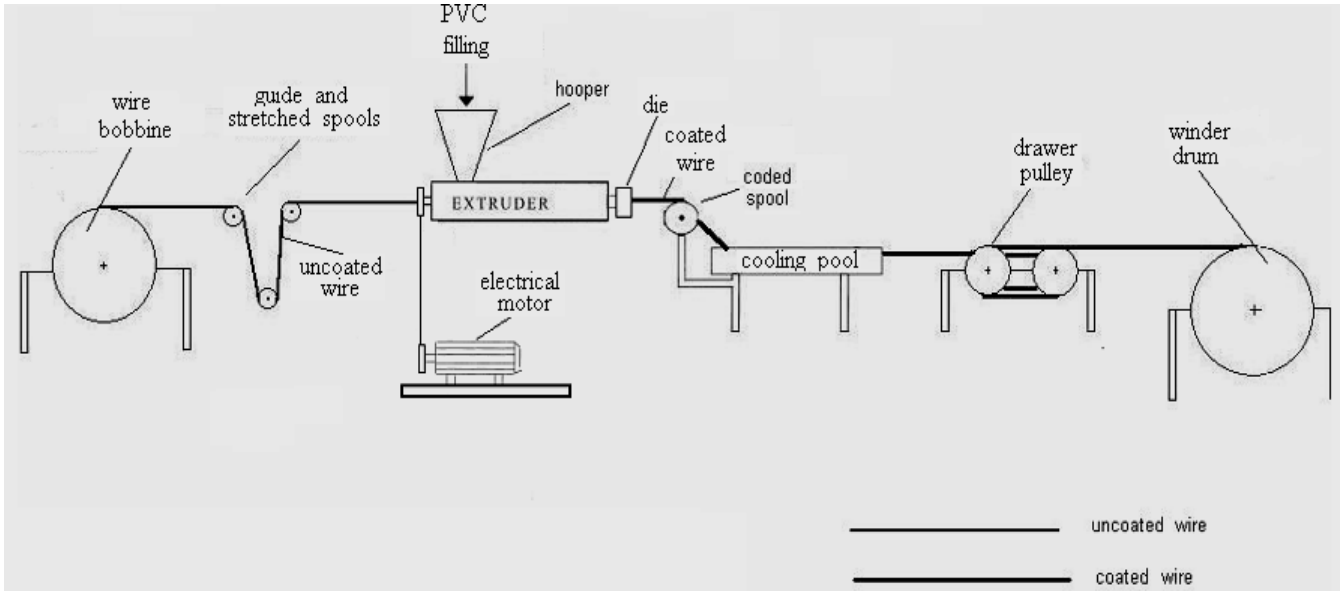

Figure 4. Wire coating extrusıon process scheme

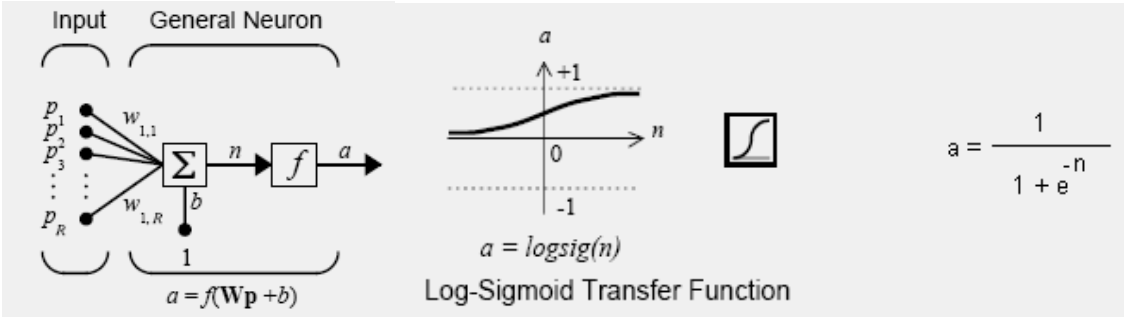

Figure 5. input schematic construction of artificial neural network

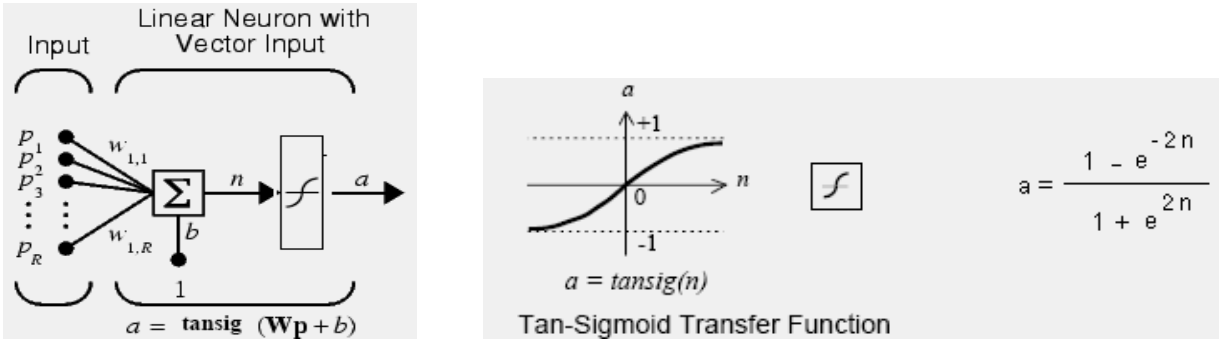

Figure 6. hidden schematic construction of artificial neural network

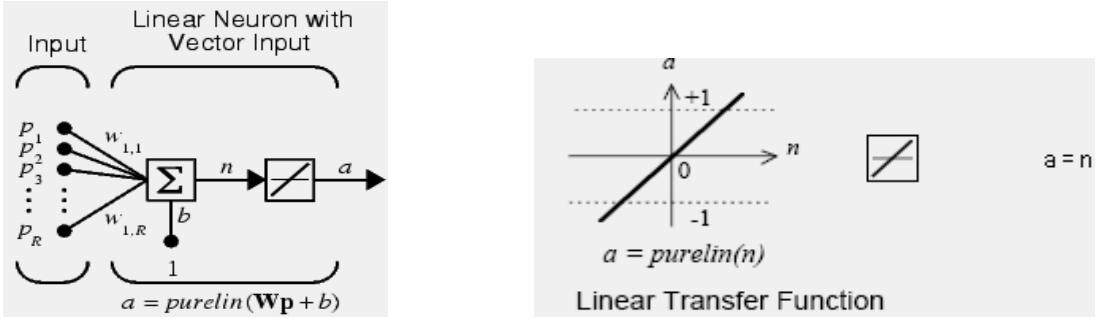

Figure 7. output schematic construction of artificial neural network

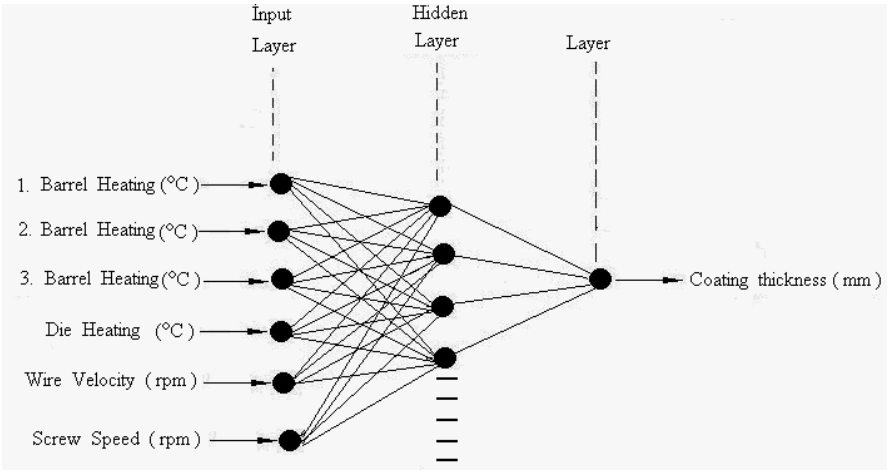

Figure 8. Wire coating configüration of theANN Model

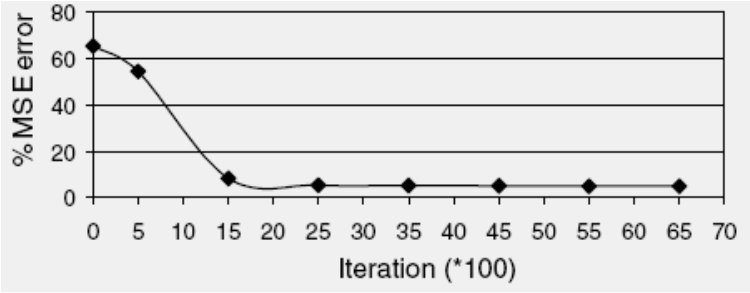

Figure 9. Iteration number versus mean square error for training nonlinear coating thickness

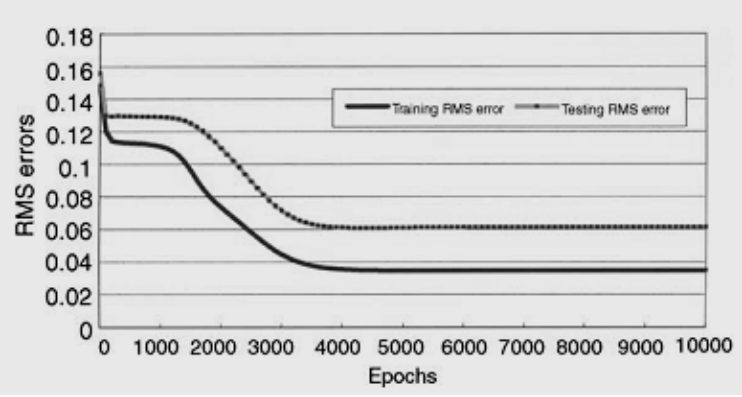

Figure 10. The development of training and testing RMS with learning epochs fort he 6-13-1 ANN model

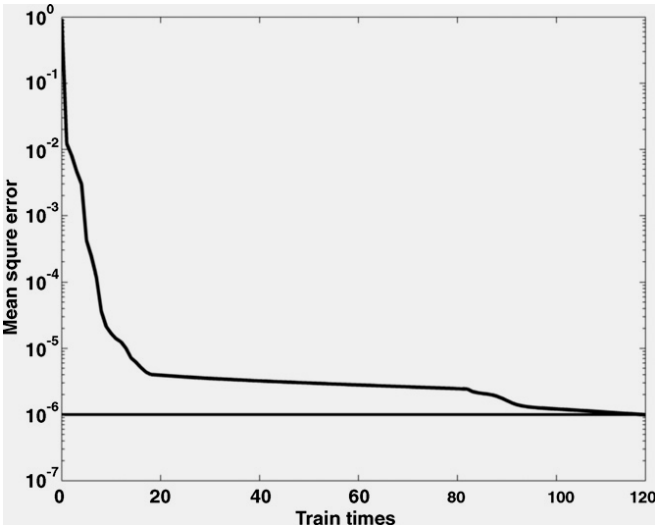

Figure 11. Train eror during the training

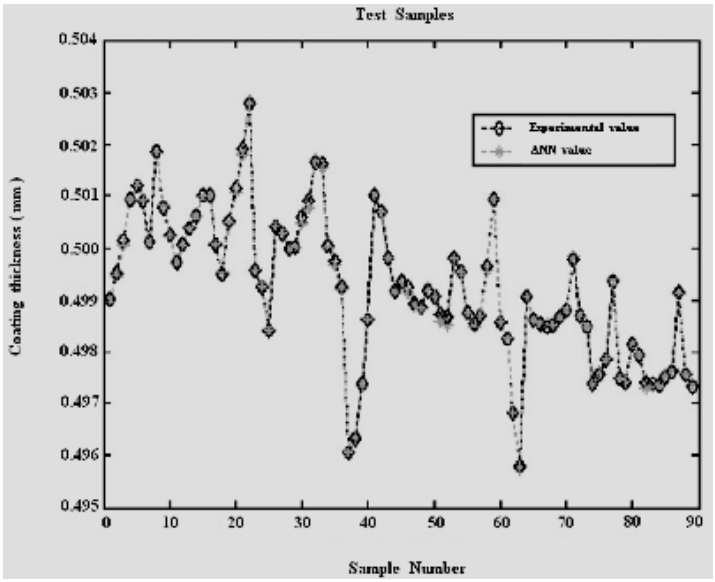

Figure 12. Test samples

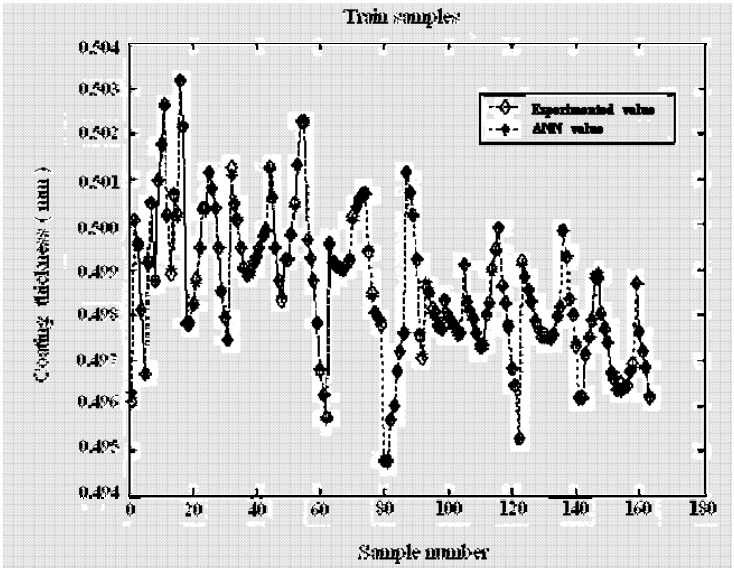

Figure 13. Train samples

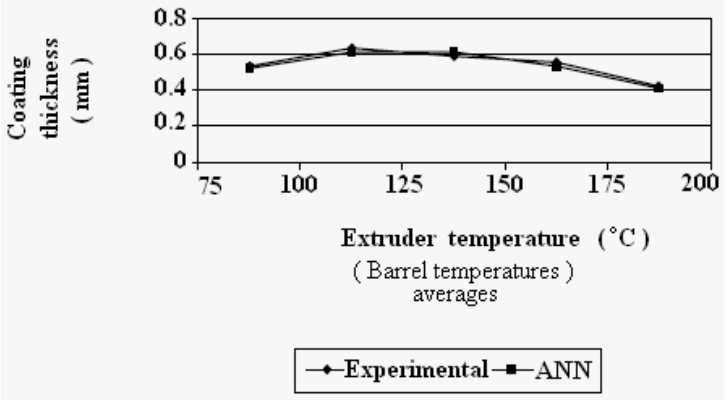

Figure 14. The comparison of coating thickness values with ANNs results

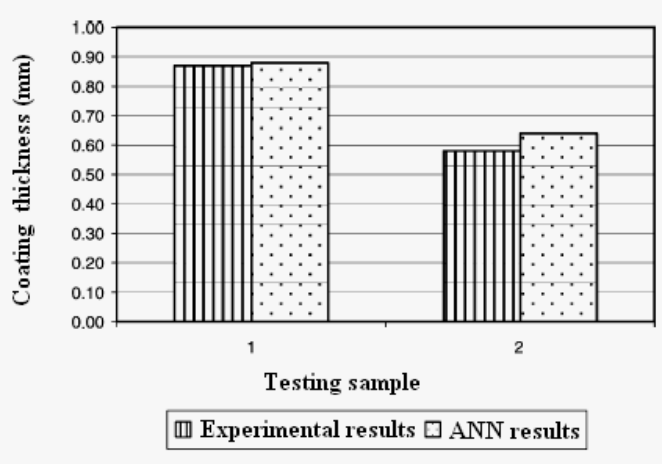

Figure 15. The comparison of experimental coating thickness Values with ANNs results for testing samples

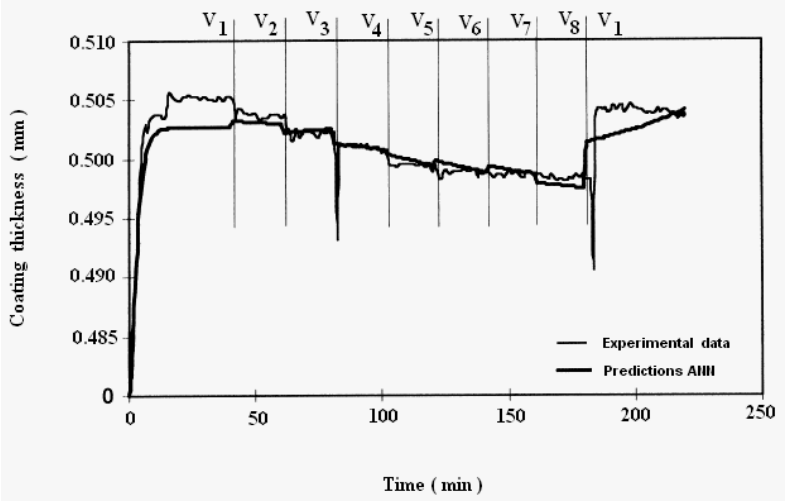

Figure 16. Experimental data and predictions of coating thickness by given full title ANN during extrusion

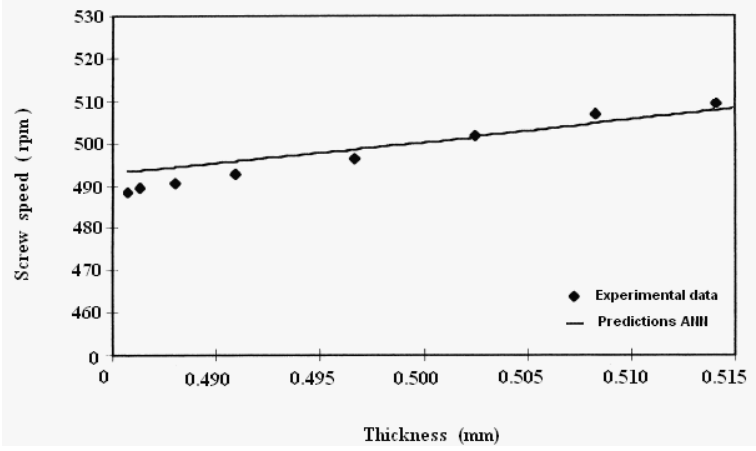

Figure 17. Experimental data and predictions of extruder screw speed with coating thickness by the 6 -13 – 1 ANN model

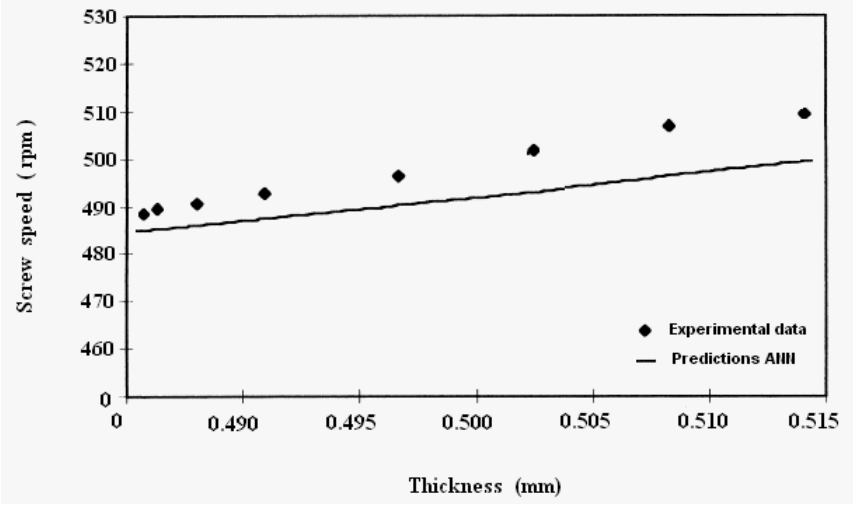

Figure 18. Experimental data and predictions of extruder screw speed with coating thickness by the 6 - 9 - 1 ANN model

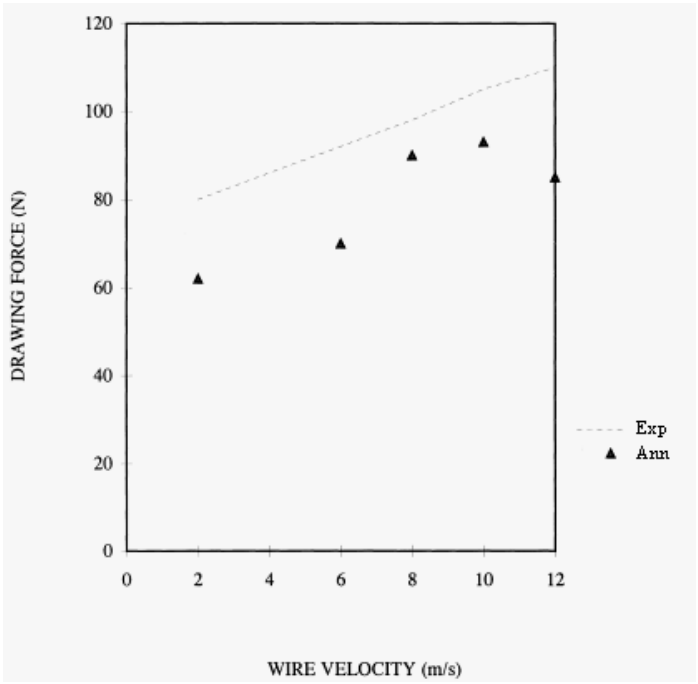

Figure 19. Drawing force for extruder temperature of 150 ◦C (Polimer – Ep 58 pvc)

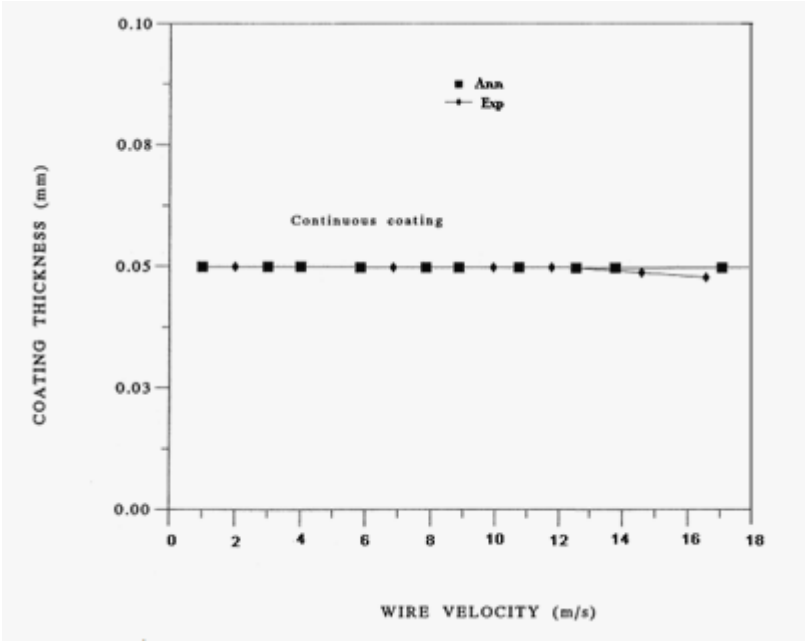

Figure 20. The relationship of wire velocity with coating thickness

Modern Applied Science

www.ccsenet.org/journal.html

Vol. 3, No. 7

July 2009

Geometric Condition of Singularity of $S_3^2(\Delta_{MS}^2)$

Lijuan Chen (Corresponding author) & Mingzhu Li

School of Science, Qingdao Technological University

Fushun Road 11, Qingdao, China

E-mail: chenljcool@163.com

Li Zhang

College of Information Science and Engineering, Shandong Agricultural University

Tai'an, China

Abstract

The aim of this paper is to investigate the geometric condition of singularity of $S_3^2(\Delta_{MS}^2)$. The algebraic of singularityof $S_3^2(\Delta_{MS}^2)$ is obtained in (Luo and Chen, 2005). The result of this paper will be useful to further study the geometric condition of singularity of $S_{\mu+1}^{\mu}(\Delta_{MS}^{\mu})(\mu > 3)$.

Keywords: Singularity, Spline space, Geometric condition

1. Introduction

The definition of multivariate spline is stated as follows(Wang, 1994): for a given partition Δ of a region Ω, the linearspace

$$S_k^{\mu}(\Delta) := \{s \mid s|_{T_i} \in P_k, s \in C^{\mu}(\Omega), \forall T_i \in \Delta\}$$

is called spline space of degree k with smoothness μ, where T_i is a cell of the Δ and P_k is the polynomial space of total degree $\leq k$.

Luo & Chen(Luo and Chen, 2005) investigated the singularity of the space $S_{\mu+1}^{\mu}(\Delta_{MS}^{\mu})(\mu \geq 2)$ and gave out an algebraic necessary and sufficient condition to the singularity. Take $\mu = 1$ for instance, i.e. Morgan-Scott triangulation. Shi(shi,1991) and Diener(Diener,1990) obtained the geometric significance of the necessary and sufficient condition of $\dim(S_2^1(\Delta_{MS})) = 7$, respectively. Du(Du, 2003) gave another type of the necessary and sufficient condition of the singularity of $S_2^1(\Delta_{MS})$ from the viewpoint of the projective geometry, that is, if the six quasi-inner edges are regarded as six points in the projective plane then they lie on a conic.

Now, we research the condition of $\mu = 2$.

2. Algebraic of Singularity of $S_3^2(\Delta_{MS}^2)$

The singularity of the spline space $S_3^2(\Delta_{MS}^2)$ is investigated by Luo and Chen(Luo and Chen, 2005) using the Generation Basis method. They obtained a necessary and sufficient condition in algebraic form. Δ_{MS}^2 is seen in Figure 1.

Denoted by

$$\begin{cases} l_1 = a_1 u + b_1 w \\ l_2 = a_2 u + b_2 w, \\ l_3 = a_3 u + b_3 w \end{cases} \quad \begin{cases} l_4 = a_4 w + b_4 v \\ l_5 = a_5 w + b_5 v \\ l_6 = a_6 w + b_6 v \end{cases} \text{ and } \begin{cases} l_7 = a_7 v + b_7 u \\ l_8 = a_8 v + b_8 u \\ l_9 = a_9 v + b_9 u \end{cases} \tag{1}$$

Then, the following conclusion in algebraic form is true

Theorem 1. (LuoandChen,2005) The spline space $S_3^2(\Delta_{MS}^2)$ is singular ($\dim(S_3^2(\Delta_{MS}^2)) = 11$) if and only if

$$\frac{a_1 a_2 a_3}{b_1 b_2 b_3} \cdot \frac{a_4 a_5 a_6}{b_4 b_5 b_6} \cdot \frac{a_7 a_8 a_9}{b_7 b_8 b_9} = -1 \tag{2}$$

Let a, b, c be three distinct non-infinity lines in P_2. Denoted by the intersection points between lines a, b, c and $l_i (i = 1,2,3), l_j (i = 4,5,6), l_i (i = 7,8,9)$ respectively. $u =< b, c >., v =< c, a >, w =< a, b >$

Let l_2', l_5' and l_8' be

$$l_2' = b_2 u + a_2 w, l_5' = b_5 w + a_5 v, l_8' = b_8 v + a_8 u .$$

Without loss of generality, we assume that the six points determined by intersections of Aa, Bb, Cc and intersections of l_2', l_5', l_8' are distinct from each other in the triangulation . Under this assumption, we shall prove the following important conclusion.

Theorem 2. The spline space $s_3^2\left(\Delta_{MS}^2\right)$ is singular if and only if the six points determined by intersections of Aa, Bb, Cc and intersections of l_2', l_5', l_8' lie on a conic.

Proof: Without loss of generality, we regard the lines u, v, w as basic lines, and let u = (1, 0, 0), w = (0, 1, 0), v = (0, 0, 1).

From (1), we have

$$l_1 = (a_1, b_1, 0) \quad l_4 = (0, a_4, b_4) \qquad l_7 = (b_7, 0, a_7)$$
$$l_3 = (a_3, b_3, 0), \quad l_6 = (0, a_6, b_6), \text{ and } \quad l_9 = (b_9, 0, a_9)$$
$$l_2' = (b_2, a_2, 0), \quad l_5' = (0, b_5, a_5), \qquad l_8' = (a_8, 0, b_8)$$

and

$$A = l_1 \times l_9 = (b_1 a_9, -a_1 a_9, -b_1 b_9), \; B = l_6 \times l_7 = (a_6 a_7, b_6 b_7 - a_6 b_7), \; C = l_3 \times l_4 = (b_3 b_4, -a_3 a_4, a_3 a_4)$$
$$a = w \times v = (1,0,0), \; b = u \times w = (0,0,1), \; c = u \times v = (0,-1,0).$$

So the lines Aa, Bb and Cc can be expressed as follows:

$$Aa = A \times a = (0, -b_1 b_9, a_1 a_9), \; Bb = B \times b = (b_6 b_7, -a_6 a_7, 0), \; Cc = C \times c = (a_3 a_4, 0, -b_3 b_4).$$

By direct calculations, the intersections of Aa, Bb, Cc and the intersections of l_2', l_5', l_8' are formed to be

$$v_1 = Aa \times Bb = (a_1 a_9 a_6 a_7, a_1 a_9 b_6 b_7, b_1 b_9 b_6 b_7), \quad v_2 = Bb \times Cc = (a_6 a_7 b_3 b_4, b_6 b_7 b_3 b_4, a_6 a_7 a_3 a_4),$$
$$v_3 = Cc \times Aa = (-b_3 b_4 b_1 b_9, -a_3 a_4 a_1 a_9, -a_3 a_4 b_1 b_9), \quad v_4 = l_2' \times l_5' = (a_2 a_5, -b_2 a_5, b_2 a_5),$$
$$v_5 = l_5' \times l_8' = (b_5 b_8, a_5 a_8, -b_5 a_8), \; v_6 = l_8' \times l_2' = (-b_8 a_2, b_8 b_2, a_8 a_2)$$

We now give the equivalent condition that $v_1, v_2, \cdots, v_6$ lie on a conic by Pascal's Theorem. To do this, the three intersection points of three subtense of the hexagon with vertices $v_1, v_2, \cdots, v_6$ are

$$B_1 = (v_1 \times v_5) \times (v_2 \times v_6) = (b_1 b_5 b_6 b_7 b_8 b_9 + a_1 b_5 a_6 a_7 a_8 a_9)(b_2 b_3 b_4 a_6 a_7 b_8 + a_2 b_3 b_4 b_6 b_7 b_8)$$
$$-(a_1 a_5 a_6 a_7 a_8 a_9 - a_1 b_5 b_6 b_7 b_8 a_9)(-a_2 a_3 a_4 a_6 a_7 b_8 - a_2 b_3 b_4 a_6 a_7 a_8)(a_1 a_5 a_6 a_7 a_8 a_9 -$$

$a_1b_5b_6b_7b_8a_9)(a_2b_3b_4b_6b_7a_8 - b_2a_3a_4a_6a_7b_8) - (-a_1b_5b_6b_7a_8a_9 - b_1a_5b_6b_7a_8b_9)$

$(a_6a_7b_3b_4b_8b_2 + b_6b_7b_3b_4b_8a_2)(-a_1a_9b_6b_7b_5a_8 - b_1b_9b_6b_7a_5a_8)(-a_6a_7a_3a_4a_2b_8$
$-a_6a_7b_3b_4a_2a_8) - (b_1b_9b_6b_7b_5b_8 + a_1a_9a_6a_7b_5a_8)(b_6b_7b_3b_4a_8a_2 - a_6a_7a_3a_4b_2b_8)$,

$B_2 = (v_1 \times v_4) \times (v_3 \times v_6) = (b_1a_2a_5b_6b_7b_9 - a_1b_2b_5a_6a_7a_9)(-b_1b_2b_3b_4b_8b_9 - a_1a_2a_3a_4b_8a_9)$
$-(-a_1b_2a_5a_6a_7a_9 - a_1a_2a_5b_6b_7a_9)(b_1a_2a_3a_4b_8b_9 + b_1a_2b_3b_4a_8b_9)(-a_1b_2a_5a_6a_7a_9 -$

$a_1a_2a_5b_6b_7a_9)(-a_1a_2a_3a_4a_8a_9 + b_1b_2a_3a_4b_8b_9) - (a_1b_2b_5b_6b_7a_9 + b_1b_2a_5b_6b_7a_8b_9)$

$(-b_3b_4b_1b_9b_8b_2 - a_3a_4a_1a_9b_8a_2)(a_1a_9b_6b_7b_2b_5 + b_1b_9b_6b_7b_2a_5)(a_3a_4b_1b_9b_8a_2$
$+b_3b_4b_1b_9a_8a_2) - (b_1b_9b_6b_7a_2a_5 - a_1a_9a_6a_7b_2b_5)(-a_3a_4a_1a_9a_8a_2 + a_3a_4b_1b_9b_8b_2)$,

$B_3 = (v_2 \times v_4) \times (v_3 \times v_5) = (a_6a_7a_3a_4a_2a_5 - a_6a_7b_3b_4b_2b_5)(-b_3b_4b_1b_9a_5a_8 + a_3a_4a_1a_9b_5b_8)$
$-(-a_6a_7b_3b_4b_2a_5 - b_6b_7b_3b_4a_2a_5)(-a_3a_4b_1b_9b_5b_8 - b_3b_4b_1b_9b_5b_8)(-a_6a_7b_3b_4b_2a_5$

$-b_6b_7b_3b_4a_2a_5)(a_3a_4a_1a_9b_5a_8 + a_3a_4b_1b_9a_5a_7) - (b_6b_7b_3b_4b_2b_5 + a_6a_7a_3a_4b_2a_5)$

$(-b_3b_4b_1b_9a_5a_8 + a_3a_4a_1a_9b_5b_8)(b_6b_7b_3b_4b_2b_5 + a_6a_7a_3a_4b_2a_5)(-a_3a_4b_1b_9b_5b_8$
$-b_3b_4b_1b_9b_5a_8) - (a_6a_7a_3a_4a_2a_5 - a_6a_7b_4b_3b_2b_5)(a_3a_4a_1a_9b_5b_8 + a_3a_4b_1b_9a_5a_8)$

The directed area of triangle determined by B_1, B_2 and B_3 is

$(B_1, B_2, B_3) = -(b_5b_8b_2 + a_2a_5a_8)^2(b_7b_6b_2 + b_2a_6a_7)(b_5b_1b_9 + a_1a_5a_9)(b_3a_8b_4 + a_3a_4b_8)$

$(b_1b_3b_4b_6b_7b_9 - a_1a_3a_4a_6a_7a_9)^2(b_1b_2b_3b_4b_5b_6b_7b_8b_9 + a_1a_2a_3a_4a_5a_6a_7a_8a_9)$

Since the six points $v_1, v_2, \cdots, v_6$ are all distinct, we have

$-(b_5b_8b_2 + a_2a_5a_8)^2(b_7b_6b_2 + b_2a_6a_7)(b_5b_1b_9 + a_1a_5a_9)(b_3ba_8b_4 + a_3a_4b_8)$

$(b_1b_3b_4b_6b_7b_9 - a_1a_3a_4a_6a_7a_9)^2 \neq 0$.

Hence, it follows from Pascal's Theorem (says that $v_1, v_2, \cdots, v_6$ lie on a conic if an only if $(B_1, B_2, B_3) = 0$ that the necessary and sufficient condition that $v_1, v_2, \cdots, v_6$ lie on a conic is

$$\frac{a_1a_2a_3}{b_1b_2b_3} \cdot \frac{a_4a_5a_6}{b_4b_5b_6} \cdot \frac{a_7a_8a_9}{b_7b_8b_9} = -1$$

4. Example

In this section, we shall give two examples to illustrate our main results distinctly. One of the conic is elliptic conic, the other is hyperbolic conic.

Example 1. Consider a given triangulation shown in Fig. 2, where

$A = (1/2,2,1), B = (-4,-2,1), C = (4,-2,1), a = (0,-1,1), b = (1,0,1),$

$c = (-1,0,1), u : -y = 0, v : -x - y - z = 0, w : x - y - z = 0,$

$l_1 : -4x - y + 4/3z = 0, l_2 : -2/3x - y + 2/3z = 0, l_3 : -1/4x - y - z = 0,$

$l_4 : 1/4x - y - z = 0, l_5 : 2/3x - y + 2/3z = 0, l_6 : 4/3x - y + 4/3z = 0$

$l_7 : 2x - y - 2z = 0, l_8 : -1/2x - y - z = 0, l_9 : -42/47x - y - 42/47z = 0$.

It can be proved that the spline space $S_3^2(\Delta_{MS}^2)$ of piecewise polynomial of degree 3 with smoothness 2 is singular. The corresponding l_7', l_8', l_9' are

$l_7' = -x - y + z = 0, l_8' = 1/2x - y - z = 0, l_9' = -5/47x - y - 5/47z = 0$.

In this example, the conic corresponding to Theorem 2 is

$302x^2 - 2861xy + 15800y^2 - 1421x + 12880y + 2624 = 0$,

which forms elliptic conic and is shown in Fig. 2

Example 2. The following example shows that a conic corresponding to Theorem 2 forms hyperbolic conic. Given a singular triangulation Δ_{MS}^2 for spline space of piecewise polynomial of degree 3 with smoothness shown in Fig. 3, where

$A = (1/2,2,1), B = (-4,-3,1), C = (3,-4,1), a = (0,-2,1), b = (1,-1,1),$

$c = (-1,0,1), u: -1/2x - y - 1/2z = 0, v: -2x - y - 2z = 0, w: x - y - 2z = 0,$

$l_1: -6x - y + 5z = 0, l_2: -3/2x - y + 1/2z = 0, l_3: -2/3x - y - 2z = 0,$

$l_4: 1/4x - y - 2z = 0, l_5: x - y + z = 0, l_6: 4/3x - y + 4/3z = 0,$

$l_7: 1/7x - y - 8/7z = 0, l_8: 2x - y - 2z = 0, l_9: -38/61x - y - 38/61z = 0$

The corresponding l_7', l_8', l_9' are

$l_7' = 5/14x - 19/14 - y = 0, l_8' = -3x - 2 - y = 0, l_9' = -229/122x - 229/122 - y = 0$,

and the corresponding duality figure of the triangulation is shown in Fig. 3. A hyperbolic curve passing through the six points as mentioned Theorem 2 is shown in 3 and

$$\frac{1143}{2803}x^2 + \frac{1028}{1963}y^2 - \frac{1022}{715}xy - \frac{503}{256}xz + \frac{1161}{1112}yz + z = 0$$

References

P. Alfeld. (1985). On the dimension of multivariate piecewise polynomial functions, Proc. Biennial Dundee Conf. On Numerical Analysis, Pitman, London.

Diener, D. (1990). Instability in the dimension of spaces of bivariate piecewise polynomials of degree $2r$ and smoothness order r, SIAM J. Numer. Anal., Vol. 2, No. 3, 543-551.

Hong Du. (2003). A geometric appraoch to $\dim(S_2^1(\Delta_{MS}))$, (R.H. Wang Ed.), AMS/IP Studies in Advanced Mathematics ,67-70.

Luo Zhongxuan, Wang Renhong. (2006). Structure and Dimension of Multivariate Spline Space on Arbitrary Triangulation, Journal of Computational and Applied Mathematics, Vol. 195, Issues 1-2, 113-133.

Shi X. Q. (1991) The Singularity of Morgan-Scott Triangulation, CAGD, 8, 201-206.

Wang R. H., X. Q. Shi, Z. X. Luo, Z. X. Su. (2002). Multivariate Spline and its Applications, Kluwer Press, 2002, Academic Press, Beijing, 1994(in Chinese).

Z. X. Luo and L. J. Chen. (2005). The singularity of $S_{\mu+1}^{\mu}(\Delta_{MS}^{\mu})$, J. Information and Computational Science, Vol. 2 No. 4,739-746.

Zhongxuan Luo. (2001). Generator bases of modules in and their Application, Acta Mathematica Sinica, 44(6), 983-994.

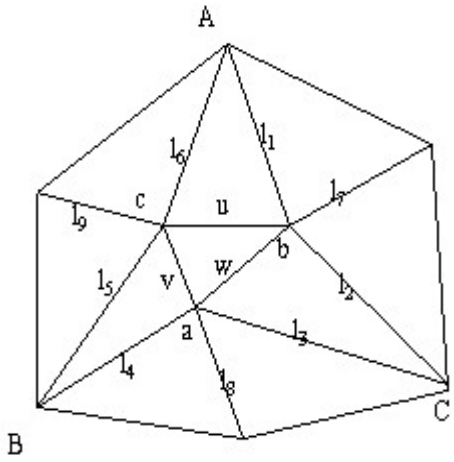

Figure 1. Δ^2_{MS}

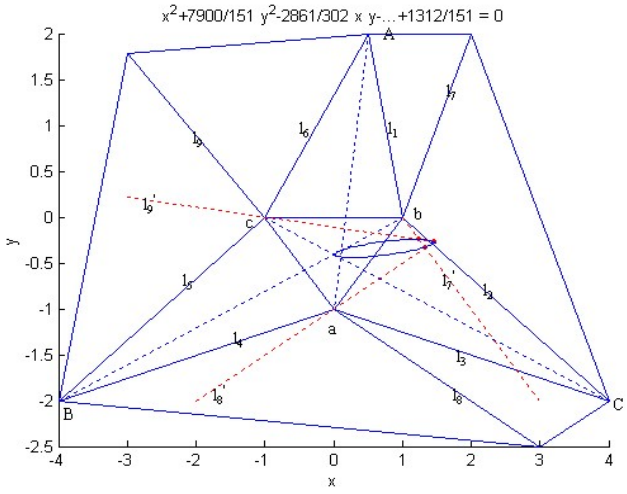

Figure 2. Example 1

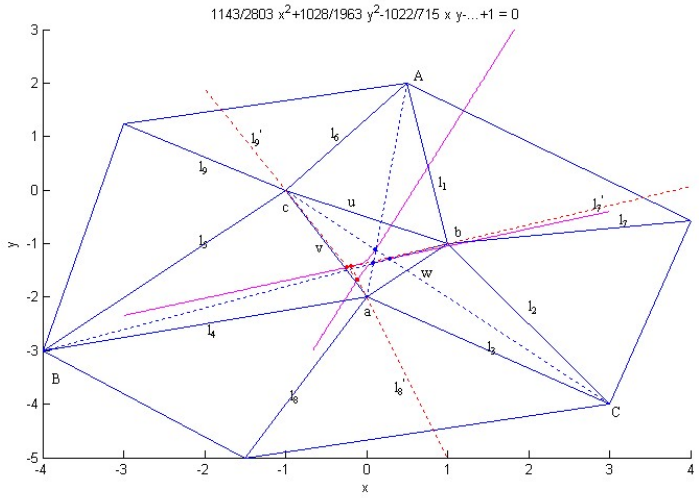

Figure 3. Example 2

Modern Applied Science

www.ccsenet.org/journal.html

Vol. 3, No. 7

July 2009

Gallium Arsenide Nanowires Formed by Au-assisted Metal-organic Chemical Vapor Deposition: Effect of Growth Temperature

Rosnita Muhammad, Zulkafli Othaman, Yussof Wahab, Samsudi Sakrani, W. Faizal W. Ahmad & Mohd Nazri

Physics Department, Faculty of Science

University Teknologi Malaysia

81310 UTM Skudai, Johor, Malaysia

E-mail: rosnita@ utm.my

Abstract

We have investigated the growth of gallium arsenide (GaAs) nanowires as a function of temperatures in metal organic chemical vapor deposition (MOCVD) to establish the mechanisms that govern wire growth and to optimize growth conditions. The growth follows the vapor-liquid-solid method by applying nanoparticle gold colloid as a catalyst to forms a eutectic liquid alloy with the substrate. The semi insulating undoped (111)B GaAs was first dipped in the poly-L-lysine solution before 30nm gold colloid dropped on the substrate surface. Growth process in the MOCVD system were done at temperatures between 380 and 600ºC with growth time set is 30 min. All the grown samples were analyzed using a field emmission scanning electron microscope (FE-SEM) and scanning electron microscopy (SEM). With increasing temperature the nanowire height increases but leads to significant tapering of the nanowire due to competing growth at the (111) substrate surface. At low temperatures nanowires grown are cylindrical-shaped with diameter wires between 50 and 100 nm.

Keywords: GaAs, Nanowire, Vapor-liquid solid mechanism, MOCVD, Tapering

1. Introduction

Nanowires can be grown as highly perfect one-dimensional nano-structures, suitable for basic physics investigation (nano-probes, transport physics, etc) as well as for potential applications in optical and electrical devices (LEDs, waveguides, field emitters, nano-probes, etc)(Lars Samuelson, 2003)(Yue Wu, Yi Chui, Lynn Huynh, Carl J. Barrelet, David C. Bell and Charles M. Lieber, 2004)(L. J. Lauhon, Mark S. Gudiksen and Charles M. Lieber, 2004). In most cases, the growth is initiated by the presence of metal particles, which act as catalyst. In the classical description, the growth follows the vapor-liquid solid (VLS) mechanism(R. S. Wagner and W. C. Ellis, 1964), although details are still in debate. Metal-organic chemical vapor deposition (MOCVD) for growing GaAs and InAs nanowires was already used by Hiruma et *al* (K. Hiruma, M. Yazawa, T. Katsuyama, K. Ogawa, K. Haraguchi, M. Koguchi and H. Kakibayashi, 1995), with deposited Au films, transforming into catalytically active nanoparticles by annealing. Very recently, the fabrication of nanowire-based one-dimensional heterostructures has been reported (Charles M. Lieber, 2003)(L. J. Lauhon, Mark S. Gudiksen and Charles M. Lieber, 2004) and their functionality in resonant tunneling structures has been demonstrated (M. T. Bjork et. al., 2002). However, there are still many open question to be answered before nanowires can be used as versatile building blocks in nanostructure devices. We focus in this paper on investigating the growth mechanism, with special emphasis on effect of growth temperature and optimizing the growth conditions of GaAs nanowires.

2. Experiment

The experiments start with semi insulating undoped GaAs (111)B substrates immersed in 0.1% poly-L-lysine (PLL) solution for 3 min. After washing with deionize water and subsequent drying with N_2, the wafer was cut into desired size. The 30 nm diameter gold colloids were dispersed on the wafer surface by using microlittre pipette and immediately washed after 20 sec. The PLL layer on the surface is positively charged and attracts the negatively charged of the gold colloids. The cutting wafer was put on the graphite susceptor inside the vertical reactor in the MOCVD system for the growth processes. The growth pressure inside vertical reactor chamber was 76 Torr. Trimethylgallium

(TMGa) and arsine (AsH_3; 10% in H_2) were used as the source gases. The AsH_3 to TMGa molar flow ratio (the V/III ratio) was set at 166. The wafer was annealed in situ at 600°C under AsH_3 ambient for 10 min to desorbed surface contaminants and form eutectic alloy between Ga and gold colloid (Au). After annealing process, the temperature was ramped down to the desired nanowire growth temperature. The growth temperature was chosen between 380°C to 600°C. Nanowire growth started when trimethylgallium (TMGa) was supplied to the reactor chamber. The nanowire growth time was kept constant at 30 min. All the grown samples were then characterized using a JSM-6390LV scanning electron microscope (SEM) and JEOL JSM-6701F field emission scanning electron microscope (FE-SEM).

3. Results and discussions

Figure 1 shows scanning electron microscopy (SEM) images of GaAs nanowires grown at various temperatures (380°C – 600°C), taken with the substrates tilted 30° from the electron beam. The tilting is needed to verifying structures from 2 D to 3 D images. The first temperature (Figure 1(a)) is closed to the lowest eutectic temperatures (339.4°C and 348.9°C) of the AuGa phase diagram (Zhong Lin Wang, Yi Liu and Ze Zhang, 2002) which particles phase transition is solid below 340°C and return to liquid phase at 400°C. At this stage, only particles in size range between 50 – 100nm distributed on the substrate surface. The particles increased further in width and height with increasing growth temperature to 440°C. The nanowire height increases with increasing temperature up to 540°C and then decreases at higher temperature, while tapering of the nanowires increases continuously. From the classical VLS mechanism theory, an ideal liquid surface captures all impinging material source atoms, while a solid surface rejects almost all source atoms if the temperature is sufficiently high(R. S. Wagner and W. C. Ellis, 1964).

Tapering of the nanowires at high growth temperature is due to the effect of radial growth. If the growth of nanowires is dominated by the reaction species impinging directly on the Au nanoparticles on the top of the nanowires, ideal one dimensional nanowire growth is achieved without any tapering. However, a significant amount of reaction species could also have arrived at the nanowire sidewall or (111)B substrate and diffused toward the Au nanoparticle. During the migration process, the incorporation of the reaction species into the (111)B surface and nanowire sidewall takes place at high growth temperature. This incorporation, known as the 2-D growth, results in the tapering (H. H. Tan, K. Sears, S. Mokkapati, Lan Fu, Yong Kim, P. McGowan, M Buda and C. Jagadish, 2006). The decrease of apparent nanowire height at 600°C is due to the increase of 2-D growth at (111)B substrate. From Figure 1 the optimized growth temperature is in the range of 420 – 480°C with little tapering and reasonable uniformity.

All the nanowires are growing in <111>B direction i.e., they are standing vertically on the (111)As surface. In addition, also on (110) cleavage planes, which were exposed to Au nanoparticles dropped, nanowires were growing. At lower growth temperature, the nanowires grown are cylindrical shape whereas at high temperature, visualizing the hexagonal cross-section with the {110} side facets is clearly defined. Plante and LaPierre (2008) already investigated the faceting GaAs nanowire sidewall using molecular beam epitaxial growth. They conclude that tapered tip exhibit different facets than the base of the wire during planar growth of the nanowire sidewall (M. C. Plante and R. R. LaPierre, 2008).

The temperature-dependent reduction in tapering also can be explained using schematically with reference to the axial and radial growth mechanism shown in Figure 2(Hannah J.Joyce, Qiang Gao, H. Hoe Tan, Chennupati Jagadish, Yong Kim, Xin Zhang, Yanan Guo and Jin Zou, 2007). Reaction species which impinge directly upon the nanoparticle contribute to axial growth. Additionally, Ga adatoms are adsorbed on the substrate and nanowire sidewalls and diffuse along the concentration gradient toward the growing nanoparticle-nanowire interface. These diffusion adatoms contribute to both radial and axial growth, hence radial growth competes with axial growth at high growth temperature as can be seen on Figure 3. Images of GaAs nanowires are taken from cross-sectional FE-SEM measurement. The nanowires get increasingly tapered with the thicker end at the base and segmented. These trends are in agreement with observations of Hiruma et. al. (K. Hiruma, M. Yazawa, T. Katsuyama, K. Ogawa, K. Haraguchi, M. Koguchi and H. Kakibayashi, 1995). Because radial growth is kinetically limited, diffusing adatoms are less likely to be incorporated into nanowire sidewalls at lower growth temperatures. Furthermore, adatom diffusion length decreases with decreasing growth temperature. This reduces the flux of adatoms diffusing from the substrate, limiting radial growth and tapering.

The measured height and width of the GaAs nanowires at different growth temperature were plotted in Figure 4. The height of the nanowires was measured above the base feature, which is an actual measure of the growth enhancement of the catalytic particle. The width and diameter was measured at the middle point of the full length for each wire as did the average length. The nanowire height increases with increasing temperature up to 540°C and then decreases at higher temperature. The width of the nanowires increases continuously. Each measurement point represents an average over about 50 nanowires, selected from areas of high nanowires homogeneity. A maximum in nanowire height occurred at 540°C growth temperature. Towards low temperatures, the height decreases almost linearly in range 420 - 540 °C. By plotting the graph of growth rate (nm/s) versus 1/T (K) for GaAs nanawire, the slope of the low-temperature times (-R) results in Arrhenius activation energy which is 58.86 kJ/mol. The equation used was

$$E_a = -R\left(\frac{\partial \ln k}{\partial\left(\frac{1}{T}\right)}\right)$$

where E_a is the activation energy and R is the gas constant equal to 8.314472 $JK^{-1}mol^{-1}$ (James F. Shackelford, 1996). The activation energy, 58.86 kJ/mol found agreed with activation energy for the overall GaAs low-temperature MOCVD process (D. H. Reep, S. K. Ghandi, 1983). Borgstrom et al (2004) found in their observation of activation energy at higher growth temperature after limitation of nanowires growth rate, that Au on top of the nanowires does not effect the activation energy, but the process outside the droplet (M. Borgstrom, K. Depert, L. Samuelson, W. Seifert, 2004).

4. Conclusion

We have investigated the height, width and shape of Au-catalyzed GaAs nanowires grown on the (111)B GaAs surface, as a function of temperature using MOCVD system. With increasing temperature, the height of the nanowire increases but lead to tapered of the nanowire sidewall. Towards low temperatures, the nanowire height decreases almost linearly in the arrhenius plotted. The slope results in activation energy about 58.86 kJ/mol, the value is in agreement with activation energies reported for overall GaAs nanowires at low temperatures using MOCVD. The decreasing of nanowire height towards higher temperature most probably the onset of competing growth on (110) side-facets and on the Au-free (111)B substrate surface. We conclude that the optimizing growth temperature is in the range of 420 – 480^{o}C with minimal tapering and reasonable uniformity of growing GaAs nanowires.

Acknowledgements

The authors acknowledge the Ministry of Science, Technology and Environment Malaysia for the financial support through Science funding 03-01-06-SF0370 and the Ibnu Sina Institute for the laboratory facilities.

References

Charles M. Lieber. (2003). Nanoscale science and technology: Building a big future from small thing, *MRS Bulletin*, p 486-491.

D. H. Reep, S. K. Ghandi. (1983). *Journal of electrochemical society*, Vol 130, p 675.

H. H. Tan, K. Sears, S. Mokkapati, Lan Fu, Yong Kim, P. McGowan, M Buda and C. Jagadish. (2006). QD and Nanowires grown by MOCVD for optoelectronic device applications, *IEEE Journal of selected topics in quantum electronics*, Vol 12, No 6, p 1242.

Hannah J.Joyce, Qiang Gao, H. Hoe Tan, Chennupati Jagadish, Yong Kim, Xin Zhang, Yanan Guo and Jin Zou. (2007). Twin-Free Uniform Epitaxial GaAs Nanowires Grown by a two-temperature process, *Nanoletters*, Vol 7, No 4, p 921-926.

James F. Shackelford. (1996). *Introduction to Materials Science for Engineers*, Fourth edition, Prentice Hall International Editions, p 109.

K. Hiruma, M. Yazawa, T. Katsuyama, K. Ogawa, K. Haraguchi, M. Koguchi and H. Kakibayashi. (1995). Growth and optical properties of nanometer-scale GaAs and InAs whiskers, *Journal of Applied Physics*, Vol 77 (2), p 447.

L. J. Lauhon, Mark S. Gudiksen and Charles M. Lieber. (2004). Semiconductor nanowire heterostructure, *Phil. Trans. R. Soc. Lond*, A, 362, p 1247-1260.

L. J. Lauhon, Mark S. Gudiksen and Charles M. Lieber. (2004). Semiconductor nanowire heterostructure, *Phil. Trans. R. Soc. Lond*, A, 362, p 1247-1260.

Lars Samuelson. (2003). Self-forming nanoscale devices, *Materials today*, p22.

M. Borgstrom, K. Depert, L. Samuelson, W. Seifert. (2004). Size- and shape controlled GaAs nanowhiskers grown by MOVPE : a growth study, *Journal of crystal growth*, Vol 260, p 18 – 22.

M. C. Plante and R. R. LaPierre. (2008). Au-assisted growth of GaAs nanowires by gas source molecular beam epitaxy : Tapering, sidewall faceting and crystal structure, *Journal of Crystal Growth*, Vol 310, p 356-363.

M. T. Bjork et. al. (2002). Nanowire resonant tunneling diodes, *Applied Physics Letter*, Vol 81, Issue 23, p 4458.

R. S. Wagner and W. C. Ellis. (1964). Vapor-liquid solid mechanism of single crystal growth, *Applied Physics Letter*, Vol 4, No 5, p 89.

Yue Wu, Yi Chui, Lynn Huynh, Carl J. Barrelet, David C. Bell and Charles M. Lieber. (2004). Controlled growth and structures of molecular-scale silicon nanowires, *Nanoletters*, Vol 4, No 3, p 433-436.

Zhong Lin Wang, Yi Liu and Ze Zhang. (2002). *Handbook of nanophase and nanostructured materials-materials system and applications (I) Vol 3*, Kluwer Academic Publisher.

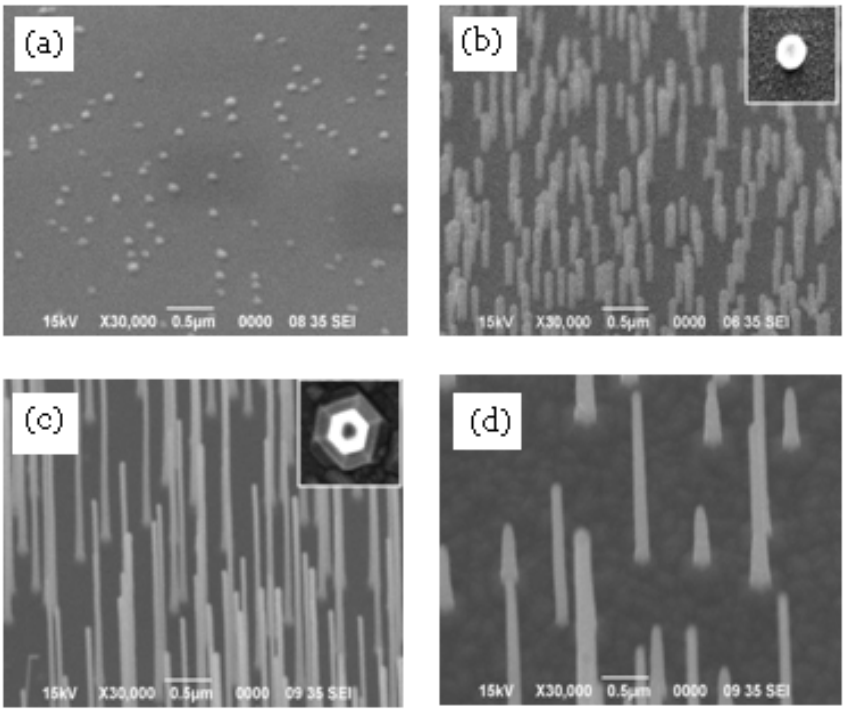

Figure 1. SEM images of GaAs nanowires grown at different temperatures: (a) 380^{o}C, (b) 440^{o}C, (c) 540^{o}C and (d) 600^{o}C. The substrate is (111)B GaAs, tilted by 30^{o} towards the electron beam. The inset figure shows topview of a nanowire

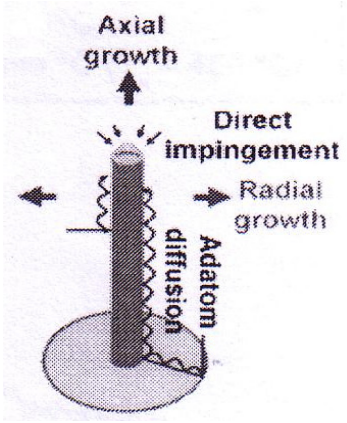

Figure 2. Schematic illustrating axial and radial nanowire growth, fed by direct impingement of precursor species on the nanoparticle and Ga adatom diffusion from the substrate and along nanowire sidewalls (Hannah J.Joyce, Qiang Gao, H. Hoe Tan, Chennupati Jagadish, Yong Kim, Xin Zhang, Yanan Guo and Jin Zou, 2007)

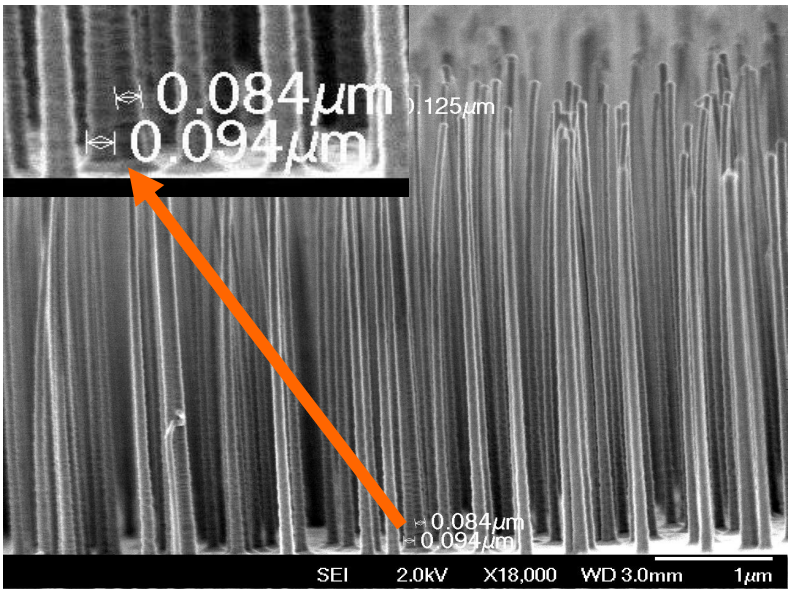

Figure 3. FE-SEM images of cross sectional GaAs nanowires grown at high temperature 540°C with rod-like structure at the tip and hexagonal facet at the base

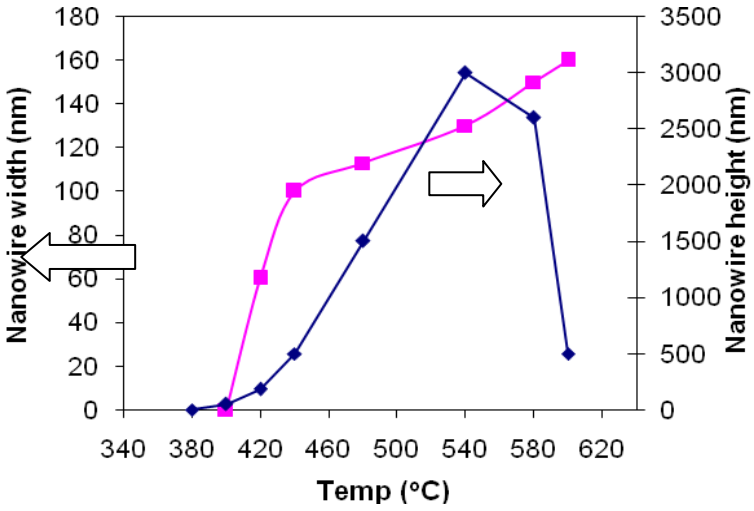

Figure 4. Width and height of GaAs nanowire as a function of the growth temperature The nanowire growth time and V/III ratio was set at 30 min and 166 respectively.